Transport-Model Analysis of the ϕ-Meson Spectrum Produced in 12 GeV pA Reactions

Masaya Ichikawa

October 15, 2025

Abstract

The masses of hadrons, particularly those of light hadrons, are significantly larger than the masses of the quarks that constitute them. Theoretically, it is considered that quarks acquire large constituent quark masses through their interactions with the non-trivial vacuum of the strong interaction, specifically, the quark condensate. The quark condensate is an order parameter of the spontaneously broken chiral symmetry of Quantum Chromodynamics (QCD). On the other hand, the spontaneous breaking of chiral symmetry is predicted to be partially restored at finite density or high temperature. Therefore, measuring the hadron mass spectrum under such conditions is crucial for understanding the mechanism of mass generation of hadrons. Various experimental measurements and theoretical calculations have been carried out to investigate the properties of hadrons at high temperatures or finite densities.

In the KEK-PS E325 experiment, a 12 GeV proton beam was irradiated onto carbon and copper targets with the aim of collecting vector meson e^+e^- decay events inside nuclei. In past analyses focusing particularly on the ϕ meson, the reconstructed invariant-mass spectra were divided according to the target nucleus and meson velocity. Since most of the ϕ mesons produced in this setup are expected to decay outside the nucleus, this division was performed to separate spectra with higher nuclear decay probability from those with lower probability. As a result, significant modifications were observed in part of the spectra, and the density dependence of such modifications was evaluated.

The space-time evolution of nucleons inside the target nucleus after the pA reaction is not trivial. Meanwhile, since the decay length of the ϕ meson is large compared to the nuclear size, it decays in environments of various densities, such as inside the nucleus, near the nuclear surface, or in vacuum. Thus, the spatial distribution of nucleons after the pA reaction is important for discussing spectral modifications. While past analyses assumed a Woods–Saxon distribution for this spatial distribution, in this study, a more realistic simulation was performed using the Parton-Hadron-String Dynamics (PHSD) transport approach, and the spectral modification was reanalyzed.

In the present analysis, we employed PHSD to simulate the ϕ-meson spectra expected in the experiment and compared them with the measured

data. First, using the simulated spectrum without assuming any in-medium modification, we demonstrated that a significant spectral modification appears in the spectrum that is expected to contain the largest fraction of ϕ mesons decaying inside the nucleus. Next, we examined the spectrum under the assumption of a density dependence that is common across all momentum regions. However, this assumption again failed to reproduce the experimental spectrum. Finally, by introducing a momentum-dependent and density-dependent spectral modification, as suggested by theoretical studies, we succeeded in reproducing the experimental spectrum.

As a result, significant spectral modifications were again observed, similar to previous analysis. However, the density dependence of the modification was found to be smaller than that reported previously, showing better consistency with the latest theoretical predictions.

Contents

List of Figures

List of Tables

Chapter 1

Introduction

1.1 Physics Background

1.1.1 Hadron Mass

Hadrons consist of quarks and gluons. Their fundamental interaction is described by Quantum Chromodynamics (QCD), an SU(3) color gauge theory, which introduces an internal degree of freedom called color with three states. In QCD, observable states must be gauge invariant, and thus the directly observable states are restricted to color-singlet combinations such as mesons and baryons.

In the Standard Model, which unifies QCD with the electroweak theory, the current quark masses are generated through the Higgs field. The quark masses themselves are external parameters in QCD, determined by lattice QCD calculations based on hadron properties measured in experiments. For example, the Modified Minimal Subtraction scheme ($\overline{\mathrm{MS}}$) masses of the up, down, and strange quarks at the scale $\mu = 2\,\mathrm{GeV}$ are $2.16\,\mathrm{MeV}/c^2$, $4.70\,\mathrm{MeV}/c^2$, and $93.5\,\mathrm{MeV}/c^2$, respectively [1]. In contrast, the masses of hadrons formed from two or three quarks are much larger than the sum of the masses of their constituent quarks. For instance, the mass of the proton, the lightest baryon consisting of uud, is $938\,\mathrm{MeV}/c^2$, which is more than one hundred times larger than the sum of its constituent quark masses ($9.02\,\mathrm{MeV}/c^2$). We have been engaged in research on the origin of this hadron mass.

As described in the following sections, QCD in the vacuum is predicted to exhibit spontaneous breaking of an approximate chiral symmetry. This spontaneous breaking of chiral symmetry is believed to provide additional mass to quarks in the vacuum.

1.1.2 Spontaneous Breaking of Chiral Symmetry

In QCD, which describes the strong interaction, the Lagrangian can be written as follows [2]:

$$L = \sum_q (\bar{q_L} i \not{D} q_L + \bar{q_R} i \not{D} q_R) - \frac{1}{4} G^{\alpha}_{\mu\nu} G^{\mu\nu}_{\alpha} + \sum_q \left(\bar{q_L} m_q q_R + \bar{q_R} m_q q_L \right), \quad (1.1)$$

where $G^{\alpha}_{\mu\nu}$ is the field strength tensor of the gluon defined as $G^{\alpha}_{\mu\nu} = \partial_\mu \mathcal{A}^{\alpha}_{\nu} - \partial_\nu \mathcal{A}^{\alpha}_{\mu} - g f_{\alpha\beta\gamma} \mathcal{A}^{\beta}_{\mu} \mathcal{A}^{\gamma}_{\nu}$, where A^{α}_{μ} is the color-octet gluon field and g is the strong-coupling constant, and $\not{D}$ denotes the covariant derivative defined as $\not{D} = \gamma^\mu D_\mu$ and $D_\mu \equiv \partial_\mu + i g t^{\alpha}_{\mathrm{C}} \mathcal{A}^{\alpha}_{\mu}$, where γ^μ is the Dirac matrix and t^{α}_{C} is the color SU(3) generator. For a quark field q, its left- and right-handed components are defined as

$$q_L \equiv \frac{1-\gamma^5}{2} q, \qquad q_R \equiv \frac{1+\gamma^5}{2} q \qquad (q = q_L + q_R), \quad (1.2)$$

with

$$\gamma^5 \equiv i \gamma^0 \gamma^1 \gamma^2 \gamma^3. \quad (1.3)$$

A chiral transformation is defined as an independent flavor rotation of the left- and right-handed components. It can be expressed as a combination of the vector transformation

$$\exp(i \alpha^a T^a), \quad (1.4)$$

and the axial transformation

$$\exp(i \gamma^5 \alpha^a T^a), \quad (1.5)$$

where T^a is $\tau^a/2$ (τ^a is the Pauli matrix) for flavor SU(2) and $\lambda^a/2$ (λ^a is the Gell-Mann matrix) for flavor SU(3).

The Lagrangian (Eq. (1.1)) is invariant under vector transformations, and invariant under axial transformations except for the mass term. For up and down quarks, the mass term can be almost neglected, and hence the Lagrangian approximately has chiral symmetry. The strange quark, while heavier than the up and down quarks, is also frequently treated as massless in many theoretical contexts.

Moreover, hadrons that are mixed under a chiral transformation are referred to as chiral partners, and in the presence of chiral symmetry, these states become degenerate. However, there exists a large mass difference between one such pair of chiral partners, the ρ meson ($775.26\,\mathrm{MeV}/c^2$) and the a_1 meson ($1230\,\mathrm{MeV}/c^2$), indicating that chiral symmetry is broken in reality [1]. This indicates that chiral symmetry is in fact broken. The concept that consistently explains this discrepancy is the spontaneous breaking of symmetry.

Spontaneous breaking of symmetry means that the corresponding symmetry of the Lagrangian is not realized in the ground state. Figure 1.1 illustrates an example of a potential with spontaneously broken symmetry. Although the potential itself has rotational symmetry, the ground states form a continuous set of degenerate minima. Choosing one of them clearly breaks the symmetry.

Quark Condensate

In general, if Q is a generator of a symmetry group and an operator Φ satisfies

$$\langle [iQ, \Phi] \rangle_0 (\equiv \langle 0 | [iQ, \Phi] | 0 \rangle) \neq 0, \tag{1.6}$$

its expectation value is called the order parameter, which characterizes the degree of symmetry breaking [2].

For $SU(2)_A$, the Noether current is

$$A^a_\mu = \bar{q} \gamma_\mu \gamma_5 \frac{\tau^a}{2} q, \tag{1.7}$$

and the corresponding generator is

$$Q^a_5 \equiv \int A^a_0 d^3x. \tag{1.8}$$

Choosing the operator

$$P^a = \bar{q} i \gamma_5 \tau^a q, \tag{1.9}$$

and making use of the appropriate communication relations of the quark fields, one finds that $\langle \bar{q} q \rangle$ serves as the order parameter of the axial transformation. This expectation value is called the quark condensate.

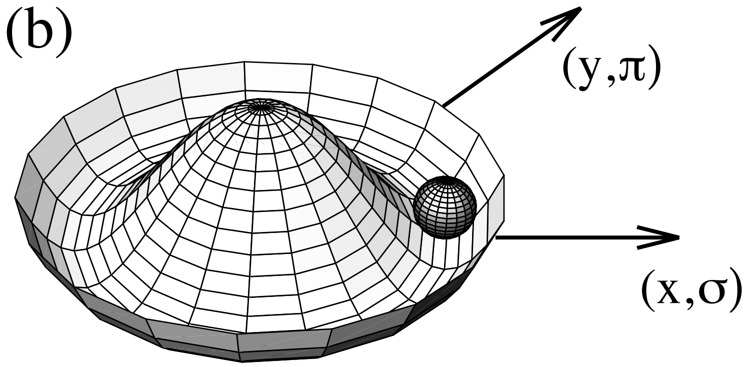

Figure 1.1: Example of the potential which cause spontaneous break of symmetry. Figure is adapted from Ref. [3].

1.1.3 Quark Condensate at Finite Density and High Temperature

The expectation value of the quark condensate is modified in nuclear matter due to the presence of nucleons. At low densities, it can be expressed as a linear sum of contributions from individual nucleons:

$$\langle \bar{q}q \rangle_\rho = \langle \bar{q}q \rangle_0 + \langle N|\bar{q}q|N\rangle \rho + \mathcal{O}(\rho^{4/3}). \tag{1.10}$$

The part of the nucleon mass originating from $\langle \bar{q}q \rangle$, called the pion-nucleon sigma term $\sigma_{\pi N}$, can be written using the explicit chiral symmetry breaking Hamiltonian $H_{X\chi SB}$ as

$$\sigma_{\pi N} = \langle N|H_{X\chi SB}|N\rangle. \tag{1.11}$$

For the QCD Lagrangian,

$$H_{X\chi SB} = -m_q \bar{q}q, \tag{1.12}$$

which leads to

$$\sigma_{\pi N} = m_q \langle N|\bar{q}q|N\rangle. \tag{1.13}$$

Using the Gell-Mann–Oakes–Renner (GOR) relation [4],

$$f_\pi^2 m_\pi^2 = -2m_q \langle \bar{q}q \rangle_0, \tag{1.14}$$

one obtains

$$\langle\bar{q}q\rangle_\rho = \left(1 - \frac{\sigma_{\pi N}}{m_\pi^2 f_\pi^2}\rho + \mathcal{O}(\rho^{4/3})\right)\langle\bar{q}q\rangle_0, \tag{1.15}$$

indicating that the quark condensate decreases approximately linearly with density in the low-density limit.

More detailed calculations have been carried out using chiral perturbation theory [5–9]. Experimentally, from measurements of the pion optical potential by pionic atoms, combined with the in-medium Glashow–Weinberg relation [6],

$$\frac{\langle\bar{q}q\rangle_\rho}{\langle\bar{q}q\rangle_0} \simeq \sqrt{\frac{b_1(0)}{b_1(\rho)}}\left(1 - \gamma\frac{\rho}{\rho_0}\right), \tag{1.16}$$

it has been evaluated that at the nuclear surface density $\rho = 0.098\ \mathrm{fm}^{-3}$, the quark condensate decreases to $(77 \pm 2)\%$ of its vacuum value [10].

As for the temperature dependence, lattice QCD studies have shown that the condensate rapidly decreases near the critical temperature $T_c \sim 160\,\mathrm{MeV}$ [11].

1.1.4 Relation between Quark Condensate and Hadron Mass

The quark condensate is related to hadron masses via QCD sum rule. QCD sum rule connects the correlation function of an operator J,

$$\Pi(q^2) = i\int d^4x\, e^{iqx}\langle 0|T[J(x)J^\dagger(0)]|0\rangle, \tag{1.17}$$

to a sum of perturbatively calculable Wilson coefficients $C_d(q^2)$ and non-perturbative vacuum expectation values,

$$\Pi(q^2) = \sum_d C_d(q^2)\langle 0|\mathcal{O}_d|0\rangle. \tag{1.18}$$

This can further be related to the spectral function of the corresponding hadron, thereby connecting hadron spectral properties with vacuum condensates [12]. Although QCD sum rule relies on certain approximations and assumptions, limiting their precision to about 10–20%, they do not require large-scale computations unlike lattice QCD, and can also be applied at finite density.

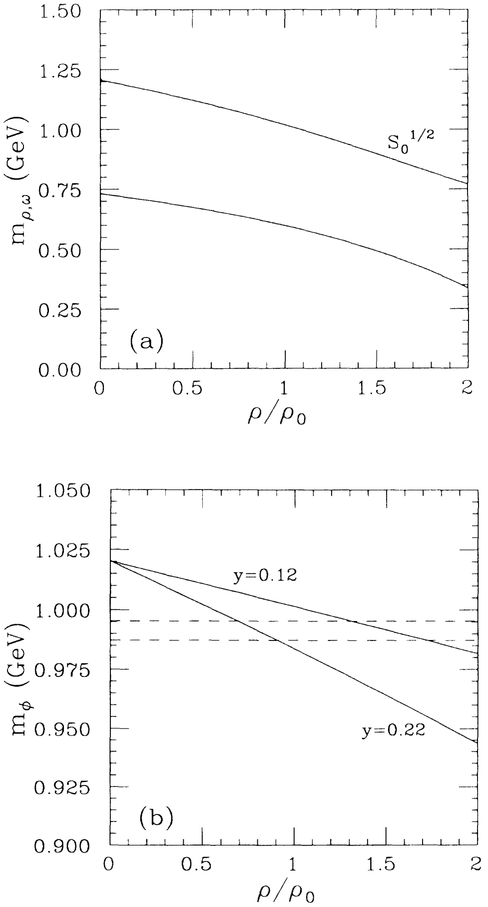

Figure 1.2: Density dependence of the ρ–ω,and ϕ meson masses calculated using QCD sum rules. The momentum of mesons is zero. The upper panel shows the ρ–ω mesons, while the lower panel shows the ϕ meson. In the upper panel, the upper solid line represents the lower bound of the energy calculated by perturbative QCD ($S_0^{1/2}$) in the QCD sum rule analysis. In the lower panel, the two solid lines correspond to the cases where the ratio of the strangeness content to the quark content in the nucleon ($y \equiv 2\langle \bar{s}s \rangle_N / (\langle \bar{u}u \rangle_N + \langle \bar{d}d \rangle_N)$) is 0.12 and 0.22, respectively. The dashed line in the lower panel indicates the sum of the vacuum masses of the main decay products of the ϕ meson, namely K^+K^- and $K^0\bar{K}^0$. Figure is adapted from Ref. [13].

The density dependence of vector meson masses was first calculated in Ref. [13] (Fig. 1.2). In addition to the quark and gluon condensates as vacuum expectation values, four-quark condensates ($\langle(\bar{q}q)^2\rangle$) and twisted-two condensates ($\langle\bar{q}\gamma_\mu D_\nu q\rangle$) were also taken into account. It was concluded that these light vector meson masses decrease approximately linearly with density up to normal nuclear density.

As described above, spontaneous breaking of chiral symmetry plays a crucial role in determining the properties of hadrons. To deepen our understanding of this relation, it is essential to study hadron properties in different environments such as high-temperature or finite-density environments, both theoretically and experimentally.

1.2 ϕ Meson Mass at Finite Density or High Temperature

When hadrons are measured in environments with surrounding hadrons, such as finite density or high temperature, distortions of the mass spectrum due to interactions between decay products and the surrounding hadrons become problematic. Vector mesons are advantageous for such studies because they can decay into lepton pairs, which avoid strong interactions with the surrounding hadrons, thus allowing a more direct discussion of the spectral shape.

Among the vector mesons composed of u, d, and s quarks, there are the ρ, ω, and ϕ. The ρ meson has a large decay width of $147.4\,\mathrm{M}/c^2$, making it less sensitive to spectral modifications. The ω meson has a mass close to that of the ρ meson, which makes it difficult to distinguish their spectra. Moreover, for both ρ and ω, higher-order contributions in QCD sum rules calclations, such as $\langle(\bar{q}q)^2\rangle$ are considered to be significant in their spectra [14].

In contrast, the ϕ meson, although its e^+e^- branching ratio is as small as 3.0×10^{-4}, has no nearby resonance states and a narrow decay width of $4.249\,\mathrm{MeV}/c^2$, and its spectral properties are believed to be dominated by the $\langle\bar{s}s\rangle$ condensate [14].

Experimentally, high-temperature environments are realized in high-energy heavy-ion collisions, while finite-density environments are realized in nuclear targets. Thus, the size of the medium created in such experiments is on the order of nuclei. If the decay width is too narrow, the meson may escape the medium before decaying. However, the typical mean free path of the ϕ meson is about 50 fm for $\beta\gamma(= p/m) = 1$, meaning that a part of them can decay inside the medium.

Therefore, the ϕ meson serves as an excellent probe for studying hadron spectral modifications in different vacuums.

1.2.1 Theoretical Calculations

The properties of the ϕ meson at normal nuclear density have been studied using various approaches, such as vector meson dominance, hidden local symmetry, and chiral effective theories based on $SU(3)$ and $SU(6)$ [15–19]. Many of these studies predict a small mass reduction of about 10 MeV/c^2 and a substantial broadening of the width of about 50 MeV/c^2. Some calculations, however, predict a mass reduction as large as 35 MeV/c^2. Furthermore, lattice QCD has calculated the quantity σ_{sN}, which represents the contribution of the strange quark condensate to the nucleon mass [20].

In parallel, QCD sum rule calculations introduced in Sect. 1.1.4 have been developed to relate the ϕ meson spectral function to vacuum expectation values [13–16, 21–27]. Ref. [25] calculated the mass dependence on σ_{sN} and the density dependence of the mass using lattice QCD inputs for σ_{sN}. Ref. [26] studied the momentum dependence of the mass for the transverse and longitudinal modes separately. These results will be compared with the present study in Sect. 5.3.

1.2.2 Experiments

Various measurements of the ϕ meson spectra and transparency ratios in finite-density and high-temperature environments have been carried out.

KEK-PS E325 Experiment

In the KEK-PS E325 experiment, 12 GeV proton beam was incident on C and Cu targets, and the $\phi \to e^+e^-$ and $\phi \to K^+K^-$ decays were measured [28, 29]. From the e^+e^- decay channel, a significant modification of the ϕ meson spectrum was observed. A comparison with simulations indicated that at normal nuclear density the resonance mass decreases by $3.4^{+0.6}_{-0.7}\%$, while the width increases by a factor of $3.6^{+1.8}_{-1.2}$. Details will be discussed in Chapter 2.

Since the Q value of the $\phi \to K^+K^-$ decay is small, a mass reduction of the ϕ meson is expected to affect its branching ratio. However, in this experiment no significant density dependence of the branching ratio was observed.

Other Experiments

In the COSY-ANKE experiment, a 2.83 GeV proton beam was incident on C, Cu, Ag, and Au targets, and the $\phi \to K^+K^-$ decay was measured [30]. The momentum range of the measured ϕ mesons was 0.6 GeV/c to 1.6 GeV/c. From transparency ratios between C and heavier targets, the momentum dependence of the ϕ meson width at normal nuclear density was extracted using model calculations, showing both an increase from the vacuum value and a rising trend with momentum.

In the CLAS experiment, γ beams up to 4 GeV were incident on ^{2}H, C, Ti, Fe, and Pb targets, and the $\phi \to e^+e^-$ decay was measured [31]. The measured momentum of the ϕ mesons was above 0.8 GeV/c, with an average of 2 GeV/c. From transparency ratios, the ϕ meson width at $\rho = 0.08\,\mathrm{fm}^{-3}$ was concluded to be 23–100 MeV/c^2.

In the LEPS experiment, γ beams of 1.5–2.4 GeV were incident on Li, C, Al, and Cu targets, and the $\phi \to K^+K^-$ decay was measured [32]. The measured ϕ momentum range was 1.0–2.2 GeV/c, with an average of 1.8 GeV/c. No significant modification of the resonance mass or width was observed in the spectra. However, from the A-dependence of the production cross section, the ϕ–nucleon cross section was estimated as 35^{+17}_{-12} mb, much larger than the free-space value of 7.7–8.7 mb. This was interpreted as possible evidence for medium modifications of the ϕ meson.

In the HADES experiment, a 1.7 GeV/c π^- beam was incident on C and W targets, and the $\phi \to K^+K^-$ decay was measured [33]. Although the transparency ratio of the ϕ meson was evaluated, no quantitative values for its width in finite-density nuclear matter were extracted in Ref. [33].

It should be noted that the conversion from cross section to width is not always claimed by the experimental groups themselves, and different values can be deduced from the same data. For example, Ref. [34] used

$$\Gamma(p) = \beta\sigma^*_{\phi N}\rho_0 \tag{1.19}$$

to estimate the ϕ meson width at normal nuclear density as 45–200 MeV/c^2 from CLAS, 97^{+47}_{-31} MeV/c^2 from LEPS, and 36–51 MeV/c^2 from HADES.

For high-temperature environments, the NA60 experiment at CERN SPS measured $\phi \to \mu^+\mu^-$ in 158 AGeV In-In collisions [35]. No significant spectral modification was observed. The fraction of ϕ mesons affected by the medium was found to be consistent with 0%, with an upper limit of 8%. Thus, it was inconclusive whether the ϕ meson undergoes spectral modifications in the medium or whether too few in-medium ϕ mesons were observed.

As described above, numerous experiments have studied the properties of the ϕ meson at high temperature and finite density. In high-temperature experiments, uncertainties arise from the fraction of ϕ mesons actually affected by the medium due to its instability. Discussions based on transparency ratios are highly model dependent, and direct evidence for mass modifications is difficult to obtain. By measuring the dilepton decay of ϕ mesons produced in the relatively static environment of nuclei, direct investigation of spectral modifications becomes possible, overcoming these difficulties. Since the dilepton branching ratio is small, hadron beams are more suitable for such studies. The E325 experiment demonstrated the spectral modification of ϕ mesons in nuclear matter using the 12 GeV pA reaction and evaluated both the mass reduction and width broadening. However, even in this reaction, it is not self-evident that changes in the spatial distribution of the target nucleus are sufficiently small to have no impact on the results. To address such issues, transport calculations are useful.

1.3 Transport Calculations

Transport calculations are numerical approaches that solve the time evolution of many-body systems in which particles interact with each other, such as in nuclear collisions. Various transport models have been developed to describe nuclear collisions over a wide range of eV to TeV energies [36]. The relevant degrees of freedom depend on the energy: at low energies, they are nucleons, Δ resonances, and light mesons such as pions; at higher energies, hadrons containing strange quarks such as kaons and ϕ mesons are included; and at even higher energies, partonic degrees of freedom such as quarks and gluons are employed. The classification of transport approaches and the fundamental equations are described in Appendix. A.

In the present analysis, we employed a transport approach called Parton-Hadron-String Dynamics (PHSD). PHSD has successfully reproduced and interpreted a wide range of experimental data from heavy-ion collision experiments. In particular, for di-leptons, the model has demonstrated good agreement with the invariant mass spectra measured in pp, pA, and AA collisions over a broad range of center-of-mass energies, from a few GeV to several TeV, at experiments such as HADES experiment, STAR experiment, and those at the LHC [37]. Ref. [38] investigated the production and decay of the ϕ meson by employing a T-matrix coupled-channel approach based on the extended SU(6) chiral effective Lagrangian to PHSD. By incorporating newly calculated ϕ-meson production channels and the collisional broadening of the ϕ meson, this approach naturally reproduced the experimentally observed enhancement of ϕ-meson production near the threshold. Ref. [39] studied the production position, production momentum, and production spectrum of ϕ mesons generated in the 12 GeV pC and pCu reactions, which are the same reactions as in the KEK-PS E325 experiment.

1.4 Aim of Present Work

In this thesis, I report on a reanalysis of the $\phi \to e^+e^-$ spectra obtained in the KEK-PS E325 experiment, as presented in Ref. [28]. In the present analysis, we employ the experimental spectra from Ref. [28] but adopt a different fitting function [40].

To incorporate effects not considered in the original analysis of Ref. [28], such as the influence of the pA reaction on the target nucleus, we calculate the time evolution of the spatial density distribution using a BUU-type transport approach called Parton-Hadron-String Dynamics (PHSD). Furthermore, we perform an analysis including the momentum dependence of the ϕ-meson spectral modification, which was not addressed in Ref. [28].

This thesis consists of six chapters. In Chapter 1, we introduce the physics background of the experiment and general aspects of transport calculations. Chapter 2 describes the setup of the KEK-PS E325 experiment the analysis carried out in Ref. [28], focusing on the parts relevant to the present study. In Chapter 3, we present details of the initialization and time evolution in the PHSD transport calculations used in this work. Chapter 4 discusses the issues encountered when implementing PHSD into the analysis of the experimental data, as well as the treatment of experimental effects and spectral modifications. In Chapter 5, we show the results obtained from the fits to the experimental spectra and compare them with theoretical calculations, other experiments, and previous analyses. Finally, Chapter 6 summarizes the conclusions drawn from the present analysis.

Chapter 2

KEK-PS E325 Experiment

In the KEK-PS E325 experiment, the decays of vector mesons ρ, ω, and ϕ into e^+e^- or K^+K^- were measured using 12 GeV pC and pCu reactions [28, 29, 41–43]. The experimental data used in the present analysis, such as the invariant mass spectra of e^+e^- pairs and the momentum distributions, were not newly analyzed in this study, but were already analyzed in Refs. [28, 44]. In this chapter, we summarize the experimental setup and analysis described in those references, focusing on the aspects relevant to the present study.

2.1 Experimental Setup

2.1.1 Accelerator Facility and Beam Line

The experiment was conducted in two separate periods, in 2001 and 2002, at the EP1-B beam line of the 12 GeV Proton Synchrotron (PS) at KEK. A top view of the beam line is shown in Fig. 2.1.

2.1.2 Beam

Proton beam with kinetic energy of 12 GeV and an intensity of 6–9 $\times$ 10^8 per spill (with one spill lasting 2 s) was used. The horizontal beam profile is shown in Fig. 2.2. This profile was measured from the interaction rate while the carbon target (described later) was rotated by 90° with respect to the vertical axis to serve as a narrow target in the horizontal direction, and the beam was swept horizontally. The horizontal beam position was calculated as $x = 0.109(V - V_0)$, where V is the voltage of the B22 magnet shown in

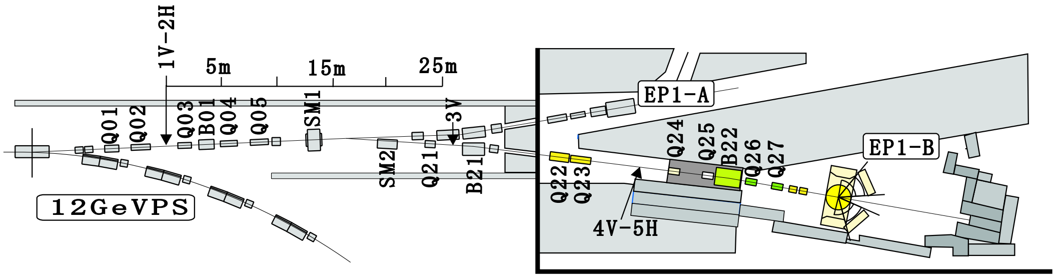

Figure 2.1: Top view of the KEK-PS EP1-B beam line. Figure is adapted from Ref. [44].

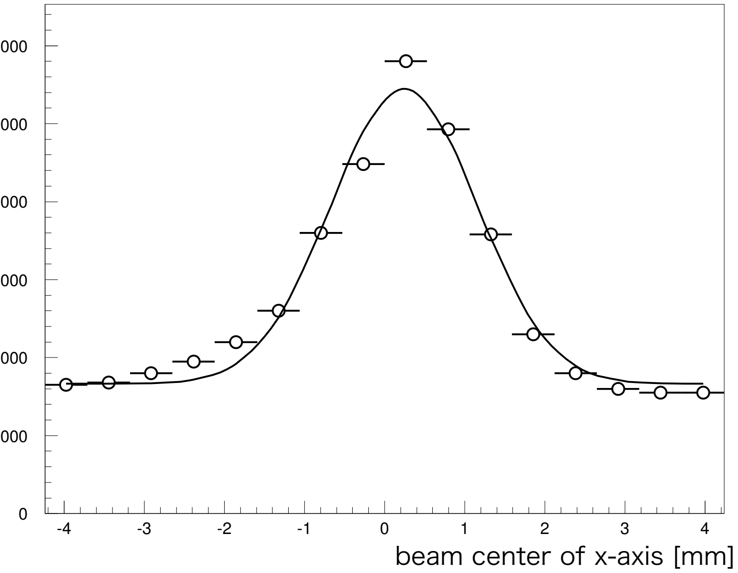

Figure 2.2: Beam-position dependence of the interaction rate in the horizontal direction. Circles represent the measured data. Solid curve shows the result of a Gaussian fit convoluted with the target width (1 mm). Figure is adapted from Ref. [44].

Fig. 2.1. The standard deviation of the horizontal beam profile was 1.59 mm in the 2001 run and 0.83 mm in the 2002 run.

2.1.3 Targets

Carbon (C) and copper (Cu) targets were installed in a comb-like configuration along the beam axis, as shown in Fig. 2.3. In the 2001 run, one carbon target and two copper targets were installed. In the 2002 run, one carbon target with twice the thickness and four copper targets (twice the number) were used. To suppress γ conversions in the targets, the radiation length of each target was limited to approximately 0.5% at most. The details of the targets are summarized in Table 2.7.

2.1.4 Detectors

Top and side views of the spectrometer are shown in Figs. 2.4 and 2.5, respectively. Hereafter, the beam direction is taken as the z-axis, the vertically upward direction as the y-axis, and the remaining axis as the x-axis.

In the e^+e^- measurement described in Ref. [28], two types of tracking detectors and a two- or three-stage electron identification system were employed. The spectrometer covered an acceptance of $\pm 12^\circ$ to $\pm 90^\circ$ in the horizontal direction and $\pm 22^\circ$ in the vertical direction, corresponding to $0 < p_T < 1$ GeV$/c$, $0.5 < y < 2.0$, and $0.5 < \beta\gamma < 3.5$ for ϕ mesons.

The tracking detectors consisted of the cylindrical drift chamber (CDC) and the barrel drift chambers (BDC). Although a vertex drift chamber (VDC)

Table 2.1: Detail of the targets. The values of z position are the design values.

Year	2001		2002	
Material	C	Cu	C	Cu
Quantity	1	2	1	4
z position [mm]	0	± 48	0	-43, -23, 24, 48
Width [mm]	25	25	10	10
Height [mm]	25	25	25	25
Thickness [mg cm^{-2}]	92	2×73	184	4×73
Interaction length [%]	0.11	2×0.054	0.21	4×0.054
Radiation length [%]	0.21	2×0.57	0.43	4×0.57

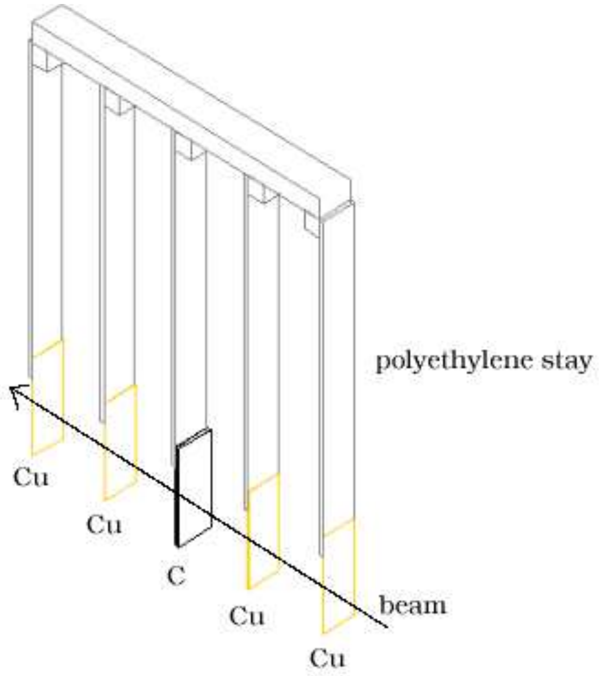

Figure 2.3: Schematic view of the targets and jigs (2002 configuration). Figure is adapted from Ref. [44].

was installed in the innermost layer and also served as a tracking detector, it was not used in the analysis in Ref. [44] because it significantly affected the measurable e^+e^- invariant mass range depending on the target.

For electron and positron identification, two types of gas Cherenkov counters, the front gas Cherenkov counters (FGC) and the rear gas Cherenkov counters (RGC), as well as three types of lead-glass calorimeters, the rear lead-glass calorimeter (RLG), the side lead-glass calorimeter (SLG), and the forward lead-glass calorimeter (FLG), were used. Since the acceptance of each detector differs, as summarized in Table 2.2, electron identification was performed using a combination of two or three of these detectors.

The start timing counters (STC), a scintillator located 380 mm from the center of the spectrometer in the horizontal plane, covered an acceptance of ±12° to ±60° in the horizontal direction and ±23° in the vertical direction. While the STC was originally used to detect the track timing for kaon identification via the time-of-flight (TOF) method, it also served as one of the trigger components for the e^+e^- measurement.

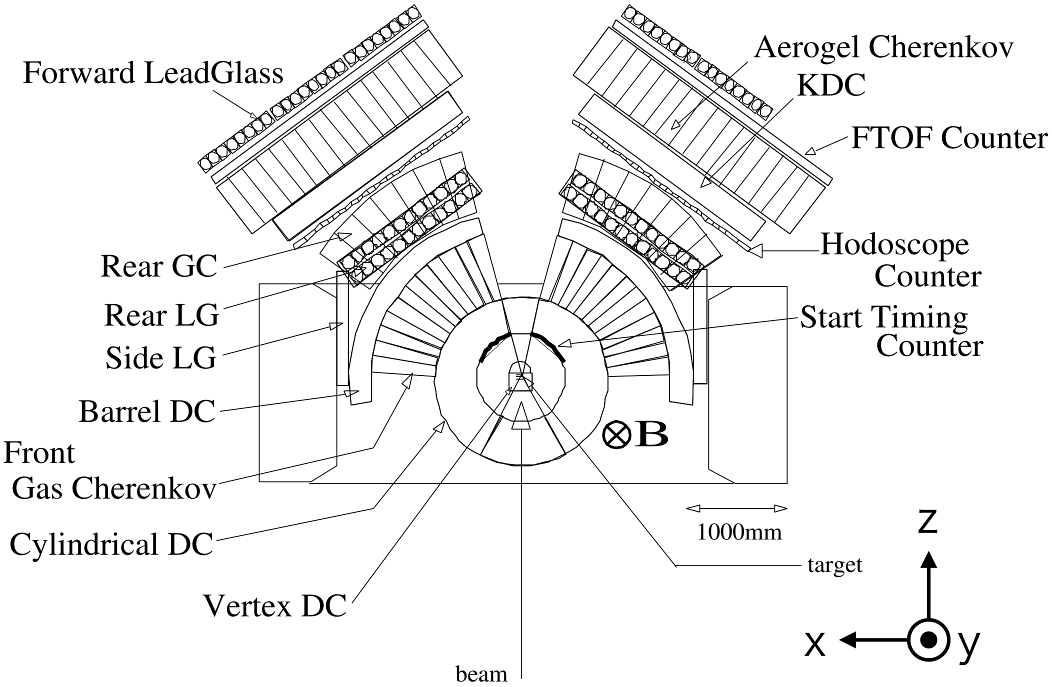

Figure 2.4: Top view of the spectrometer. Figure is adapted from Ref. [44].

Other detectors not described here were used for K^+K^- measurements and are omitted in this thesis.

The position resolution and the efficiency of the tracking detectors were evaluated as summarized in Table 2.3. The CDC consisted of 10 layers as shown in Fig. 2.6, while the BDC consisted of four layers as shown in Fig. 2.7. The position resolution was modeled as a double Gaussian, with σ_1 as the

Table 2.2: Acceptance of the electron identification detectors.

Layer	Detector	Horizontal Acceptance [°]	Vertical Acceptance [°]
1	FGC	±12–±90	±23
2	RGC	±12–±54	±6
2	RLG	±12–±54	±9–±23
2	SLG	±57–±90	±23
3	FLG	−40–−12, 12–54	±7

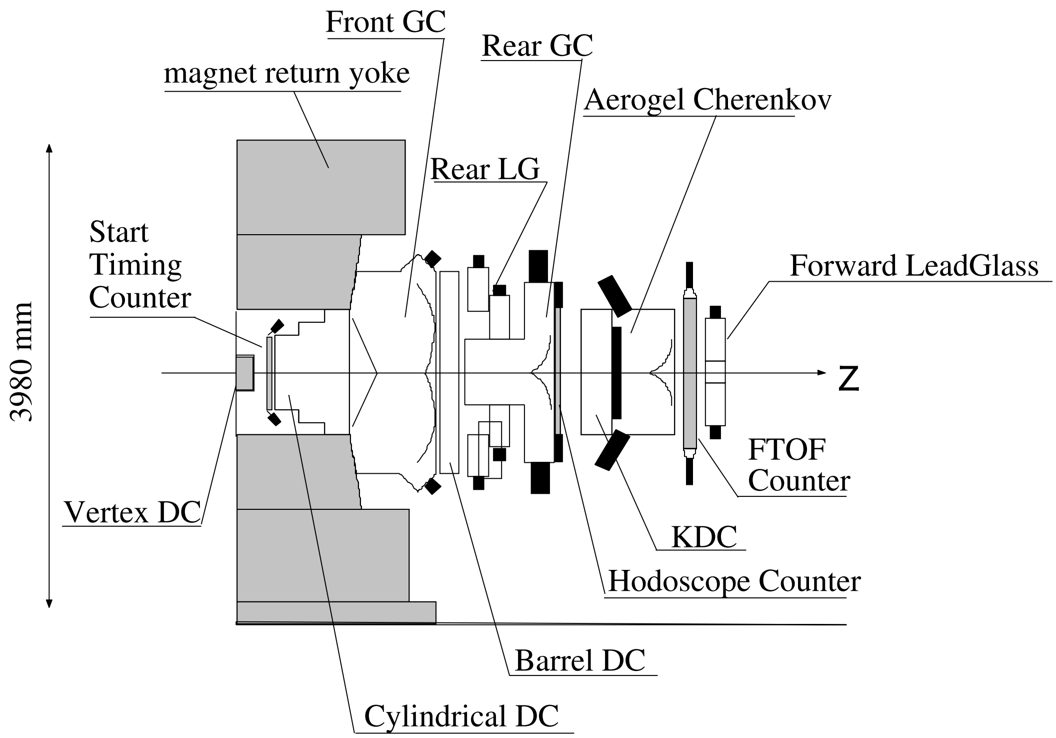

Figure 2.5: Side view of the spectrometer. Figure is adapted from Ref. [44].

main component, σ_2 as the secondary component, and the ratio defined as the secondary-to-main component.

The momentum dependence of the detection efficiency for the electron identification detectors was evaluated using the function: $f(p) = a - b/p^c$. For the performance evaluation, electron samples originating from γ conversions and π^0 Dalitz decays, with the trigger bias removed, were used. The parameters obtained from the fit are summarized in Table 2.4.

2.1.5 Spectrometer Magnet

The spectrometer magnet, as shown in Figs. 2.4 and 2.5, was a dipole-type magnet with a maximum field strength of 0.71 T. The integrated magnetic field from the center to the radius of the Barrel Drift Chamber (BDC), located at 1680 mm, was 0.81 T m.

The magnetic field used in the analysis of Ref. [44] was derived from a combination of measurements taken in a limited spatial region and field calculations using TOSCA [45]; a software package which solves non-linear magnetostatic or electrostatic field and current flow problems in three dimensions. The procedure was as follows:

Table 2.3: Position resolution and detection efficiency of tracking detectors. The values of σ_2 and ratio are common in the same super layer.

Super layer	Layer	σ_1 [mm]	σ_2 [mm]	Ratio	Efficiency [%]
CDC inner	X	0.197	0.595	0.436	96.1
	X'	0.203			96.8
	U	0.286			90.2
CDC middle	V	0.238	0.644	0.367	94.6
	V'	0.217			95.7
	X	0.183			94.6
	X'	0.181			93.1
CDC outer	U	0.285	0.718	0.395	97.2
	X	0.212			95.7
	X'	0.261			94.2
BDC	X	0.292	0.661	0.488	99.0
	X'	0.289			99.1
	U	0.340			99.0
	V	0.261			96.8

Table 2.4: Efficiency parameters for electron identification counters.

Detector	a	b	c
FGC	0.867	0.207	0.76
RGC	0.623	1.8×10^{-6}	9.3
RLG	0.921	9.9×10^{-6}	8.2
SLG	0.882	1.7×10^{-4}	6.8
FLG	0.913	1.2×10^{-6}	10.0

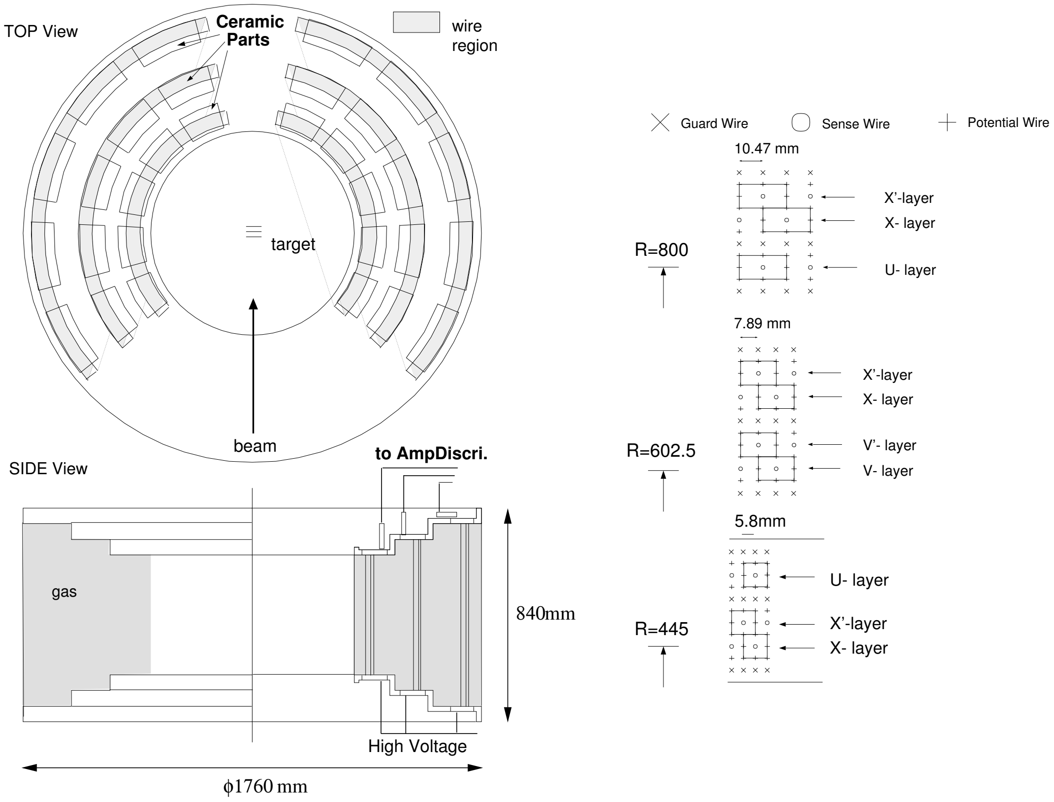

Figure 2.6: Schematic view and cell structures of CDC. Figure is adapted from Ref. [44].

- Simulate the trajectories of charged particles using the measured magnetic field to determine hit positions in the drift chambers.
- Reconstruct the momentum by applying the Runge-Kutta method to the calculated hit positions in conjunction with the computed magnetic field.

Using this method, the inconsistency in reconstructed momenta for charged particles in the range of $0.5\,\mathrm{GeV}/c$ to $2.0\,\mathrm{GeV}/c$ was found to be $0.2 \pm 0.3\%$. The calculated magnetic field was scaled accordingly and used in the analysis.

During both the 2001 and 2002 runs, some of the electromagnetic coils were malfunctioning. The magnet was equipped with seven coils each on the upper and lower sides. Prior to the 2001 run, two coils on the upper side failed and became unusable. To maintain vertical symmetry, two coils

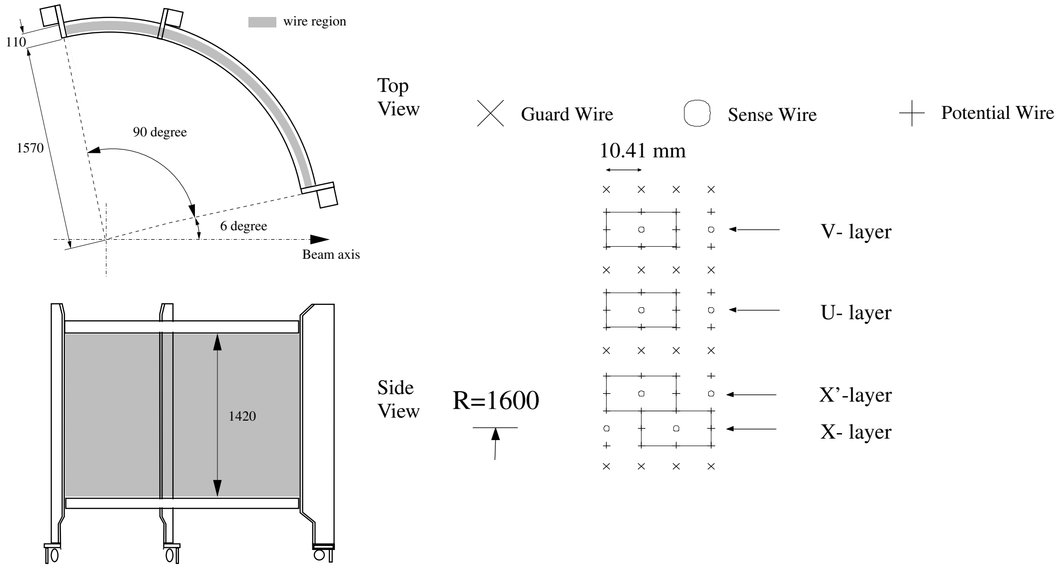

Figure 2.7: Schematic view and cell structures of BDC. Figure is adapted from Ref. [44].

on the lower side were also turned off, and the current was increased to 14/10 of the normal value for operation. Furthermore, partway through the 2001 run, one additional upper coil failed. To preserve the integrated magnetic field strength, all coils on the lower side were turned back on, resulting in a configuration with four active coils on the upper side and seven on the lower side. In this asymmetric configuration, the current was adjusted to 14/11 of the standard value. The magnetic field in this non-symmetric condition was recalculated using TOSCA. To validate this asymmetric field configuration, the absolute magnetic field was measured at several heights around the spectrometer center. The deviation from the calculated field was found to be $0.49 \pm 0.03\%$. This discrepancy was used as a scaling factor for the magnetic field in the analysis of Ref. [44].

2.1.6 Trigger

In the trigger system, track candidates were selected based on the horizontal hit patterns in Layer 1 (FGC) and Layer 2 (SLG, RLG, SGC). The hit patterns were designed to select particles with momentum greater than $0.4\,\mathrm{GeV}/c$. Due to the high hit rate, the most forward segment of the FGC (each segment covering 6°) was excluded from the trigger logic.

A trigger was generated when at least one track candidate was found in each of the left and right arms, and both arms of the STC registered hits. The STC was used to select the e^+e^- pairs generated on the targets.

2.2 Previous Analysis

In the previous analysis, the e^+e^- invariant mass distribution was used to discuss the presence or absence of the in-medium modification of the ϕ-meson spectrum, and the density dependence of the modification was evaluated from its magnitude. The vacuum width of the ϕ meson is $4.249\,\mathrm{MeV}/c^2$ [1], and assuming $\beta\gamma = 2$, it typically travels about 92 fm before decaying. Since the radii of C and Cu nuclei are less than 10 fm, the majority of the ϕ mesons observed in this experiment are considered to have decayed in vacuum. In simple terms, the probability of in-medium decay increases as the nuclear radius becomes larger and the ϕ-meson velocity becomes smaller. Therefore, in the previous analysis, the spectra obtained for each target nucleus were classified into three categories using the parent particle $\beta\gamma$: $\beta\gamma < 1.25$, $1.25 \leq \beta\gamma < 1.75$, and $\beta\gamma \geq 1.75$, and the analysis was performed for each category. The experimentally obtained e^+e^- invariant mass spectra are shown in Fig. 2.8. The detail of the analysis concerning the e^+e^- pairs are described in Appendix B. The spectra are categorized into six groups according to the target nucleus (C or Cu) and the $\beta\gamma$ of the parent particle: $\beta\gamma < 1.25$, $1.25 \leq \beta\gamma < 1.75$, and $\beta\gamma \geq 1.75$. The bin width is set to $1/150\ \mathrm{GeV}/c^2$ ($\sim 6.7\,\mathrm{MeV}/c^2$).

To interpret these spectra, we performed a detector simulation using Geant4 [46–48], a Monte Carlo simulator for particle transport in matter, to include the experimental effects including the detector resolution. Internal radiative correction according to Ref. [49] was also taken into account in the di-electron decay of ϕ meson. The detail of these effects is explained in Sect. 4.3.2 and 4.3.3. As a mass distribution of ϕ mesons, the Breit–Wigner form and also a simple spectral-modification model were used as described in following section. Then, the simulated mass shapes were compared to the data.

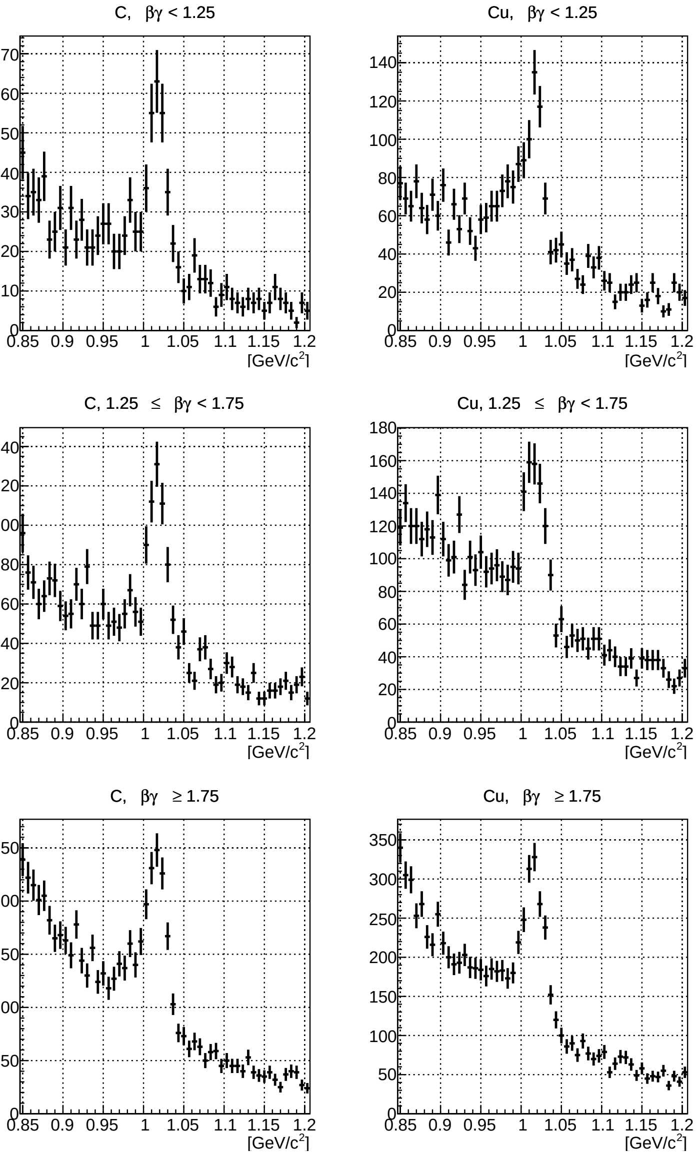

Figure 2.8: e^+e^- invariant mass spectra obtained in the experiment. The classification of spectra is described in the main text. The bin width is 1/150 GeV/c^2.

2.2.1 Parameterization of Spectral Modification

The spectral function was assumed to follow a non-relativistic Breit–Wigner distribution, expressed as:

$$A(m) = \frac{1}{2\pi}\frac{\Gamma_\phi}{(m - m_\phi)^2 + (\frac{\Gamma_\phi}{2})^2}, \tag{2.1}$$

where Γ_ϕ is the width of ϕ meson and m_ϕ is the resonance mass of ϕ meson.

The in-medium spectral modifications were parameterized by introducing a density dependence to both the resonance mass m_ϕ and the total width Γ_ϕ, with parameters k_1 and k_2 as follows:

$$m_\phi(\rho) = (1 - k_1\frac{\rho}{\rho_0})m_0, \tag{2.2}$$

$$\Gamma_\phi(\rho) = (1 + k_2\frac{\rho}{\rho_0})\Gamma_0, \tag{2.3}$$

where ρ is the baryon density, ρ_0 is the normal nuclear density, and m_0 and Γ_0 are the pole mass and the width of ϕ meson in vacuum. Regarding Eq. (2.2), calculations based on QCD sum rules [13] have shown that the dependence is approximately linear up to normal nuclear density. Although there is no theoretical foundation for Eq. (2.3), the values calculated in Ref. [50] were found to be well fitted by a linear function as shown in Fig. 2.9.

Ideally, the partial width for the e^+e^- decay channel should also be parameterized independently. However, due to the limited statistics of the experimental data to increase the free parameters, this was not done. In the nuclear medium, the total width of the ϕ meson is expected to change from its vacuum value due to modifications in the kaon and anti kaon masses, which are the primary decay products, and interactions with surrounding nucleons. On the other hand, the partial width for the e^+e^- decay is determined by the overlap of the s and $\bar{s}$ quark wave functions. There is little theoretical basis to expect the partial width to vary in the same way as the total width, but it is also unlikely that it remains completely unchanged. Therefore, we considered two extreme cases for the density dependence of the e^+e^- partial width:

1. A case in which it changes proportionally with the total width, following the same density dependence as Eq. (2.4).

$$\Gamma_\phi^{ee}(\rho) = (1 + k_2\frac{\rho}{\rho_0})\Gamma_0^{ee}, \tag{2.4}$$

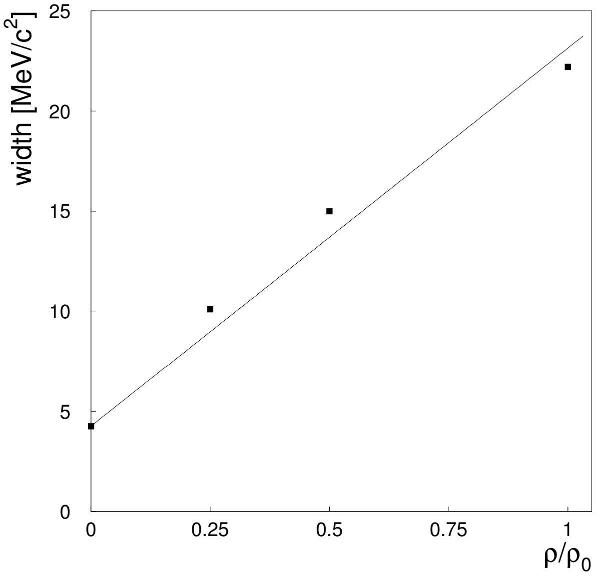

Figure 2.9: Width of the ϕ meson in nuclear matter calculated in Ref. [50]. Points represent the calculated values, taken from Fig. 4 of Ref. [50]. Line shows the result of a linear fit that passes through the width at vacuum, with $\Gamma_\phi(\rho)/\Gamma_\phi(0) = 1 + 4.4(\rho/\rho_0)$ Figure is adapted from Ref. [44].

where Γ_0^{ee} is the $\phi \to e^+e^-$ partial decay width in vacuum and the value of k_2 is common with Eq. (2.3).

2. A case in which it remains unchanged from the vacuum value.

2.2.2 Generation of ϕ Meson Mass and Momentum at Decay

The production and decay of ϕ mesons were simulated as follows. First, the production position of a ϕ meson was assumed to follow the spatial distribution of the nuclear density in the target. This assumption is based on the observed A-dependence of the ϕ meson production cross section in the E325 experiment, which follows $\sigma \propto A^1$ [43]. The nuclear density distribution was modeled using the Woods–Saxon form:

$$\rho(r) = \frac{N}{1 + \exp(\dfrac{r-R}{\tau})}\rho_0, \tag{2.5}$$

where N is normalization factor, R is half density radius of the nucleus, and τ is the surface diffuseness. The parameters are shown in Table 4.4. The parameters for Cu were obtained from pA scattering experiments [51], while those for C were calculated using $R = 1.02A^{1/3}$ and $\tau = 2.5/4.4$. N was determined such that the integral of $\rho(r)$ matched the number of nucleons, given the values of ρ_0, R, and τ. The momentum distribution of ϕ meson is taken from JAM [1] 1.01.00 [52], a hadronic cascade model, at the decay of phi meson in the code. The distribution is consistent with the observed $\phi \to e^+e^-$ events.

The momentum and mass at the decay point were simulated as follows:

- Assuming that the momentum of the ϕ meson remains unchanged and its mass varies according to Eq. (2.2), the velocity calculated from these values is used to propagate the ϕ meson from its production point in steps of 0.1 fm. Density dependent pole mass is used in the propagation.
- The local density at the middle point of the step is used to calculate the decay probability in the step through the density dependent mass and width.
- With a probability proportional to the partial width divided by the total width, it was determined whether the decay resulted in an e^+e^- final state.
- The decaying mass was randomly selected according to the density-dependent Breit–Wigner shape, namely, Eqs. (2.1) (2.2), and (2.3).
- Given the decay density, a mass was randomly selected according to Eqs. (2.1), (2.2), and (2.3).

If the flight distance exceeded 100 fm without decay, the ϕ meson was forced to decay at that point.

---

[1] Jet AA Microscopic transport model

Table 2.5: Parameters of Eq. (2.5) used in Ref. [28].

Nucleus	ρ_0 [fm^{-3}]	R [fm]	τ [fm]	N
Carbon	0.17	2.3	0.57	0.9
Copper		4.1	0.50	1.2

Corrections for experimental effects that influence the observed invariant mass spectrum, such as detector acceptance and resolution, are shared with those in the present analysis and are described in Sect. 4.

2.2.3 Fitting to Experimental Data

The simulated momentum distribution of ϕ mesons was found to be in good agreement with the experimentally obtained distribution, as shown in Fig. 2.10. The experimental momentum distribution was extracted through the following procedure:

- The e^+e^- invariant mass region from $0.95\,\mathrm{GeV}/c^2$ to $1.05\,\mathrm{GeV}/c^2$ was defined as the ϕ mass region, which contains both signal and background. The sideband regions were defined as $0.85\,\mathrm{GeV}/c^2$ to $0.95\,\mathrm{GeV}/c^2$ and $1.05\,\mathrm{GeV}/c^2$ to $1.15\,\mathrm{GeV}/c^2$, which are assumed to contain only background.
- The invariant mass distribution in the sideband regions was fitted with a quadratic polynomial to estimate the background contribution in the ϕ mass region.
- The momentum distribution of events in the sidebands was then used as the background momentum distribution. It was normalized using the number of background events estimated in the ϕ mass region and subtracted from the total momentum distribution in that region.

To fit the experimental invariant mass spectra, the simulated $\phi \to e^+e^-$ mass distribution was combined with a background component modeled by a quadratic function. Fit was then performed to the data, with the three coefficients of the quadratic function and the yield of the ϕ meson signal treated as free parameters. The fit was carried out over the range $0.847\,\mathrm{GeV}/c^2$ to $1.207\,\mathrm{GeV}/c^2$, divided into 54 bins.

2.2.4 Previous Results

In Ref. [28], the simulation described above was first performed without assuming any spectral modifications. The result of the fit to the experimental data under this assumption is shown in Fig. 2.11. Out of the six spectra, five were well reproduced. However, for the spectrum with the lowest $\beta\gamma$ among

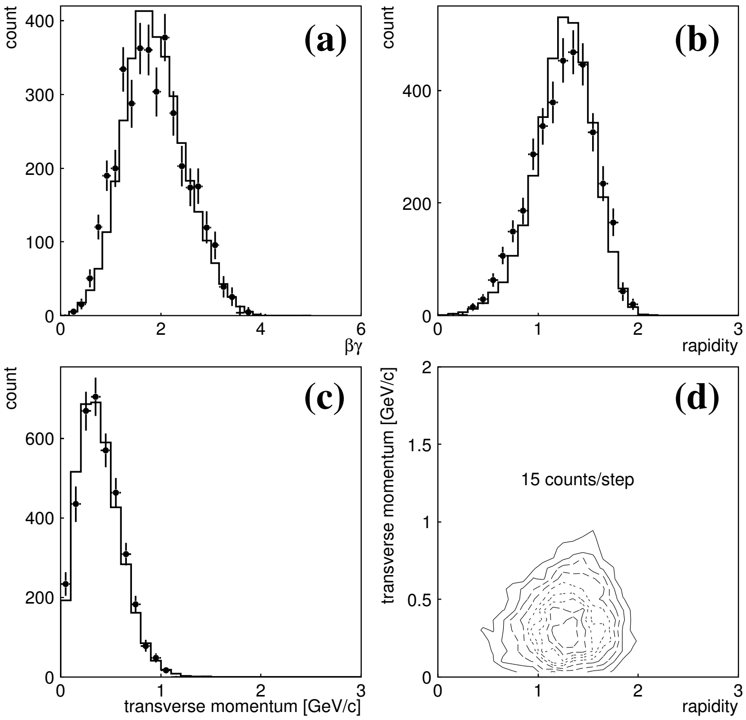

Figure 2.10: Momentum distributions of ϕ mesons, as functions of (a) $\beta\gamma$, (b) rapidity, (c) transverse momentum, and (d) transverse momentum versus $\beta\gamma$. Circles with error bars represent the real data and lines represent the simulation of Ref. [28]. Figure is adapted from Ref. [44].

the Cu targets, the fit yielded a $\chi^2/\text{dof} = 83/50$, which was rejected at a 99% confidence level.

Assuming that the discrepancy originates from the region $0.947\,\text{GeV}/c^2$ to $1.007\,\text{GeV}/c^2$, the amount of excess in this region was estimated as follows:

- A fit was performed in the same manner as above, excluding the excess region.
- The number of ϕ mesons N_ϕ excluding the excess was determined from the scale parameter of the signal component in the fit.
- The number of excess events N_{ex} was calculated by subtracting the fit function from the experimental data in the excess region.

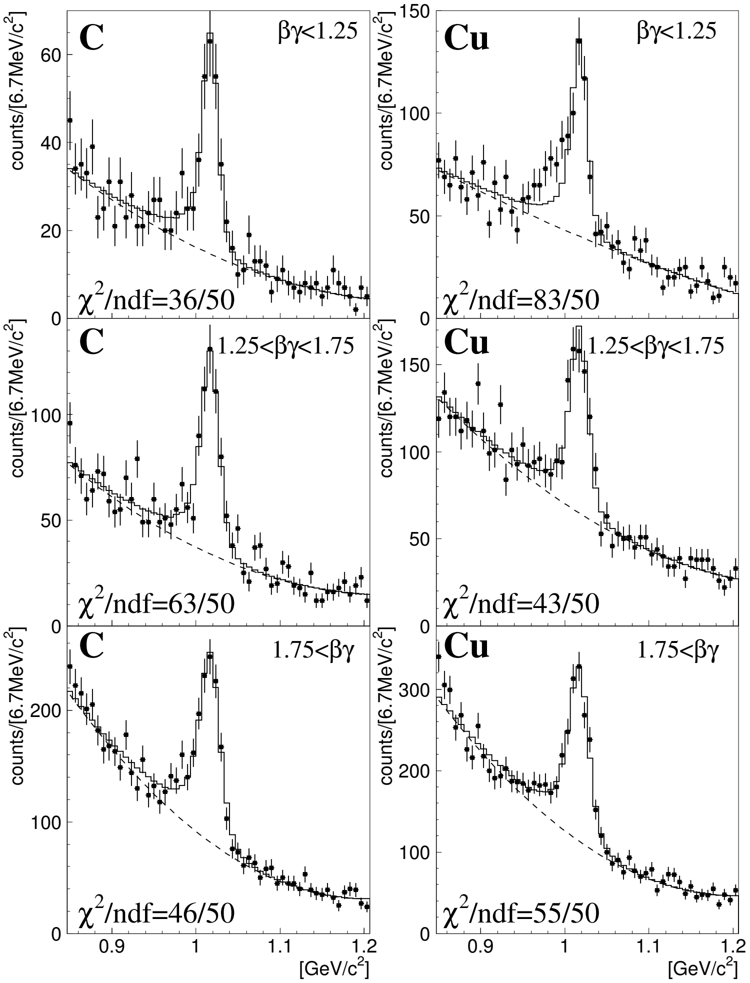

Figure 2.11: Fit result from Ref. [44] without assuming spectral modifications. Data points with error bars represent the experimental data, and the solid curve shows the fit result. Figure is adapted from Ref. [44].

The target nucleus and $\beta\gamma$ dependence of the excess ratio $(N_{\mathrm{ex}}/(N_\phi + N_{\mathrm{ex}}))$, including systematic uncertainties, are shown in Fig. 2.12. As shown, a statistically significant excess was observed in the Cu target data with the lowest $\beta\gamma$.

Next, spectral modifications were introduced to the simulated spectra assuming the forms given in Eqs. (2.2) and (2.3). Fits were performed for various combinations of k_1 and k_2, using the same values across all six spectra.

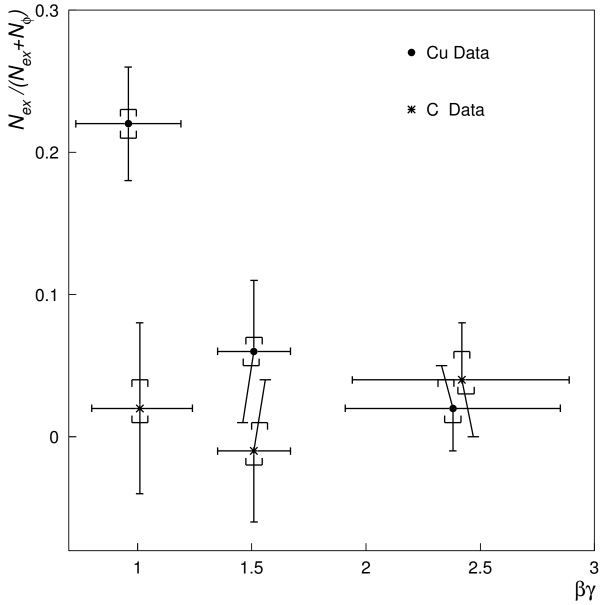

Figure 2.12: Dependence of the excess ratio on target nucleus and $\beta\gamma$. Vertical error bars indicate statistical uncertainties, while brackets represent systematic uncertainties. Horizontal error bars show the standard deviation of $\beta\gamma$ for each spectrum. Figure is adapted from Ref. [44].

Figure 2.13 shows the dependence of the total χ^2 from all six spectra on the parameters k_1 and k_2 obtained in Ref. [28]. The best-fit values of k_1 and k_2 for each case of the assumption of the partial width are summarized in Table 2.6. Figure 2.14 shows the fit results for the best-fit k_1 and k_2 values in each case.

In both cases, $k_1 \sim 0.034$, indicating a significant shift in the resonance mass. Furthermore, the case where the partial width follows Eq. (2.4) is favored, as the total χ^2 is decreased by 4.4 compared to the constant partial width case.

Table 2.6: Best-fit values of k_1 and k_2 and χ^2/dof obtained in Ref. [28].

Partial width	k_1	k_2	χ^2/dof
Density dependent	$0.034^{+0.006}_{-0.007}$	$2.6^{+1.8}_{-1.2}$	316.4/298
Constant	$0.033^{+0.011}_{-0.008}$	$0^{+5.6}$	320.8/298

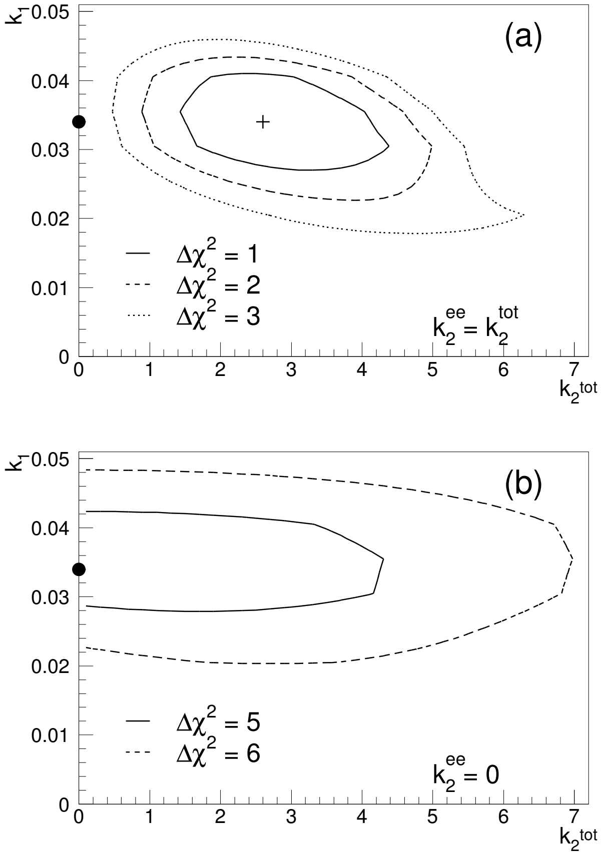

Figure 2.13: χ^2 dependence on k_1 and k_2 for the combined fit of all six spectra (Ref. [28]). Top: assuming density-dependent partial width (Eq. (2.4)). Bottom: assuming constant partial width. The cross and black dot indicate the best-fit points in each case. Contour lines represent constant $\Delta\chi^2$ values from the minimum. Figure is adapted from Ref. [44].

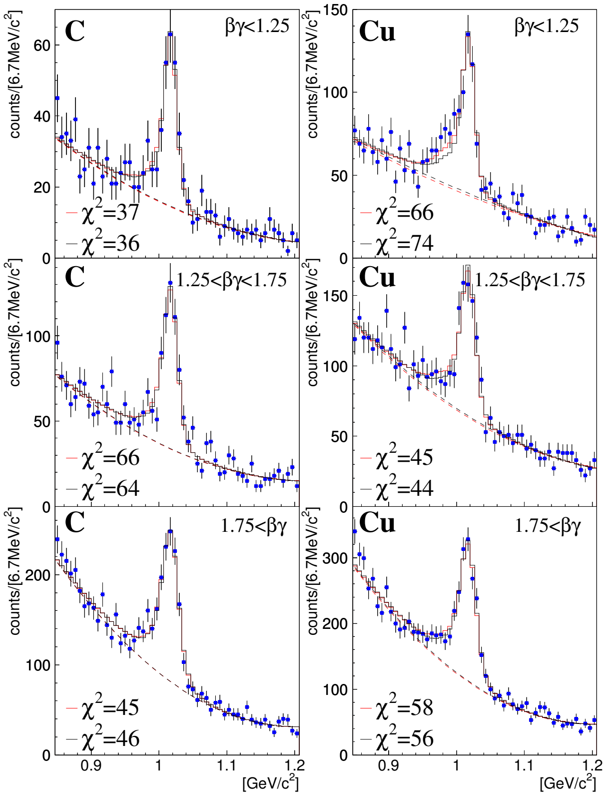

Figure 2.14: Fit results with spectral modification of Ref. [28]. Blue points represent the experimental data. Red solid and dashed curves correspond to the fit result and background component, respectively, for the density-dependent partial width (Eq. (2.4)). Black solid and dashed curves correspond to the same for the fixed partial width case. Figure is adapted from Ref. [44].

2.3 Improvements in Present Analysis

As described in Sect. 2.2.2, in the simulation of Ref. [28], the spatial distribution of baryon density was assumed to follow a Woods–Saxon distribution without time evolution, and the production position of the ϕ meson was taken to be proportional to this density distribution. However, in reality, the production position of ϕ mesons is not necessarily proportional to the density, and in pA reactions the target nucleus may undergo some space-time evolution. Therefore, in the present analysis, we newly employed the PHSD transport approach in order to perform a more realistic simulation that accounts for these effects and to reanalyze the experimentally obtained spectra.

Table 2.7: Comparison of the use of transport calculations in previous analyses and in the present analysis. The details of their application in the present analysis will be described later in Chapter 4.

	Previous analysis [28]	Present analysis
Experimental spectra	Common	
Production position (not used directory)	Proportional to Woods–Saxon	Output of PHSD
Momentum	Initial momentum of JAM. Not changed.	Based on PHSD
Density	Woods–Saxon	Based on PHSD
Decay	Calculated from Eq. (2.3)	Based on PHSD

Chapter 3

PHSD Transport Approach

3.1 Features of PHSD

The PHSD model is a type of BUU-based transport approach, but instead of using the BUU equation (Eq. (A.5)), it is based on the Cassing–Juchem formulation of the Kadanoff–Baym equations, which allow for the treatment of off-shell particles [53–56]. The Kadanoff–Baym equations provide a quantum-theoretical description of transport phenomena, but their direct solution requires an impractically large computational effort. Therefore, practical approximations are employed, among which the Cassing–Juchem approach is one of those.

Although not directly relevant to the 12 GeV pA reactions studied in this work, a notable feature of PHSD is its capability to describe not only hadronic matter but also non-equilibrium partonic phases such as the quark–gluon plasma (QGP).

In the following sections, we explain the specific procedure of the calculation. This analysis focuses solely on 12 GeV pC and pCu reactions.

3.2 Procedure

The general procedure of the simulations performed in PHSD is as follows:

- Initialization: The initial positions and momenta of the nucleons constituting the target and projectile (or pions in the case of a pion beam) are determined.

- Time evolution: At each time step, the following procedures are carried out:
  - Density calculation: The density used for the calculation of the potentials is evaluated.
  - Collisions: Collisions among baryons, between mesons and baryons, and among mesons are computed.
  - Propagation: The positions and momenta of hadrons are updated using the potentials.
  - Virtual e^+e^- decays: The probabilities of Dalitz or di-lepton decays of mesons are calculated. The usage of this procedure is explained in Sect. 3.7.2.

Since the procedures related to partons are not relevant to the present analysis, they are omitted.

3.3 Initialization

The initial positions and momenta of the nucleons in the target and projectile nuclei are first determined in the laboratory frame. The spatial density distribution and nuclear radius are used to determine the initial state. The spatial density distribution is based on a shell model for light nucleons (^{12}C) and on the Woods–Saxon distribution for heavier nucleons (^{64}Cu), as follows:

$$\rho(r) = \begin{cases} \dfrac{4}{(a\sqrt{\pi})^3}(1 + \dfrac{A-4}{6}(\dfrac{r}{a})^2)\exp(-(\dfrac{r}{a})^2) & \text{if } A \leq 16, \\ \dfrac{N\rho_0}{1+\exp(\dfrac{r-R}{\tau})} \quad (N\rho_0 = \dfrac{3A}{4\pi R^3(1+\dfrac{\pi\tau}{R})^2}) & \text{if } A > 16, \end{cases} \tag{3.1}$$

$$R = \begin{cases} 2.3 & \text{if } A = 12, \\ 1.123A^{1/3} - 0.941A^{-1/3} & \text{if } A > 16, \end{cases} \tag{3.2}$$

where R [fm] is nuclear radius (half-density radius), A is mass number of nuclei, a is related to nuclear size and 1.64 fm for ^{12}C, τ [fm] is surface thickness, and N is a normalization factor. The spatial density distribution of ^{12}C and ^{64}Cu is shown in Fig. 3.1.

In the present analysis, the initial position and momentum of the projectile proton were set to be identical across all events within the same ensemble.

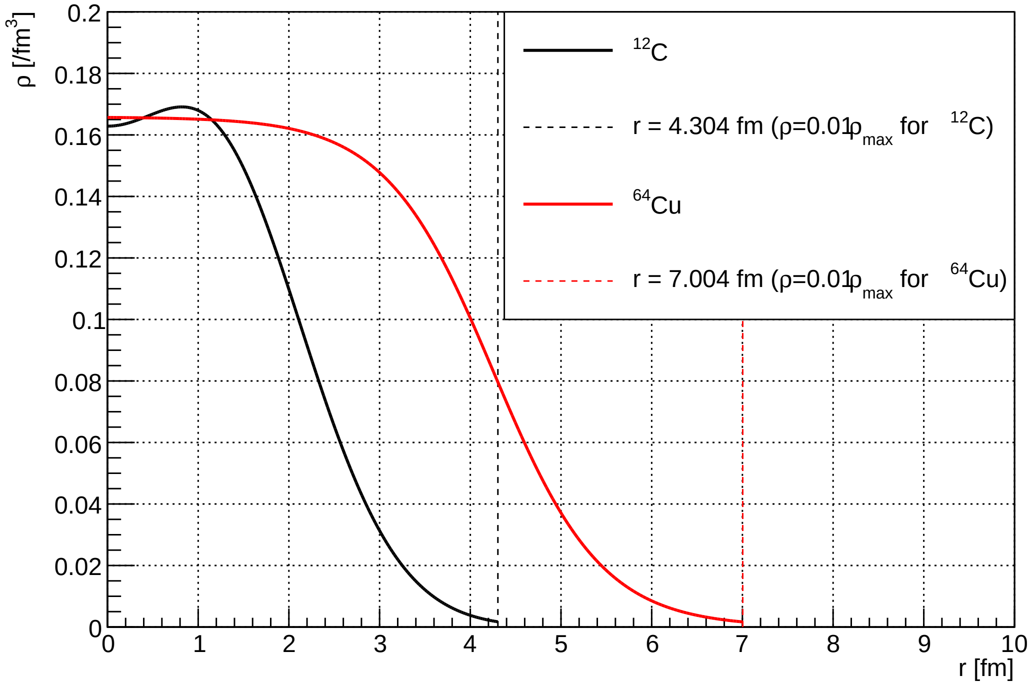

Figure 3.1: Spatial density distribution of ^{12}C and ^{64}Cu. Black (red) lines are about ^{12}C (^{64}Cu). Dashed lines represent the radius at which the density is 1% of the maximum density of the nuclei.

3.3.1 Position

For the target nuclei (C, Cu), nucleons are randomly placed one by one within a sphere whose radius is given by adding 2 fm to the radius calculated with Eq. (3.2), with a probability proportional to the density distribution calculated with Eq. (3.1). If the density at the selected position is less than 1 % of the maximum density, the nucleon is repositioned. In the cases of ^{12}C and ^{64}Cu, the central distances corresponding to this density are 4.304 fm and 7.004 fm, respectively. Additionally, if a nucleon comes within 0.8 fm of another nucleon within the same event during the placement process, it is also repositioned randomly. After the placement is completed, the entire nucleus system within each event is shifted so that the average position of all nucleons in the same event becomes zero.

The projectile proton is randomly placed within a circle on the xy-plane (perpendicular to the beam axis), whose radius is given by adding 2 fm to the target radius calculated with Eq. (3.2). In the present analysis, while the positions of the projectile protons were varied between parallel ensembles, they were fixed within the events belonging to the same parallel ensemble.

3.3.2 Momentum

For the target nuclei (C, Cu), the Fermi momentum for each nucleon is calculated according to its local density obtained by Eq. (3.1) using Eq. (3.3).

$$p_{\mathrm{Fermi}}(\rho) = \hbar c(\frac{3}{2}\pi^2\rho)^{1/3}. \tag{3.3}$$

A random momentum vector with a magnitude less than or equal to the p_{Fermi} is assigned to each nucleon. Then, the total momentum of all nucleons within each event is shifted so that the average momentum becomes zero.

The projectile proton is given a kinetic energy of 12 GeV in the direction of the beam axis.

3.3.3 Lorentz Boost

Both the target and the projectile are Lorentz-boosted into the center-of-mass (CM) frame of the projectile proton and a stationary nucleon. The distance between the projectile proton and the center of the target nucleus in the CM frame is determined by $(2.6A_{\mathrm{tgt}}^{1/3}/\gamma + 3)$ fm to avoid the overlap of nuclei at the beginning of the simulation, where A_{tgt} is the mass number of target nucleus and γ is the Lorentz factor of the system.

3.4 Space and Time Step Sizes

In PHSD, the simulation is performed in a spatial domain defined as $\pm30\Delta x$, $\pm30\Delta y$, $\pm38\Delta z$, where Δx, Δy, and Δz are lattice sizes mainly used for density calculations. The values of Δx and Δy are fixed to 1 fm, while Δz evolves with time to cover an increasingly wider range in the longitudinal direction. At 49 fm/c, which is close to the upper time limit of the current simulation, the fraction of hadrons with $|x| > 30$ fm is only 0.03%, indicating that the spatial volume is sufficiently large.

Initially, Δz is set to $1/\gamma$, where γ is the Lorentz factor, and remains so until a certain time t_z, which satisfies the following condition:

$$(t_z - t_{\text{coli}})\beta + \frac{12}{\gamma} > \frac{i_z}{\gamma}, \tag{3.4}$$

where β is the velocity of the center-of-mass frame, $i_z = 38$ is half the number of lattice cells along the z-axis, and $t_{\text{coli}} = z_0/\beta$ represents the time at which the center of the target nucleus nucleus reaches $z = 0$ simultaneously with the projectile, assuming initial momentum conservation. In this expression, the first term on the left-hand side represents the absolute value of the z-coordinate of the center of the target and projectile nucleus at time t_z fm/c, the second term corresponds to the Lorentz-contracted nuclear radius, assuming a maximum rest-frame radius of 12 fm, and the right-hand side indicates the maximum z-range of the simulation domain after Lorentz contraction (Fig. 3.2). This condition ensures that the simulation volume is expanded only after the colliding nuclei begin to approach the boundaries of the simulation region. After the time t_z, Δz is updated dynamically according to:

$$\Delta z = \frac{(t - t_{\text{coli}})\beta + 12/\gamma}{i_z - 2}, \tag{3.5}$$

where the numerator represents the outermost z-position of a non-interacting target and projectile nucleus with a 12 fm radius, propagating under momentum conservation. The time dependence of Δz is shown in Fig. 3.3.

The time step Δt is determined based on the updated Δz, and is given by $\Delta t = 0.5\Delta z$. The simulation was carried out up to 50 fm/c in the present analysis. However, at the beginning of the simulation, the earliest time at which any target nucleon and any projectile nucleon in any event of the ensemble come within a distance of 1.6 fm is determined. From that time, the system is evolved backward by three time steps, and time evolution proceeds with a step size of one time unit thereafter.

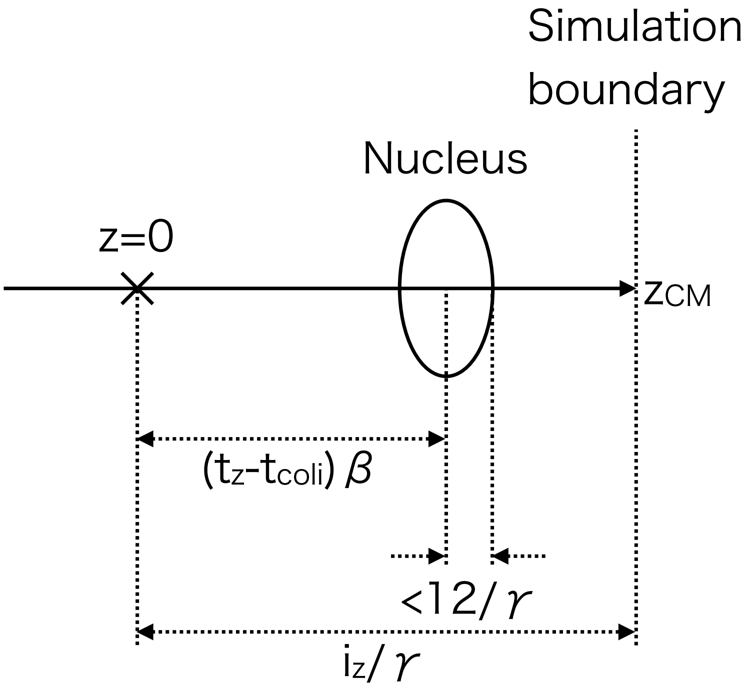

Figure 3.2: Schematic illustration of the concept represented by Eq. (3.4).

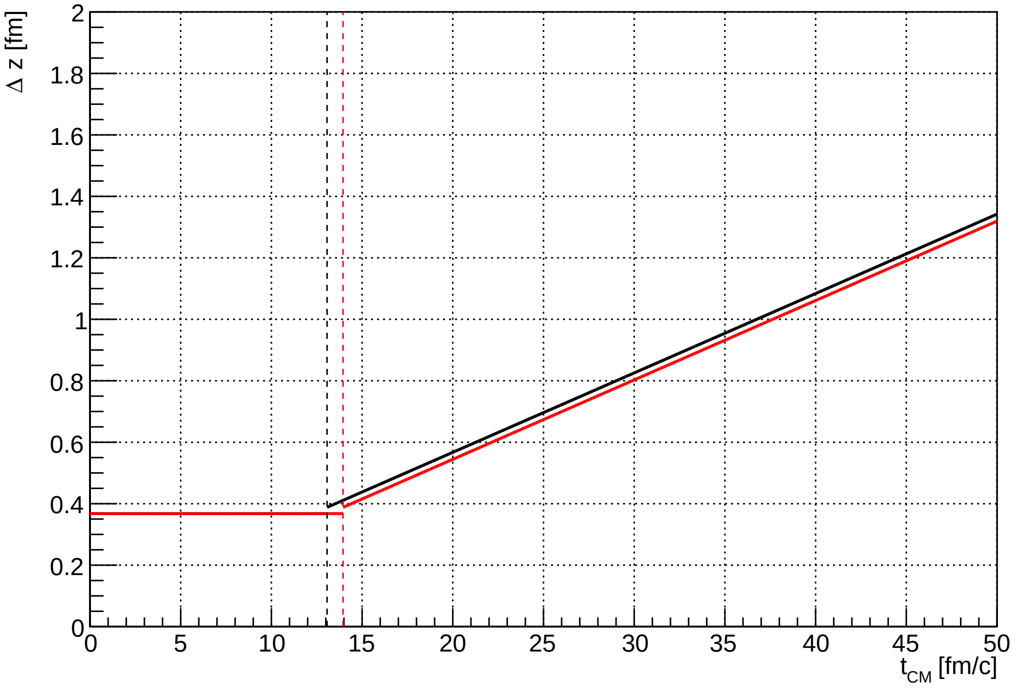

Figure 3.3: Time dependence of Δz for 12 GeV p^{12}C and p^{64}Cu reactions. Black (red) lines are for ^{12}C (^{64}Cu). Dashed lines represent t_z. On the left-hand side of the figure, the black line overlaps with the red line.

3.5 Baryon Density

In PHSD, the baryon density and net baryon density (baryon density with the contribution of antibaryons taken as negative) are evaluated at each time step for each lattice cell using the following expressions:

$$\begin{aligned} \rho'_{\mathrm{B}} &= \frac{(N_B + N_{\bar{B}})\sqrt{1-\bar{\beta}^2}}{N_{\mathrm{TP}}\Delta V}, \\ \rho'_{\mathrm{NB}} &= \frac{(N_B - N_{\bar{B}})\sqrt{1-\bar{\beta}^2}}{N_{\mathrm{TP}}\Delta V}, \end{aligned} \tag{3.6}$$

where N_B and $N_{\bar{B}}$ denote the number of baryons and anti-baryons within the lattice cell, respectively, $\bar{\beta}$ is the average velocity of the baryons in the cell, N_{TP} is the number of test particles, and ΔV is the volume of the lattice cell. The factor $\sqrt{1-\bar{\beta}^2}$ is introduced to evaluate the density in the rest frame of the lattice. To suppress density fluctuations, PHSD takes the average of the above quantities over 27 ($3 \times 3 \times 3$) neighboring cells, including the central cell and those within ± 1 cell along each of the x, y, and z directions. These averaged values are then baryon and net baryon densities.

3.6 Baryon Propagation

In the initial time steps described in Sect. 3.4, the momenta and the x and y positions of all nucleons are kept fixed. During this period, the relative positions of nucleons within the target and projectile nuclei are preserved, and only the z positions evolve according to the collective longitudinal momentum of the respective nuclei. After this time, the propagation is calculated based on the relativistic mean-field theory of the nonlinear Walecka model [36]. Here, the scalar potential corresponds to the effective mass, while the vector potential corresponds to the energy and momentum.

3.6.1 Potentials

At each spatial lattice point, the scalar potential U_s and the time component of the vector potential U_v are given by Eqs. (3.7) and (3.8), respectively:

$$U_s = g_s \sigma, \tag{3.7}$$

$$U_v^0 = g_v \omega^0, \tag{3.8}$$

where g_s and g_v are the scalar and vector coupling constant, respectively. Here, σ denotes the scalar meson field, and ω^0 denotes the time component of the vector meson field. The values of σ and ω^0 are obtained by solving Eqs. (3.9) and (3.10), respectively.

$$m_\sigma^2 \sigma + b\sigma^2 + c\sigma^3 = g_s \rho_s, \tag{3.9}$$

$$m_\omega^2 \omega^0 = g_v \rho_{NB}, \tag{3.10}$$

where m_σ and m_ω are the masses of the σ and ω mesons, b and c are coefficients representing higher-order contributions, ρ_s is the scalar density, and ρ_{NB} is the net baryon density. The values of g_s, g_v, b, and c used in this analysis are those of NL1 listed in Table 1 of Ref. [57]. NL1 is an abbreviation for the nonlinear σ–ω model, which is one of the models used for the parameter calculation in Ref. [57]. These values are determined so as to reproduce the nuclear saturation density and the effective nucleon mass. The scalar density depends on the scalar potential and is calculated using Eq. (3.11)

$$\rho_s = \frac{1}{N_{\mathrm{TP}} \Delta V} \sum \frac{m^*}{E^*}, \tag{3.11}$$

where m^* is the baryon mass modified by the scalar potential, as defined in Eq. (3.12), and E^* is the baryon energy calculated using m^*.

$$m^* = \frac{m_N^*}{m_N} m, \tag{3.12}$$

where m_N is the nucleon mass in vacuum, and $m_N^* = m_N - U_s$ is the nucleon mass modified by the scalar potential. By solving Eq. (3.9) numerically via iteration, U_s can be determined.

3.6.2 Momentum Update

For each baryon, the Hamiltonian at positions shifted by one lattice unit in the x, y, and z directions is calculated using Eq. (3.13).

$$H(\vec{x}) = U_v^0(\vec{x}) + \sqrt{(m + U_s(\vec{x}))^2 + (\vec{p} - \vec{U}_v(\vec{x}))}, \tag{3.13}$$

where $(U_v^0, \vec{U_v})$ denotes the vector potential Lorentz-boosted to the local rest frame of the lattice cell, and m and $\vec{p}$ represent the baryon mass and momentum, respectively. Using this Hamiltonian, each component of the momentum is updated using a finite-difference approximation to $dx/dt = \partial H/\partial p_x$:

$$\begin{aligned}
p_x &\rightarrow p_x + \Delta t \frac{H(x+\Delta x) - H(x-\Delta x)}{2\Delta x}, \\
p_y &\rightarrow p_y + \Delta t \frac{H(y+\Delta y) - H(y-\Delta y)}{2\Delta y}, \\
p_z &\rightarrow p_z + \frac{\Delta t}{\gamma_{CM}} \frac{H(z+\Delta z) - H(z-\Delta z)}{2\Delta z}.
\end{aligned} \tag{3.14}$$

3.6.3 Position Update

To update the position of each baryon, the Hamiltonian is calculated with small variations in momentum using Eq. (3.13), and the positions are updated as follows:

$$\begin{aligned}
x &\rightarrow x + \Delta t \frac{H(p_x+\Delta p_x) - H(p_x-\Delta p_x)}{2\Delta p}, \\
y &\rightarrow y + \Delta t \frac{H(p_y+\Delta p_y) - H(p_y-\Delta p_y)}{2\Delta p}, \\
z &\rightarrow z + \Delta t \beta_z.
\end{aligned} \tag{3.15}$$

The evolution of x and y is approximated by the relation $dp_x/dt = -\partial H/\partial x$. In contrast, for the z-axis, which corresponds to the beam axis and is subject to a strong Lorentz boost, the Hamiltonian has negligible influence. Therefore, a simplified expression is adopted to reduce computational cost. This propagation method explained here is applied when the beam energy is greater than 3 GeV.

3.7 Hadronic Interactions

At each time step, all possible hadron pairs within the same event are considered for reaction simulation. Nucleons that initially belonged to the same target nucleus are not allowed to react with each other unless at least one of them has already undergone a prior reaction.

First, for each hadron pair, the reaction threshold distance is determined based on the hadron spicies and their center-of-mass energy ($\sqrt{s}$). The minimum distance between the two hadrons is then calculated from their positions and momenta. A reaction is considered possible if their momenta are not parallel and the minimum distance is reached within the current time step.

Next, depending on the value of $\sqrt{s}$ of the two hadrons, the reaction is classified as either a string formation (high-energy reaction) or a low-energy reaction. For baryon-baryon interactions, the threshold are as follows: string fragmentation occurs for $\sqrt{s} \geq 2.65\,\mathrm{GeV}$, low-energy reaction dominates for $\sqrt{s} \leq 2.152\,\mathrm{GeV}$, and both processes are considered in the intermediate region. For meson-baryon interactions, the threshold is $2.4\,\mathrm{GeV}$, and for meson-meson interactions, it is $1.3\,\mathrm{GeV}$.

Subsequently, based on the hadron types and the reaction channel, a cross section is assigned, and a Monte Carlo method is used to determine whether an elastic scattering, inelastic scattering, or no reaction occurs.

In string fragmentation, hadronization is performed using PYTHIA 6.4 [58–63], which is based on the Lund string model. For low-energy reactions, baryon-baryon interactions are modeled using the One-Boson Exchange model, meson-baryon interactions, are treated with a resonance model [64], and meson-meson interactions follow the Breit–Wigner resonance scheme. The model parameters are turned to reproduce the available experimental data. For ϕ meson production, LUND model and the experimental data of the following channels are used for parameter decision: $pp \to \phi pp$, $pp \to \phi X$, $\pi^+ n \to \phi p$, and $\pi^+ p \to \phi X$.

3.8 ϕ meson

3.8.1 Production

The following processes are considered as possible production mechanisms of the ϕ meson in PHSD.

- baryon-baryon (BB)-string fragmentation
- meson-baryon (mB)-string fragmentation
- $NN \to \phi NN$
- $K\bar{K} \to \phi$
- $\pi N \to \phi N$
- $K\bar{K} \to \phi m$

- annihilation (for example, $N\bar{N} \to \phi m$, $Y\bar{Y} \to \phi m$)

The difference in various physical quantities of the produced ϕ mesons depending on the type of reaction are discussed in Sect. 4.1. In this thesis, B and m in the reaction channels represent a baryon and a meson, respectively.

3.8.2 Density-Dependent Spectral Modification

In PHSD, the mass of the ϕ meson is calculated from the following relativistic Breit–Wigner distribution.

$$A(m) = \frac{2}{\pi} \frac{m^2 \Gamma_\phi(\rho)}{(m^2 - m_\phi(\rho)^2)^2 + m^2 \Gamma_\phi(\rho)^2}, \tag{3.16}$$

where m_ϕ is the in-medium resonance mass and Γ_ϕ is the in-medium width. The density dependence of the ϕ meson resonance mass and width in PHSD is parameterized as follows:

$$m_\phi(\rho) = \frac{1}{1 + \dfrac{k_1}{1 - k_1} \dfrac{\rho}{\rho_0}} m_0, \tag{3.17}$$

$$\Gamma_\phi(\rho) = (1 + k_2 \frac{\rho}{\rho_0}) \Gamma_0, \tag{3.18}$$

where m_0 is the vacuum mass, ρ is the baryon density, ρ_0 is the normal nuclear density, Γ_0 is the vacuum decay width, and k_1 and k_2 are the shift and broadening parameter, respectively, explained in Sect. 2.2.4. The expression for the resonance mass is a modified version of Eq. (2.2) used in Ref. [28], such that it does not take negative values even at high densities, while it remains almost identical at normal nuclear densities.

3.8.3 Time Evolution

In PHSD, the range from zero to three times normal nuclear density is divided into 50 bins. For each density bin, the mass spectrum and the corresponding cumulative distribution function (CDF), defined by a modified relativistic Breit–Wigner distribution (Eq. (3.16)), are precomputed.

The ϕ meson propagates by updating its position at each time step. If the local density changes, the meson's mass is updated accordingly by conserving

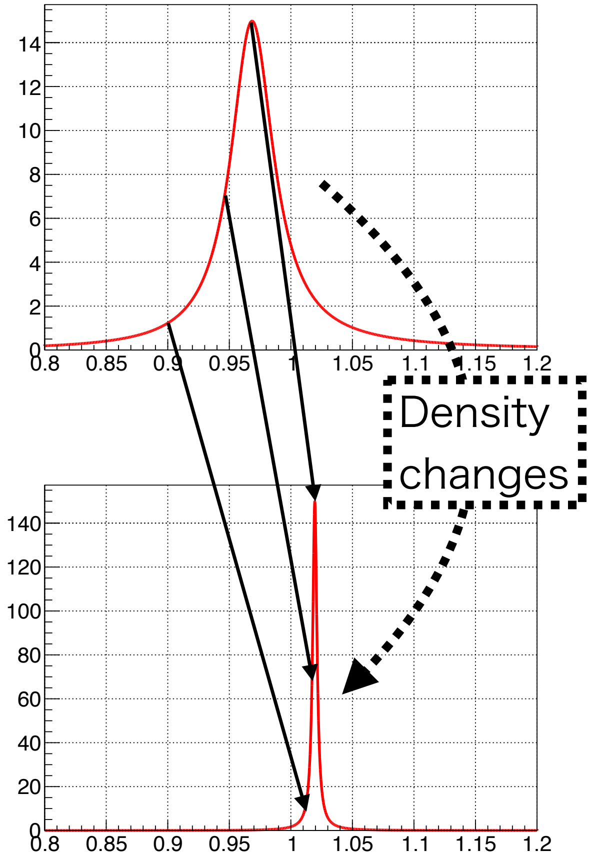

Figure 3.4: Conceptual diagram of mass updating. The upper panel shows the spectrum calculated using the density at the position before time evolution, while the lower panel shows the spectrum calculated using the density at the position after time evolution. The arrows indicate the correspondence between the mass before and after time evolution. Since the update is performed so as to conserve the cumulative probability, masses smaller than the peak remain below the peak, whereas masses larger than the peak remain above the peak after updating.

the cumulative probability on the CDF corresponding to the new density, as shown in Fig. 3.4.

Since the ϕ meson evolves with energy conservation, issues arise if the updated mass exceeds the local energy. The details of this treatment are discussed in Sect. 4.2.2.

In addition, PHSD employs the shining method for simulating the di-electron decay of the ϕ meson. At each time step, the ϕ meson is kept in the system, while a virtual di-electron decay is simulated. The decay probability is calculated from the local density and momentum, and is used as a statistical weight. This method is justified by the extremely small branching ratio of the $\phi \to e^+e^-$ decay and allows for enhanced statistical precision in the analysis of di-electron observables. In PHSD, the weight W considered at each step is calculated using Eq. (3.19):

$$W = \begin{cases} \Gamma_{ee}(m, m_\phi(\rho))\dfrac{\Delta t}{\hbar c\gamma} & \text{if } t < t_F, \\ \dfrac{\Gamma_{ee}(m, m_\phi(\rho))}{\Gamma(\rho)} \exp(-\dfrac{\Gamma(\rho)t_F}{\hbar c\gamma}) & \text{if } t \geq t_F, \end{cases} \tag{3.19}$$

Here, Γ_{ee} is the partial width for $\phi \to e^+e^-$, which is evaluated from vector meson dominance as $\Gamma_{ee} = C_{\phi\to e^+e^-}(m_\phi(\rho)^4/m^3)$. The exponential term in the case of the time upper limit is believed to represent the survival probability up to time t_F; however, this factor should already be accounted for through the absorption and decay processes of the ϕ meson during the PHSD time evolution. In the present analysis, we redefined this weighting scheme ourselves. The details are described in Sect. 4.3.1.

3.8.4 Decay and Absorption

The following processes are considered as possible decay or absorption mechanisms of the ϕ meson in PHSD.

- 3-body interaction
  - $\phi BB \to BB$
- 2-body interaction
  - mB string ($\phi B \to X$)
  - $\phi N \to \pi N$
  - $\phi N \to 2KN, 3\pi N$
  - $\phi N \to N$
- decay

- $\phi \to K^+K^-$
- $\phi \to K^0K^0$
- $\phi \to 3\pi$

Three-body reactions can occur when a ϕ meson and two baryons are located within the same spatial cell and their total center-of-mass energy is below 5 GeV.

In the case of two-body reactions, the procedure described in Sect. 3.7 is first applied to determine whether a reaction can take place. If the center-of-mass energy exceeds 2.4 GeV, string fragmentation is calculated, otherwise, a low-energy reaction is considered. In PHSD, ϕN low-energy reactions are only allowed when the center-of-mass energy satisfies $\sqrt{s} > M_N + 3M_\pi$, where M_N is the nucleon mass and M_π is the pion mass and these values are constant. If the mass of the ϕ meson exceeds the pion mass, processes such as $\phi N \to \pi N$ or $\phi N \to 2KN, 3\pi N$ may occur. Conversely, if the ϕ meson mass falls below the pion mass, the decay $\phi N \to N$ may take place. However, in the present simulation, the latter case hardly occurs.

The probability of each decay channel is calculated taking into account the in-medium mass modification of the kaon and anti-kaon. The in-medium mass of the kaon is calculated using its self energy Π as

$$m^*_{K^+} = \sqrt{m^2_{K^\pm} + \mathrm{Re}(\Pi_{K^+})}, \tag{3.20}$$

$$\mathrm{Re}(\Pi) = 0.05\rho_{\mathrm{NB}} m_{K^\pm}, \tag{3.21}$$

where $m_{K^\pm}$ is the kaon mass in vacuum and ρ_{NB} is the net-baryon density. For anti-kaons, their mass is randomly determined from the spectral function and available phase space, with an upper limit set by the mass difference between the in-medium ϕ meson and the in-medium kaon. The spectral function is given by:

$$A(m) = \frac{1}{\pi}\frac{\mathrm{Im}(\Pi_{K^-})}{(m^2 - m_K^2 - \mathrm{Re}(\Pi_{K^-}))^2 + \mathrm{Im}(\Pi_{K^-})}. \tag{3.22}$$

The in-medium mass of the anti-kaon, unlike that of the kaon, is dominated by its coupling to baryon resonances such as the $\Lambda(1405)$, making the situation more complicated, therefore, we do not go into detail here. The actual PHSD output is presented in Sect. 4.

Chapter 4

Analysis

4.1 Output of PHSD

Table 4.1 summarizes the relative contributions of different ϕ meson production channels in 12 GeV pC and pCu reactions, as calculated with PHSD, along with the initial production cross sections for each channel before absorption. 78% of the ϕ mesons are created via string fragmentation. Table 4.2 shows the ratios of ϕ-meson absorption and decay channels for pCu reaction. The output function for the absorption and decay processes was added in

Table 4.1: Breakdown of ϕ-meson creation channels.

Creation channel	pC		pCu	
	Ratio [%]	σ_{init} [mb]	Ratio [%]	σ_{init} [mb]
BB-string	55	0.15	39	0.50
mB-string	23	0.061	39	0.51
$NN \to \phi NN$	18	0.047	15	0.19
$K\bar{K} \to \phi$	2.3	6.1×10^{-3}	2.7	0.034
$\pi B \to \phi B$	1.8	4.8×10^{-3}	3.6	0.047
$K\bar{K} \to \phi m$	0.094	2.5×10^{-4}	0.17	2.2×10^{-3}
Annihilation	0.025	6.7×10^{-5}	0.030	3.9×10^{-4}
Total	-	0.27	-	1.3

PHSD after large-scale data generation for the main analysis, therefore, the same value for the pC reaction was omitted.

The initial cross section σ_{init} can be calculated using:

$$\sigma_{\text{init}} = \frac{\pi r^2 Y}{N_{\text{TP}}}, \tag{4.1}$$

where Y is the yield, N_{TP} is the number of test particles, and r is the maximum impact parameter used in the simulation. In this context, r must be large enough so that no nucleons of the target nucleus exist beyond this radius, and small enough so that the projectile does not approach multiple target nuclei within r. As shown in Fig. 3.1, there are almost no target nucleons located beyond r, and for the latter condition, there is a margin of several orders of magnitude when assuming a target thickness of approximately several hundred µm. Therefore, the chosen value of r is considered appropriate.

Using the values of the initial cross section and decay ratio listed in Tables 4.1 and 4.2, the measurable production cross section excluding absorption is found to be 0.74 mb for the 12 GeV pCu reaction by the PHSD simulation as shown in Table 4.3. The output function for the absorption and decay processes was not yet implemented in PHSD during large-scale data generation for the main analysis, therefore, the same value for the pC reaction was omitted (Table 4.3).

The distribution of production points along the z-axis (beam axis) in the laboratory frame is shown in Fig. 4.1. $z_{\text{lab}} = 0$ and $t_{\text{lab}} = 0$ are chosen as the reference position and time, corresponding to the situation where the

Table 4.2: Fraction of the various absorption and decay channels of ϕ mesons created in the 12 GeV pCu reaction. Channels with contributions below 0.1% are omitted.

Absorption and decay channel	Ratio [%]
ϕB-string ($\phi B \to X$)	32.9
$\phi \to K^+K^-$	25.9
$\phi \to K^0\bar{K}^0$	17.9
$\phi \to 3\pi$	13.4
$\phi N \to 2K/3\pi N$	9.88

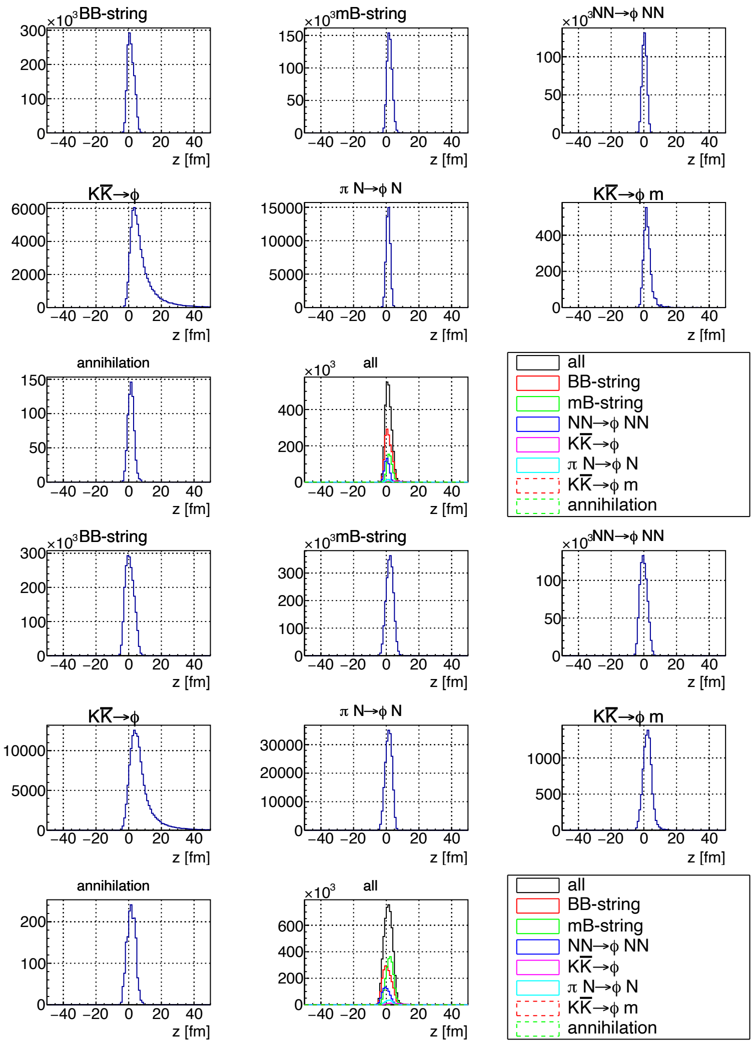

Figure 4.1: Distribution of the z-coordinates of the production points in the lab frame. The upper eight panes show the results for the pC reaction, and the lower eight panes show those for the pCu reaction. The line colors and styles correspond to the production processes as indicated in the legend.

centers of the target nucleus and the projectile coincide without undergoing any interaction. It is evident that ϕ mesons produced via the $K\bar{K} \to \phi$ process are generated farther downstream relative to the initial position of the target nucleus compared to other channels. The ϕ mesons produced via $K\bar{K}$ channels, particularly $K\bar{K} \to \phi$, are preferentially generated in the forward direction along the z axis relative to those originating from other processes. This is likely because this process does not require baryons, unlike the other production mechanisms. The difference between $K\bar{K} \to \phi$ and $K\bar{K} \to \phi m$ is attributed to the fact that the former is calculated in a density-independent manner, whereas the latter accounts for the self-energies of kaon and anti-kaon, which depend on local density and other factors. However, as these channels represent only a small fraction of the total ϕ-meson production, we do not discuss them in further detail.

Figure 4.2 shows the distribution of the radial distance from the center of the target nucleus to the production points in the laboratory frame for each production channel. This is compared with the case where the production is assumed to occur in proportion to the Woods–Saxon distribution, as shown in Fig. 4.3. Figure 4.3 presents the distribution of the distance from the target center for all processes combined, fitted with a function given by the Woods–Saxon distribution multiplied by the surface area, which was employed in Ref. [28]. For both pC and pCu reactions, it is found that ϕ mesons are more likely to be produced outside the distribution predicted by the static density profile, and that the deviation is larger for pCu. This suggests that many of the ϕ mesons are produced in secondary or later collisions. The difference of the parameters in Eq. 2.5 are shown in Table 4.4. Table 4.4 presents a comparison between the Woods–Saxon distribution parameters obtained from the fit in Fig. 4.3 and those used in Ref. [44] due to obtaining positions of ϕ meson generation.

Table 4.3: Production cross section of ϕ mesons in 12 GeV pA reactions, as obtained from experiment and transport calculations.

Experiment/Calculation	σ_{pC} [mb]	σ_{pCu} [mb]
KEK-PS E325	0.33	1.56
JAM	0.30	2.21
Present analysis (based on PHSD)	-	0.74

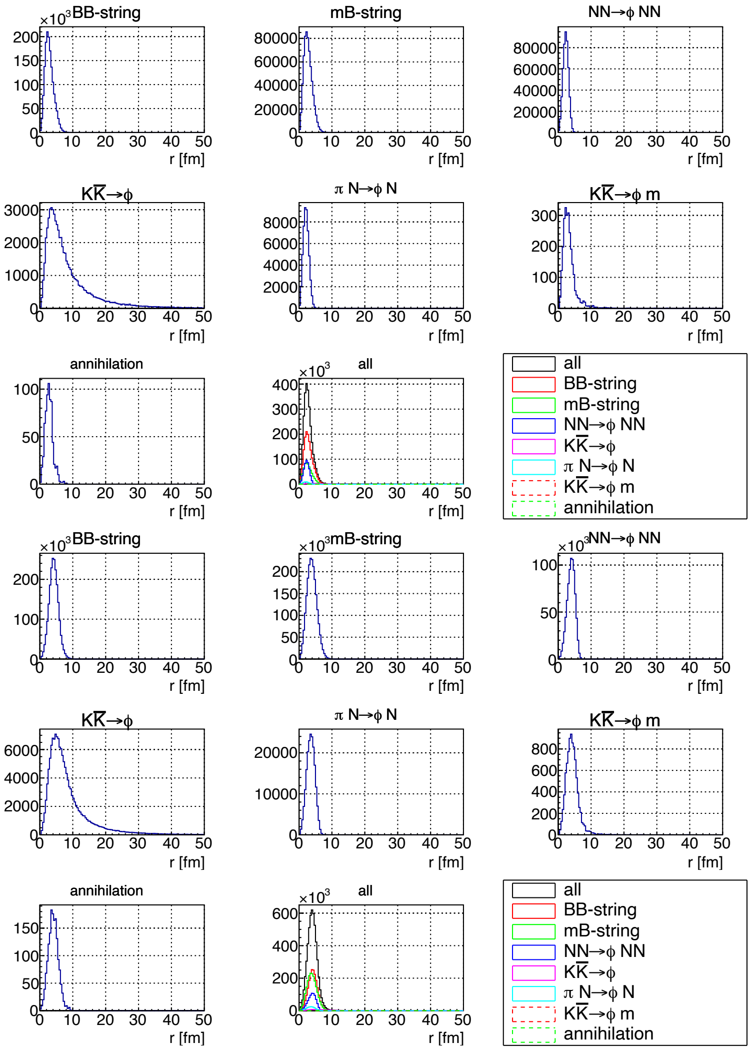

Figure 4.2: Radial distance of ϕ-meson production points from the center of the target nucleus for each production channel. The upper eight panes show the results for the pC reaction, and the lower eight panes show those for the pCu reaction. The line colors and styles correspond to the production processes as indicated in the legend.

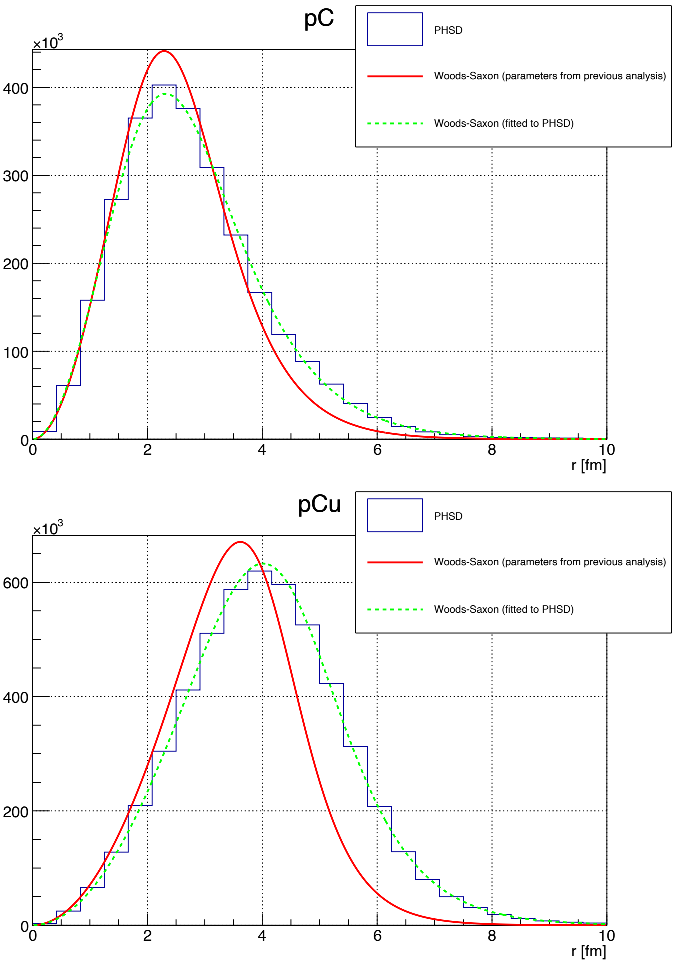

Figure 4.3: Distribution of the distance of the ϕ-meson production points from the target center, together with the fit based on the Woods–Saxon distribution. Red lines represent the fitted function, with only the scale being a free parameter. Green dashed lines represent the fitted function, with the R, τ in Eq. 2.5, and scale being free parameters. The upper panel shows the results for the pC reaction, and the lower panel shows those for the pCu reaction.

The distribution of production times is presented in Fig. 4.4. Here, $t = 0$ corresponds to the time at which the centers of the projectile proton and the target nucleus would overlap if no interaction occurred. As expected from

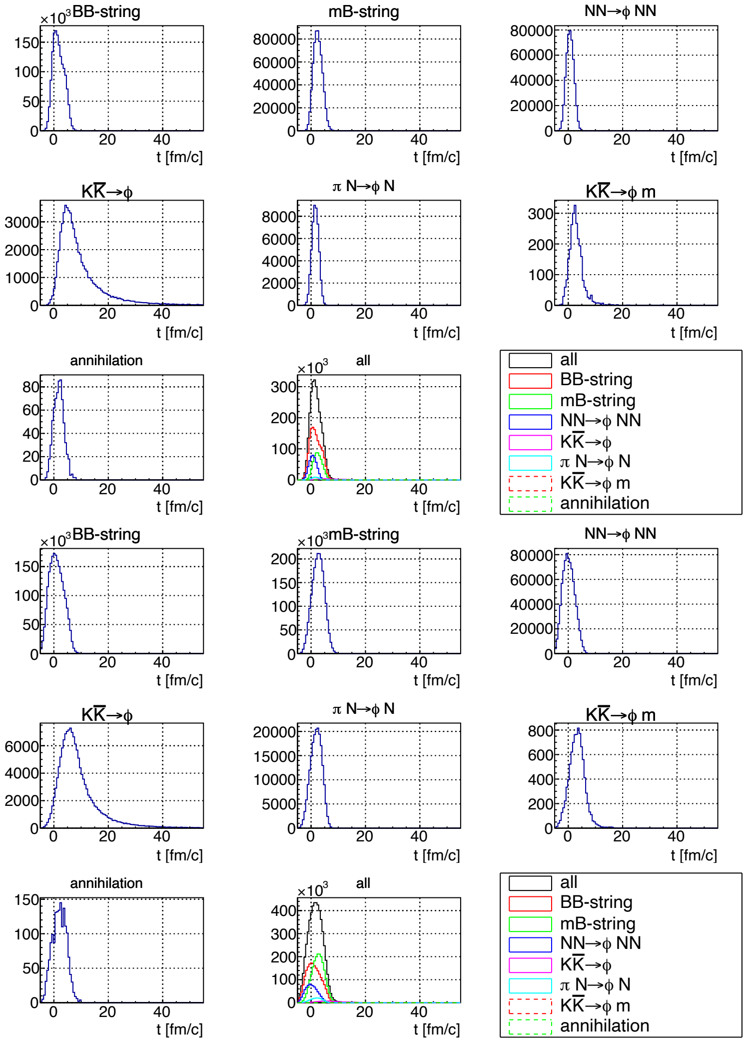

Figure 4.4: Distribution of ϕ-meson production times in the laboratory frame. The upper eight panes show the results for the pC reaction, and the lower eight panes show those for the pCu reaction. The line colors and styles correspond to the production processes as indicated in the legend.

Figs. 4.1 and 4.2, ϕ mesons produced through $K\bar{K} \to \phi$ are more frequently generated at later times compared to other channels.

The distribution of baryon densities at the ϕ-meson production points is shown in Fig. 4.5. As suggested in Fig. 4.2, ϕ-meson production via $K\bar{K}$ occurs predominantly in low-density regions.

The mass spectra at the production time are shown in Figs. 4.6 and 4.7. The mass ranges of Fig. 4.6 and Fig. 4.7 are $0\,\mathrm{GeV}/c^2$ to $2\,\mathrm{GeV}/c^2$ and $0.9\,\mathrm{GeV}/c^2$ to $1.1\,\mathrm{GeV}/c^2$, respectively. The lower-mass threshold for $K\bar{K} \to \phi$ is, in reality, determined by the sum of the in-medium masses of the kaon and anti-kaon. However, in PHSD it is fixed at twice the vacuum kaon mass, independent of the density. The increase in yield toward the lower limit is considered to be dominated not by the Breit–Wigner effect, but rather by the change in the upper mass limit allowed by the momentum. The flat components observed in $NN \to \phi NN$ and $\pi N \to \phi N$, as well as the peak around $0.4\,\mathrm{GeV}$ and the narrow peak of $K\bar{K} \to \phi m$, are due to specific implementations in PHSD, which will be discussed in detail in Sect. 4.2.2.

The momentum distributions at production are presented in Fig. 4.8. The comparison with the experimental data is discussed in Sect. 4.3.7.

Table 4.4: Comparison of the Woods–Saxon distribution parameters obtained from the fit of generation position in Fig. 4.3 with those used in Ref. [44].

	C		Cu	
	R [fm]	τ [fm]	R [fm]	τ [fm]
Ref. [44]	2.3	0.57	4.1	0.5
Present analysis	2.0	0.71	4.5	0.69

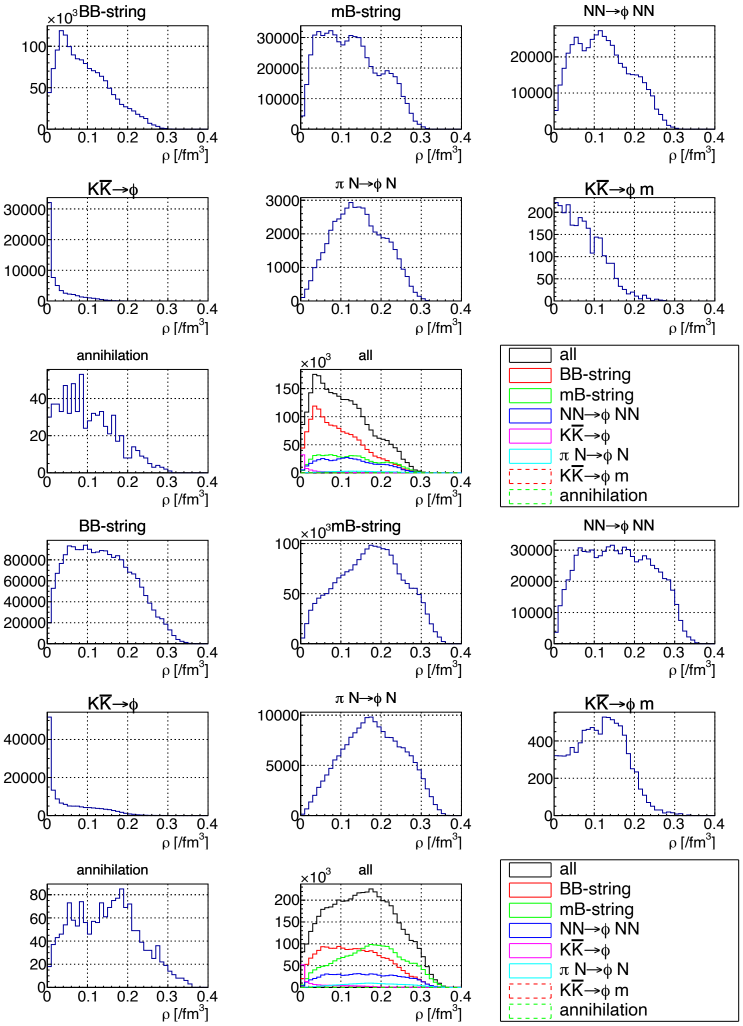

Figure 4.5: Distribution of baryon density at the ϕ-meson production points. The upper eight panes show the results for the pC reaction, and the lower eight panes show those for the pCu reaction. The line colors and styles correspond to the production processes as indicated in the legend.

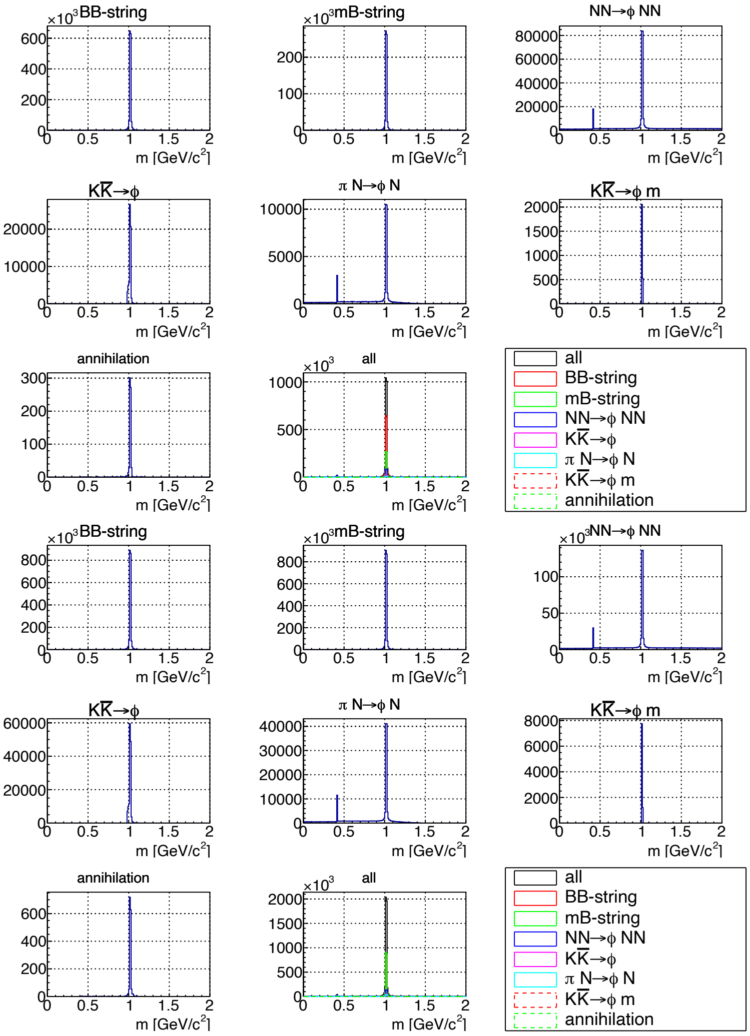

Figure 4.6: Mass spectra of ϕ mesons at the time of production ($0\,\mathrm{GeV}/c^2$ to $2\,\mathrm{GeV}/c^2$). The upper eight panes show the results for the pC reaction, and the lower eight panes show those for the pCu reaction. The line colors and styles correspond to the production processes as indicated in the legend.

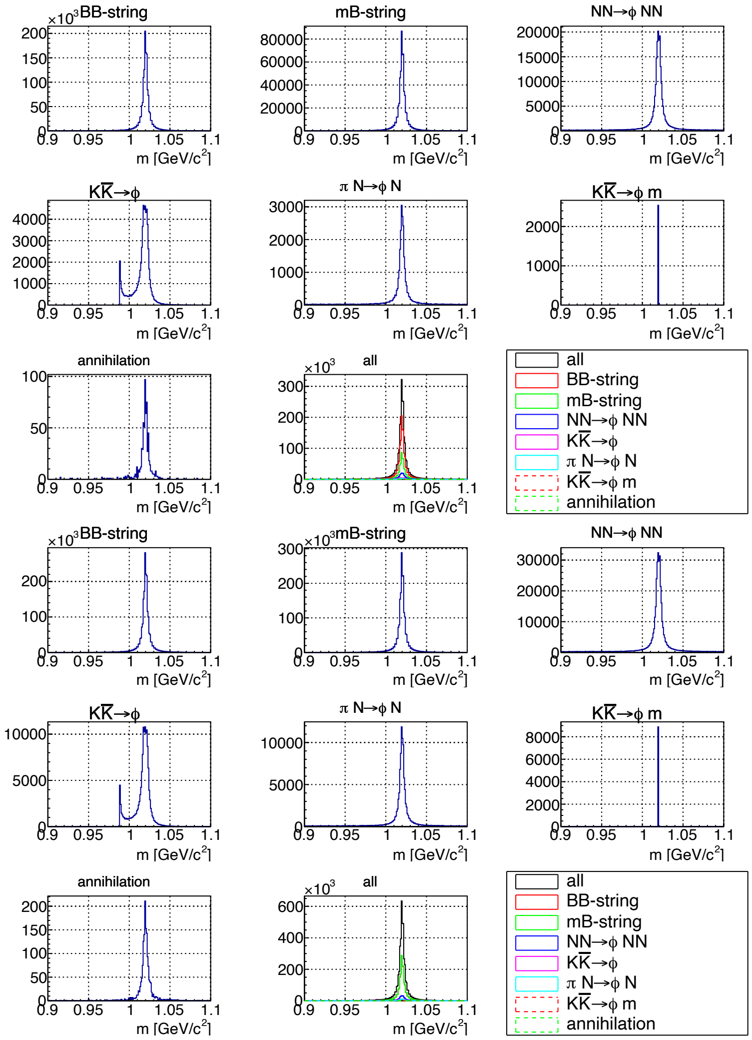

Figure 4.7: Mass spectra of ϕ mesons at the time of production ($0.9\,\mathrm{GeV}/c^2$ to $1.1\,\mathrm{GeV}/c^2$). The upper eight panes show the results for the pC reaction, and the lower eight panes show those for the pCu reaction. The line colors and styles correspond to the production processes as indicated in the legend.

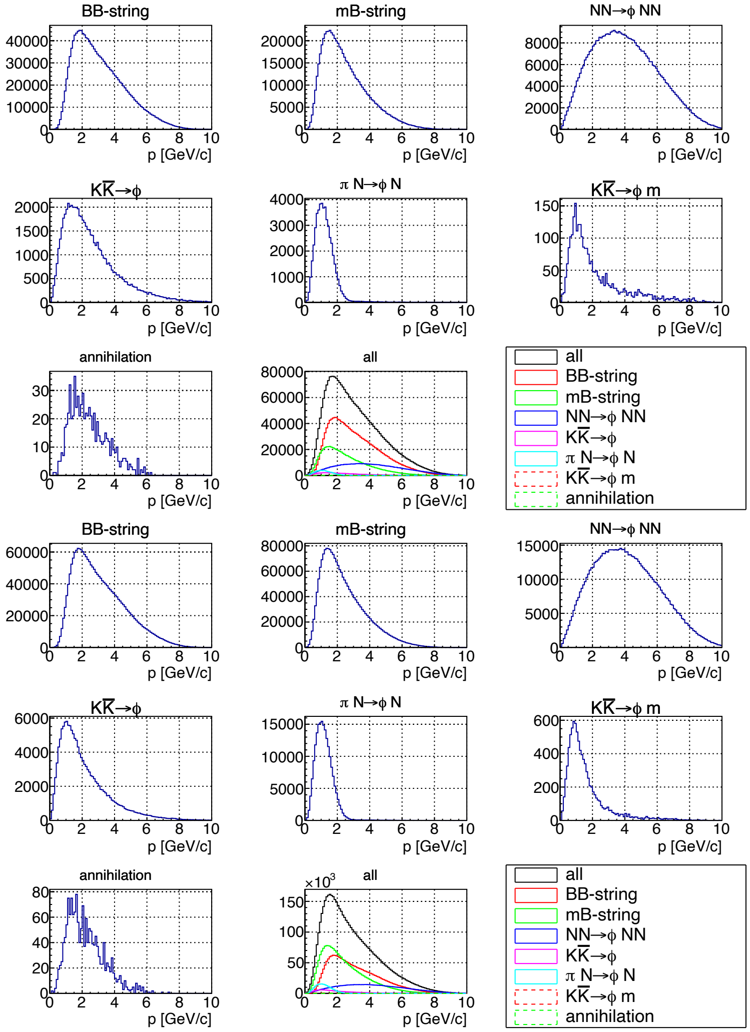

Figure 4.8: Distribution of momentum of ϕ meson at production. The upper eight panes show the results for the pC reaction, and the lower eight panes show those for the pCu reaction. The line colors and styles correspond to the production processes as indicated in the legend.

4.2 Issues in PHSD and Countermeasures

As described in Sect. 3.8.2, PHSD allows users to manually set the shift and broadening parameters that characterize the in-medium modification of the ϕ meson mass spectrum. In principle, these parameters can be determined by performing PHSD simulations with various input values, generating mass, momentum, and decay probability data, applying experimental effects, and fitting the results to experimental data. However, this approach poses several problems as outlined below.

4.2.1 Relation between Width and Lifetime

As mentioned earlier, the broadening parameter can be provided as an input to PHSD. This parameter is used in calculating the spectral width of the ϕ meson mass, but it does not directly affect the meson's lifetime. Since PHSD includes reaction channels in which the ϕ meson disappears due to interactions with other hadrons, the lifetime of the ϕ meson exhibits some density dependence. However, this dependence is not directly linked to the input broadening parameter. Consequently, even when a large broadening parameter is specified as an input to PHSD, the resulting ϕ meson lifetime remains nearly unchanged. As a result, when using PHSD outputs without modification, the in-medium decay fraction of ϕ mesons becomes effectively independent of the broadening parameter.

This behavior significantly affects any discussion of in-medium spectral modifications. Therefore, in the present analysis, we incorporated the influence of the broadening parameter on the lifetime by recalculating the decay probability at each time step using the local density, time step, Lorentz factor γ, and broadening parameter. The accumulated decay probability was then applied as a weight to each time step.

It is necessary to account for the intrinsic density dependence of the ϕ meson lifetime in PHSD, as mentioned earlier. The details of this procedure are described in Sect. 4.3.1.

4.2.2 Treatment of Unphysical Mass Increase beyond CM Energy

As mentioned in Sect. 3.8.2, there is an implementation issue in PHSD regarding the in-medium mass modification of ϕ mesons in response to changes in baryon density. If the updated mass calculated at a new density exceeds the total energy of the ϕ meson, PHSD attempts to resolve this by reducing the displacement per time step, first to half, then to a quarter of its original value, so that the ϕ meson moves to a neighboring spatial cell with potentially different baryon density. If the recalculated mass at the new position becomes physically allowed, i.e., below the energy, the simulation proceeds with updated values.

However, if the baryon density of the original cell changes, resulting in a mass exceeding the energy even at zero displacement, this method fails. In such cases, PHSD then reduces the change in density itself, again to half, then a quarter, until a mass lower than the energy is obtained, after which the momentum is recalculated.

This procedure can cause unphysical situations where ϕ mesons are assigned modified masses even in low-density regions. Moreover, this issue predominantly affects ϕ mesons with small momenta, as their energy margins are limited.

Figure 4.9 shows the CM-frame momentum distribution of ϕ mesons obtained from PHSD integrated over each time step. For the shift and broadening parameters input to PHSD, we used $k_1 = 0.034$ and $k_2 = 2.6$, as obtained in Ref. [28]. A narrow, unnatural peak can be seen around $0.1\,\mathrm{GeV}/c$ to $0.2\,\mathrm{GeV}/c$. This unphysical structure arises from ϕ mesons whose momenta were no longer updated due to the bugs discussed above.

Figure 4.10 shows the simulated mass spectra of ϕ mesons with $\beta\gamma > 2.5$, separated into those with CM momenta above and below $0.2\,\mathrm{GeV}/c$. Due to this bug, a mass shift occurs in the high $\beta\gamma$ region, where mass modification is originally expected to be negligible. Since $\beta\gamma \sim 2.5$ falls within the experimental acceptance, it is not possible to simply exclude this $\beta\gamma$ region when applying the results to experiments.

Furthermore, as discussed in Sect. 4.1, the initial mass assignment of ϕ mesons in PHSD also involves some complications. For example, in the $K\bar{K} \to \phi m$ process, the spectrum is unnaturally narrow because the mass is fixed during generation. Minor broadening arises from the fact that PHSD does not store meson masses directly but instead calculates them from energy and momentum.

For the $NN \to \phi NN$ and $\pi N \to \phi N$ processes, the mass of the ϕ meson is determined as follows. First, a mass is randomly chosen in the range from $0\,\mathrm{GeV/c^2}$ to $2\,\mathrm{GeV}/c^2$ (trial mass). Then, using the trial mass and the CM energy, the probability of producing a ϕ meson with that mass is calculated.

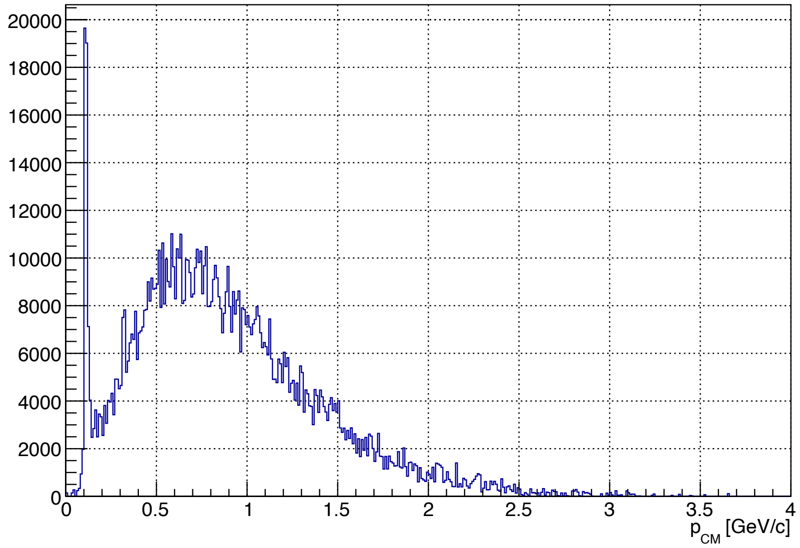

Figure 4.9: CM-frame momentum distribution of ϕ mesons obtained from PHSD. The momentum over all time steps is filled, without any weighting applied.

If a random number generated between 0 and 1 falls below this probability, the mass is accepted, otherwise, the trial mass selection is repeated until the condition is satisfied. If the trial fails, the process is repeated up to a predefined maximum number of iterations. If no mass is accepted by that point, the final trial mass is used. Flat components in the resulting spectra stem from this truncation. In the $\pi N \to \phi N$ case, the upper edge of this flat component is limited to around $1.45\,\mathrm{GeV}$ by the upper limit of CM energy allowed for low-energy interactions.

Lastly, the appearance of a peak near $3M_\pi$, where M_π is the pion mass in the vacuum, is due to the implementation of the Breit–Wigner cumulative distribution, which is only defined above that threshold. Therefore, transitions between density-dependent Breit–Wigner distributions are bounded from below at $3M_\pi$.

To address these issues, the present analysis does not use the mass values output by PHSD directly. Instead, the ϕ meson mass is recalculated after the PHSD simulation using the local baryon density. This procedure removes

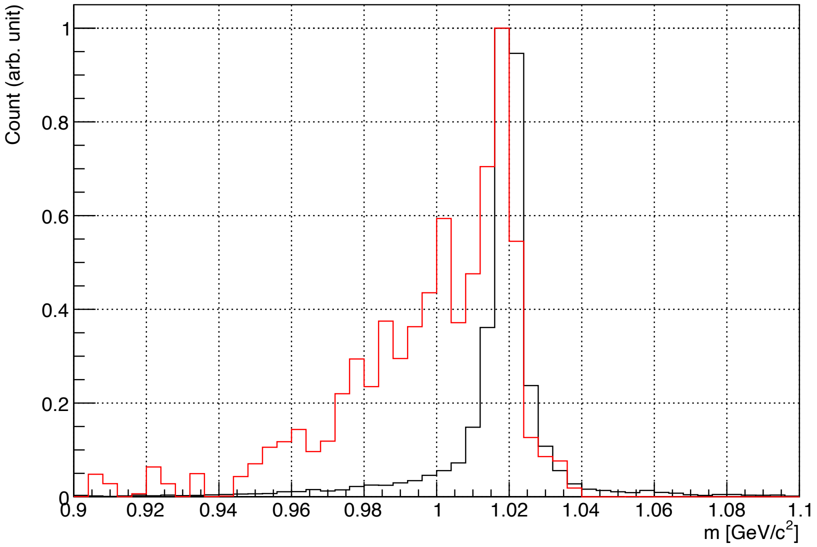

Figure 4.10: Mass distribution of ϕ mesons with $\beta\gamma > 2.5$. Black line represents those with CM-frame momentum above 0.2 GeV/c, while red line corresponds to the rest. The counts are scaled so that the maximum value becomes 1, and no weighting is applied.

the correlation between the momentum and the mass of the ϕ meson, in the sense of where it lies within the Breit–Wigner distribution. Here, the term "mass" refers to the position of the ϕ meson on the Breit–Wigner distribution. As an extreme example, if the ϕ meson is produced at a fixed energy, its momentum and mass are completely correlated. However, since the natural width of the ϕ meson is small, the impact on the momentum is expected to be negligible. Moreover, because the dominant production mechanism is string fragmentation, a high-energy process, the effect of the correlation between mass and momentum begin lost is small, since it occurs well above the kinematic threshold.

4.2.3 Required Statistics

The present analysis was performed using the KEK Central Computing System (KEKCC) [65]. The CPU used was an AMD EPYC 9654 96-Core Processor. Table 4.5 summarizes the CPU time required per ensemble and per generated ϕ meson under this environment.

At KEKCC, batch jobs can be submitted via IBM's Platform Load Sharing Facility (LSF). Depending on the system load, up to 1,200 parallel jobs can be executed per user.

To estimate the number of events required for this analysis, the following procedure was employed:

1. A mass spectrum suitable for comparison with experimental data (specifically, Cu and $\beta\gamma < 1.25$) was generated by applying experimental effects, explained in Sect. 4.3, to the PHSD output produced with a given set of shift and broadening parameters.
2. The corresponding decay probability distribution was also generated.
3. Multiple empty histograms (five in this estimate) were prepared.
4. Values of mass and decay probability were randomly sampled from the distributions in Steps 1 and 2, and filled into the histograms to create mass spectra.
5. After a certain number of iterations of Step 4, each histogram (with a quadratic background added) was fitted to the experimental spectrum. The resulting χ^2 values were compared each other to determine how many iterations were required for convergence.

When weights are assigned to each data point, the statistical uncertainty becomes larger than in the unweighted case, requiring a larger number of events.

Figure 4.11 shows the relation between the number of iterations and the range of χ^2 values (i.e., the difference between maximum and minimum) across the five histograms. For instance, achieving $\Delta\chi^2 < 0.2$ requires approximately five million events.

Table 4.5: CPU time required per ensemble and per created ϕ meson. The computational environment is described in the main text.

Reaction	Time per ensemble [sec]	Time per ϕ meson [sec]
pC	1.7×10^2	7.2×10^2
pCu	1.6×10^2	1.6×10^2

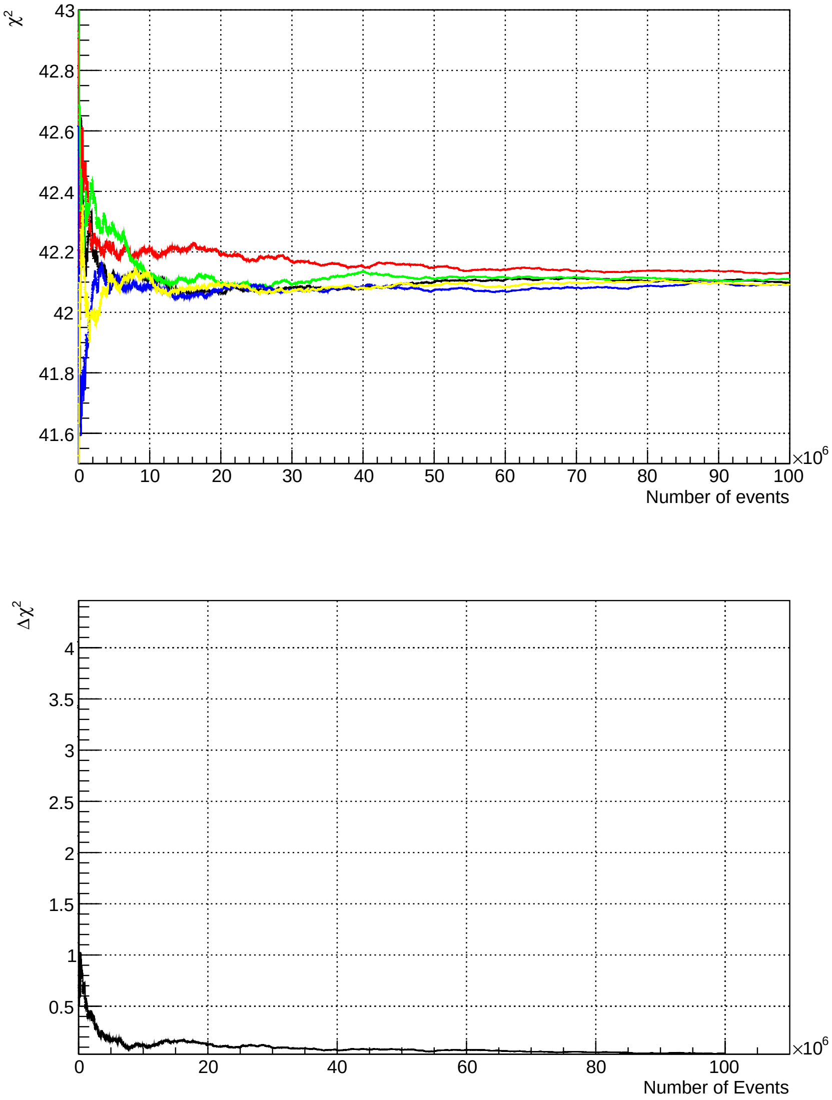

Figure 4.11: Dependence of χ^2 for each histogram, and the difference between the maximum and minimum χ^2 values, on the number of iterations. In the upper panel, each color represents the χ^2 of each histogram. The lower eight panes show the difference between the maximum and minimum χ^2 values.

Because PHSD employs the shining method for the di-electron decay of the ϕ meson, multiple data points can be obtained from a single ϕ meson event. However, if there is no change in local density or interaction with other hadrons, the mass and momentum of the ϕ meson remain constant throughout its evolution. The average number of steps per ϕ meson is 47 for pC and 63 for pCu. However, this estimate is likely an overestimation, since the ϕ meson mass does not change unless the baryon density varies beyond a certain threshold, and its momentum remains unchanged unless there is a mass change or interaction with other hadrons. Consequently, the actual number of effective steps contributing to the relevant observables is smaller, and the computational time required to achieve the necessary statistics increases accordingly.

Taking into account the spectrometer acceptance, the fraction of detected $\phi \to e^+e^-$ decays is 1.5%. However, among the undetected ϕ mesons, some can be detected if their kinematics are rotated around the beam axis. Assuming that the spectrometer covers ± 0.7 rad on each side and that e^+ and e^- are emitted back-to-back in the xy plane, the above fraction is estimated to increase by a factor of about $\pi/0.7 \sim 5$, depending on the way of rotation.

Additionally, the experimental data to be fitted are divided into six categories based on the target nuclei and the $\beta\gamma$ of ϕ meson in Ref. [28]. To perform a similar division in the simulation, the simulation data must also be divided into six subsets, and the subset with the smallest statistics must still exceed the required event count. From Table 2 of Ref. [28], the ratios of the number of ϕ mesons in the lowest-statistics $\beta\gamma$ region to those in the total $\beta\gamma$ region are found to be 14% for pC and 19% for pCu.

Taking all of these factors into account, the estimated time required to obtain sufficient statistics for scanning a single parameter point, i.e., one pair of shift and broadening parameters, with LSF is 8×10 days. Performing such a scan across multiple parameter sets is therefore impractical with this method.

To address these issues, two countermeasures were implemented. The first measure was to set the shift and broadening parameters in PHSD to zero. This approach eliminates the in-medium mass modification within PHSD, thereby avoiding the bug described in Sect. 4.2.2. The mass is randomly determined using a Breit–Wigner distribution constructed from the baryon density output by PHSD together with the simulated shift and broadening parameters. It also removes the need to rerun PHSD multiple times with different combinations of shift and broadening parameters. Furthermore, as discussed in Sect. 4.2.1, the lifetime of the ϕ meson in PHSD is independent of the input broadening parameter, meaning that no information is lost by setting the broadening parameter to zero. This procedure, however, breaks the correlation between momentum and mass (in terms of the position within the Breit–Wigner distribution rather than in-medium modification). Nevertheless, because the natural width of the ϕ meson is small, the influence of mass variations on momentum is expected to be negligible. Moreover, since the dominant production mechanism of ϕ mesons is string fragmentation, a high-energy process that occurs far from threshold energies where mass effects are significant, the impact is expected to be even smaller.

The second measure was to use PHSD not as a direct provider of final observables, but as a generator that outputs correlated sets of longitudinal momentum, transverse momentum, and baryon density. In practice, the transverse/longitudinal momentum and density information output by PHSD at each time step is weighted by the decay probability to generate a three-dimensional distribution. From this distribution, a combination of longitudinal momentum, transverse momentum, and density is randomly sampled, and this set is treated as a single ϕ meson for subsequent processing. This makes the statistical weights of individual ϕ-meson data uniform, simplifies the analysis and the estimation of required statistics, and ensures that the statistics obtained after PHSD are no longer limited by the statistics of PHSD itself.

4.2.4 Instability of Nucleons in Target Nucleus

It is generally difficult in transport calculations to maintain the spatial distribution of nucleons within a nucleus using physically realistic bounds [66]. To investigate this effect in PHSD, we examined the behavior of the target nucleus in 12 GeV pA collisions by analyzing events in which no interaction occurred between the projectile and the target.

For both pC and pCu reactions, we evaluated the spatial distribution of nucleons in the target nucleus using the following procedure:

- At each time step, the transverse radius distribution of nucleons belonging to the target nucleus was constructed. Since the transverse plane is invariant under Lorentz boosts between the CM and lab frames, relativistic effects can be neglected.

- Assuming a Woods–Saxon distribution (Eq. (2.5)), the number of nucleons at each transverse radius was calculated and fitted using the parameters N, R, τ.

The results are shown in Fig. 4.12. This effect was treated as a source of systematic uncertainty, and the evaluation method is described in Sect. 5.

As described in Sect. 3.6, the mean field is calculated from all events in the ensemble. Therefore, ideally, the above analysis should be performed using only those events in which no interaction occurred between the target and the projectile within the ensemble. However, constructing such an ensemble is not practical, and instead, events without any reactions were used. Compared to the case where no reactions occur in any of the events, the present situation weakens the mean field, and thus the evaluation of the uncertainty is conservative.

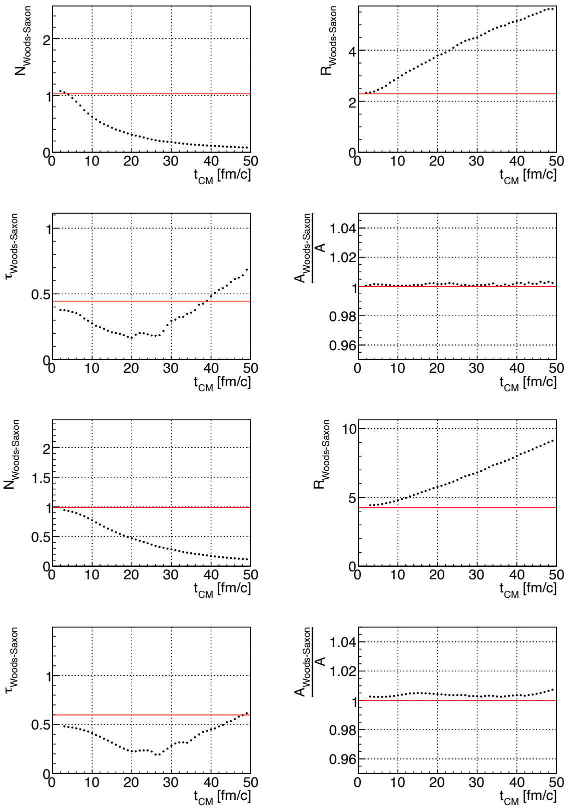

Figure 4.12: Results of fitting the nucleon distributions in the target nucleus at each time step in PHSD with the Woods–Saxon distribution (Eq. (2.5)). The upper four panes correspond to the ^{12}C target, and the lower four panes to the ^{64}Cu target. The top-left, top-right, and bottom-left panels show N, R, and τ of Eq. (2.5), respectively, while the bottom-right panel shows the ratio of the nucleon number calculated from these parameters to the original nucleon number. For the carbon target, PHSD employs the shell model for initialization, however, since the model contains only a small number of parameters and cannot describe the time evolution well, the Woods–Saxon distribution was used for the evaluation. Red lines represent the parameters used for initialization in PHSD. Red line values of R and τ for the carbon target were obtained by fitting the initial distribution in Fig. 3.1 with the Woods–Saxon distribution. Red line values of N for each target were determined such that the number of nucleons calculated with the obtained R and τ agrees with that of the corresponding nucleus, using $A = \int_0^\infty 4\pi r^2 \rho(r) dr \simeq (4\pi/3) N \rho_0 (R^3 + \pi^2 \tau^2 R)$.

4.3 Present Analysis

The objective of the present analysis is to incorporate the effects of hadron transport in 12 GeV pA reactions and quantitatively determine the in-medium spectral modification of the ϕ meson from the spectra measured in the KEK-PS E325 experiment. The spectral modification is modeled as changes in the resonance mass and width within a Breit–Wigner distribution. The density dependence of the resonance mass and width is parameterized by the shift parameter k_1 and the broadening parameter k_2, as expressed in Eqs. (2.2) and (2.3).

The parameter k_2, which represents the density dependence of the lifetime, can in principle be obtained directly from the PHSD results, as discussed later. However, in order to account for possible processes not included in PHSD and to minimize model dependence, k_2 was treated as a free parameter in this analysis.

For the partial width of the e^+e^- decay, it would ideally be parameterized with a separate k_2^{ee} in the same manner as the total width. Due to limited experimental statistics, however, only two extreme cases were considered in this study:

1. a case where the partial width has the same density dependence as the total width, as expressed in Eq. (2.4)

2. The partial width is independent of the density.

Although the partial width, unlike the total width, does not directly modify the spectral shape, it indirectly affects the spectrum by altering the distribution of baryon densities at the time of decay.

In this analysis, the division of the spectra follows the same procedure as in Ref. [28]. The e^+e^- invariant-mass spectra obtained from pC and pCu reactions were categorized into three $\beta\gamma$ regions, slow ($\beta\gamma < 1.25$), middle ($1.25 \leq \beta\gamma < 1.75$), and fast ($\beta\gamma \geq 1.75$), yielding a total of six spectra. For the two scenarios of the partial width, ϕ-meson spectra were simulated for various combinations of k_1 and k_2, which were fitted to the experimental data to determine the best-fit parameters.

The background events were determined by fitting the region outside the ϕ-meson signal window ($0.95\,\mathrm{GeV}/c^2$ to $1.05\,\mathrm{GeV}/c^2$) within the fitting range using an exponential function, $A\exp(-B(m-C))$. The values of the background parameters are fixed regardless of the shift and broadening parameters. The uncertainties arising from the choice of this functional form and the definition of the signal region are discussed in Sect. 5.2.3.

4.3.1 ϕ-Meson Sample Generation

As described above, in this analysis we did not directly use the ϕ meson output from PHSD. Instead, we first constructed the correlated distributions of baryon density, longitudinal momentum, and transverse momentum. To avoid the bug related to the time evolution of the mass, the shift and broadening parameters input to PHSD were set to zero.

When building these distributions, two types of weights were applied to each data point. The first weight is based on the decay probability into an e^+e^- pair, which is expressed using the baryon density ρ, the time-step width Δt, and the Lorentz factor γ of the ϕ meson as:

$$w^{\phi\to e^+e^-}(\rho,\gamma,\Delta t) = 1 - \exp(-\frac{\Gamma_\phi^{ee}(\rho)\Delta t}{\hbar\gamma}), \tag{4.2}$$

where $\Gamma_\phi^{ee}(\rho)$ is given by Eq. (2.4) for the density-dependent partial-width scenario, while for the constant-width scenario, the vacuum partial width of $\phi \to e^+e^-$ is used.

The second weight accounts for the true survival probability of the ϕ meson at a given time step, derived from the difference between the intrinsic broadening parameter of PHSD and the broadening parameter used in this analysis, and is expressed as

$$\begin{aligned} w^{\text{corr.}}(\rho,\gamma,\Delta t) &= \prod \frac{p^{\text{decay}}(\rho,\gamma,\Delta t)}{p^{\text{decay,PHSD}}(\rho,\gamma,\Delta t,)} \\ &= \prod \exp(\frac{(\Gamma_\phi^{\text{PHSD}}(\rho) - \Gamma_\phi(\rho))\Delta t}{\hbar\gamma}) \\ &= \prod \exp(\frac{(k_2^{\text{PHSD}} - k_2)\frac{\rho}{\rho_0}\Gamma_0\Delta t}{\hbar\gamma}), \end{aligned} \tag{4.3}$$

Here, p^{decay} and $p^{\text{decay,PHSD}}$ represent the decay probabilities of the ϕ meson for a given density, Lorentz factor, and time step, corresponding to the desired k_2 and the k_2^{PHSD}, respectively.

Here, the density dependence of the width obtained from the lifetime of ϕ mesons in PHSD is parameterized as:

$$\Gamma_{\phi}^{\mathrm{PHSD}}(\rho) = (1 + k_2^{\mathrm{PHSD}} \frac{\rho}{\rho_0})\Gamma_0. \tag{4.4}$$

To determine the k_2^{PHSD}, we first calculated the survival probability of the ϕ meson for each density and Lorentz factor from the PHSD data. Since the survival probability of a ϕ meson with Lorentz factor γ and decay width Γ over a time step Δt is given by

$$p(\Gamma, \Delta t, \gamma) = \exp(-\frac{\Gamma \Delta t}{\hbar \gamma}), \tag{4.5}$$

we applied Eq. (4.4) to Γ in Eq. (4.5) and fitted the data with k_2^{PHSD} as a free parameter. As a result, the value of k_2^{PHSD} was found to be 7.18. Figure 4.13 shows an example of the fit, and Fig. 4.14 displays the density dependence of k_2^{PHSD}.

If the absorption probability is proportional to the number (or density) of surrounding hadrons, k_2^{PHSD} should remain constant. However, as seen in Fig. 4.14, it increases up to $0.25\,\mathrm{fm}^{-3}$ and then decreases. To investigate this behavior, we performed the following analysis for the 12 GeV pCu reactions.

Figure 4.15 shows the density dependence of the total width calculated in PHSD, along with the contributions of each absorption and decay channel. The total width is derived from k_2^{PHSD} (Fig. 4.14), and the contribution of each channel is calculated by multiplying the total width by the corresponding fraction at each density. The black dashed line shows the total width using $k_2^{\mathrm{PHSD}} = 7.18$, which exhibits a significant deviation above $0.16\,\mathrm{fm}^{-3}$. It is clear that the ϕB-string channel is dominant and shapes this behavior.

Figure 4.16 shows the density dependence of the number of baryons that can react with the ϕ meson in ϕB interactions, as explained in Sect. 3. This shape closely resembles that of the total width in Fig. 4.16, suggesting that the correlation between baryon number and density governs the observed behavior. The density in these calculations follows the PHSD prescription, i.e., averaged over all events in the ensemble. Figure 4.17 shows the results when the density is computed only from baryons in the same event as the ϕ meson. In this case, the baryon number appears almost proportional to the density. Therefore, the density dependence of k_2^{PHSD} is caused by defining the density across all events in the ensemble, while the actual reacting baryons belong

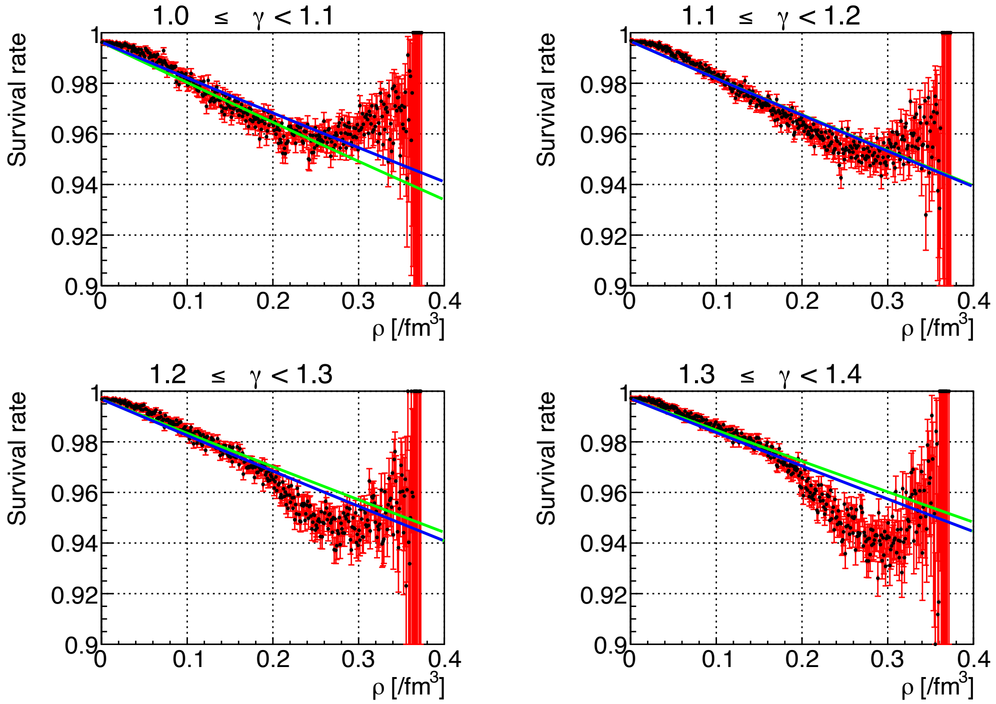

Figure 4.13: Density dependence of the survival probability of ϕ mesons for several values of Lorentz factor (γ) obtained from PHSD. Black points with red error bars represent the data points. Green line shows the density dependence of the survival probability with $k_2^{\mathrm{PHSD}} = 7.18$. Blue line represents the fit results using only the data in each panel.

only to the same event. Although this treatment is somewhat problematic, the influence of k_2^{PHSD} on the present analysis is minor, and we proceed with this definition.

Using the above procedure, we generated the density distribution and the two-dimensional distribution of transverse and longitudinal momenta for each density bin. The bin widths are set to $0.01\,\mathrm{fm}^{-3}$ for density, $0.2\,\mathrm{GeV}/c$ for longitudinal momentum, and $0.05\,\mathrm{GeV}/c$ for transverse momentum. These values were confirmed to be sufficient since the distributions are either flat or insensitive to variations within each bin.

Figure 4.18 shows the distributions of the density, transverse momentum, and longitudinal momentum for each target and density region with the broadening parameter set to zero. Figure 4.19 represents the correlation

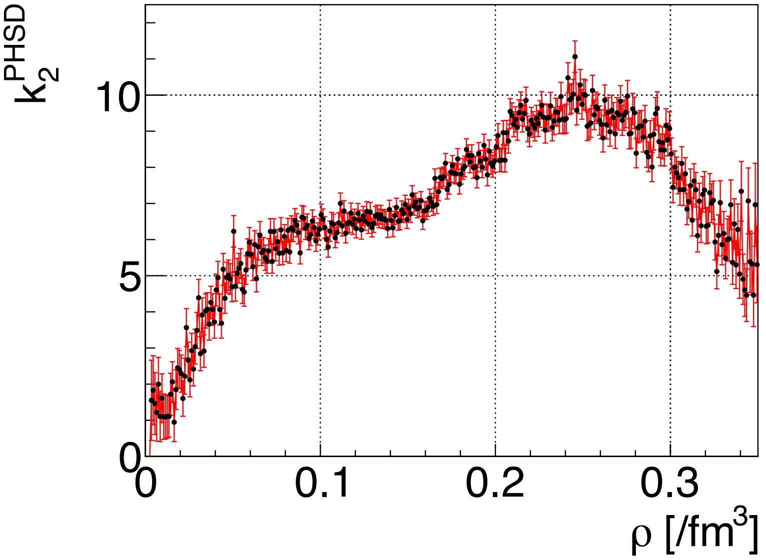

Figure 4.14: Density dependence of k_2^{PHSD} obtained from PHSD. Black points with red error bars represent the data points.

between transverse and longitudinal momentum for each target and density region with the broadening parameter set to zero. Since the population at $\rho = 0$ is significantly larger than at other densities, a separate momentum distribution was prepared for $\rho = 0$ in the analysis.

The generation of mass and momentum of ϕ mesons at their decay proceeds as follows:

1. Determine whether $\rho = 0$ or $\rho \neq 0$ based on a random sampling using their relative probabilities.
2. If $\rho \neq 0$, sample a value of ρ from the density distribution.
3. Sample the momentum from the longitudinal-transverse momentum distribution corresponding to the chosen density.
4. Generate a Breit–Wigner distribution using the chosen density, shift parameter, broadening parameter, and partial-width scenario, and randomly sample the mass.

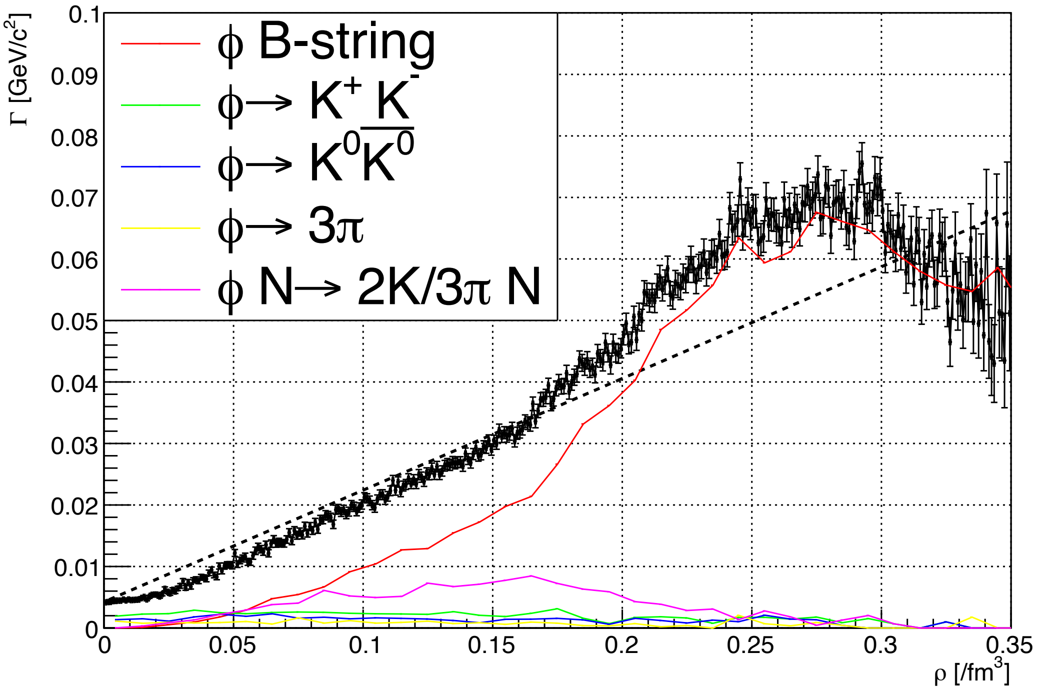

Figure 4.15: Density dependence of the ϕ-meson decay width contributions from each absorption and decay channel, calculated with PHSD. Black points represent the total width. Black dashed line corresponds to the case where $k_2^{\mathrm{PHSD}} = 7.18$ is substituted into Eq. (4.4). Red, green, blue, yellow, and purple lines represent ϕB-string, $\phi \to K^+K^-$, $\phi \to K^0\bar{K}^0$, $\phi \to 3\pi/2KN$, respectively. Uncertainties are omitted for each individual absorption and decay channel, and processes with negligible contributions are omitted.

4.3.2 Internal Radiative Correction

In measurements of electromagnetic decays such as $\phi \to e^+e^-$, it is essential to apply internal radiative corrections (IRC) to account for various electromagnetic processes occurring during the actual decay. Typical processes considered in this correction include internal bremsstrahlung, vertex correction, and vacuum polarization (Fig. 4.20). Among these, internal bremsstrahlung has the most significant impact and, in particular, produces a tail structure on the low-mass side of the spectrum, making it especially important. In the

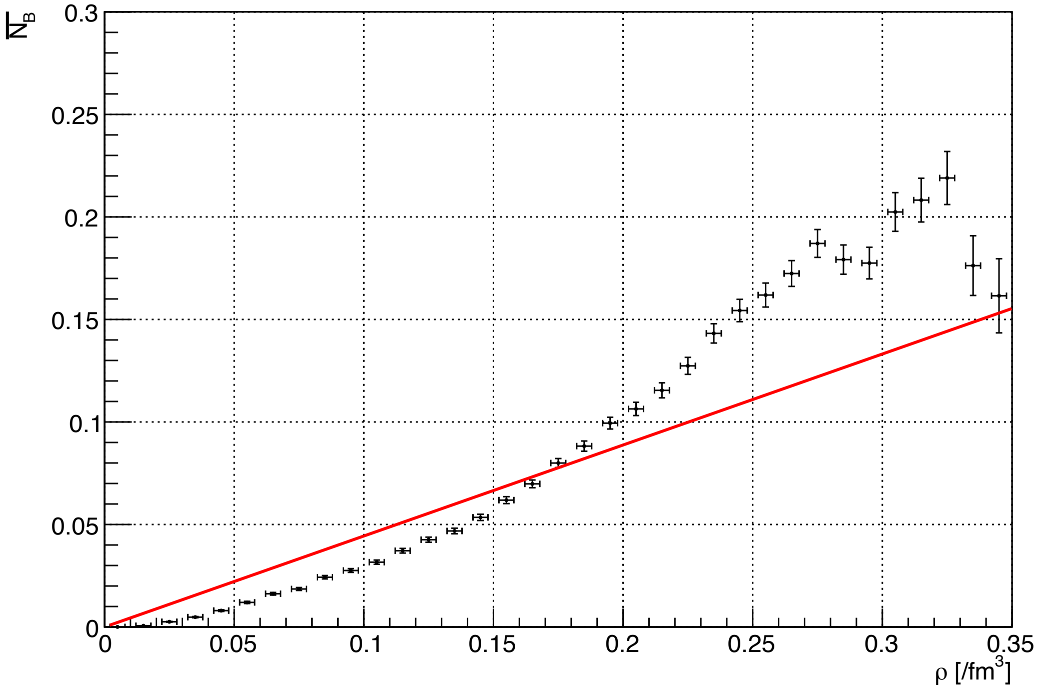

Figure 4.16: Density dependence of the number of baryons capable of undergoing ϕB reactions. The baryon number is averaged over all events in the ensemble. Black points represent the data, and red line shows the fit assuming a proportional relation.

present analysis, the correction was performed using PHOTOS 3.64 [67], a software package that simulates internal bremsstrahlung via the Monte Carlo method. Figure 4.21 shows the result of applying the IRC to a spectrum based on the Breit–Wigner shape of the ϕ meson. It can be seen that the IRC increases the event counts over a wide range, from around 0.95 GeV/c^2 up to the resonance mass region, highlighting the importance of incorporating this contribution correctly.

4.3.3 Experimental Effects

Electrons and positrons originating from ϕ-meson decays lose energy while passing through materials such as the target, detectors, and support struc-

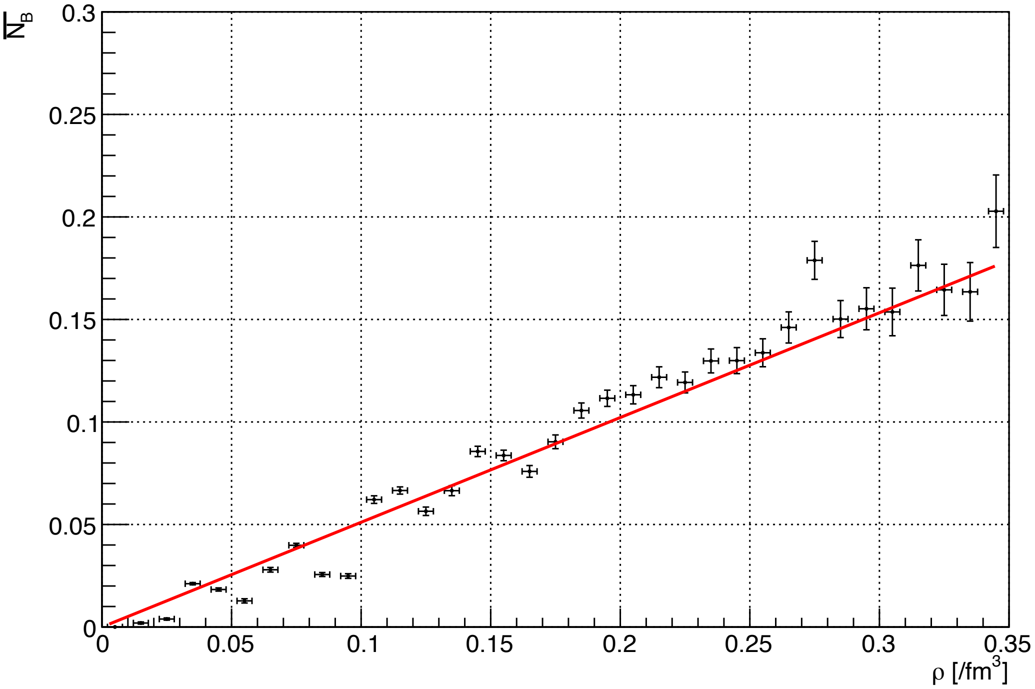

Figure 4.17: Density dependence of the number of baryons capable of undergoing ϕB reactions. The baryon number is counted only in events containing the ϕ meson, not averaged over the ensemble. Black points represent the data, and red line shows the fit assuming a proportional relation.

tures, due to the Bethe–Bloch energy loss and external radiative corrections. To account for these effects and to simulate the trajectories of these particles and obtain their hit positions on the detectors, we employed Geant4.

The detector geometry and magnetic field used in the simulation were identical to those employed in the analysis of the experimental data (Ref. [44]). The geometry was calibrated using data taken without a magnetic field. The magnetic field map was derived by comparing the field calculated with TOSCA to the measured field. The validity of these settings was confirmed using the spectra of Λ and K^0_S.

The e^+e^- pairs, generated from the ϕ mesons including the effects of IRC described in Sect. 4.3.2, were assumed to decay isotropically in the

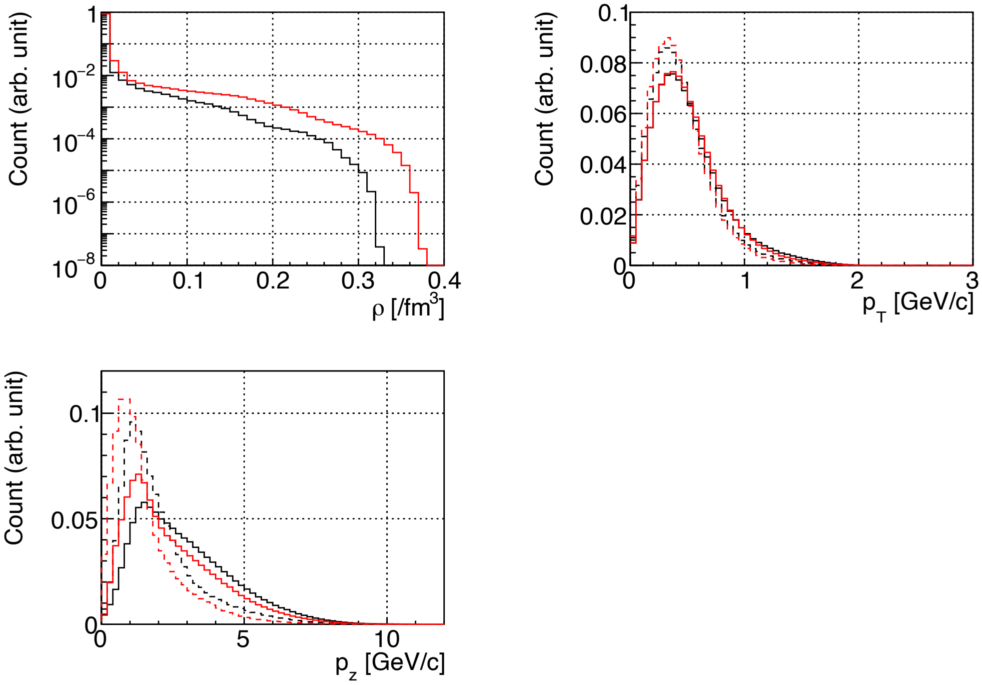

Figure 4.18: Density distribution at the ϕ meson position (upper left), transverse momentum distribution (upper right), and longitudinal momentum distribution (lower left). The distributions are normalized to unity. Black lines correspond to pC reactions, and red lines to pCu reactions. Solid lines indicate $0 \leq \rho < 0.01\,\mathrm{fm}^{-3}$, while dashed lines indicate $0.1 \leq \rho < 0.11\,\mathrm{fm}^{-3}$.

center-of-mass frame and then injected into Geant4 simulations with the defined target geometry to obtain the detector hit positions. The hit positions were smeared using a Gaussian distribution with the standard deviation σ, which corresponds to the detector resolution described in Sect. 2.1.4, and the momenta at the decay point were reconstructed using a Runge–Kutta fitting method. The Geant4 version, setup, position smearing, tracking codes, magnetic field map, and geometry files were all identical to those employed in Ref. [44].

Finally, we applied the same event-selection cuts as used in the experimental data analysis and weighted the data by the detector efficiency.

Figure 4.22 compares the ϕ-meson spectrum before the Geant4 simulation with that reconstructed from the tracked e^+e^- pairs using the invariant mass

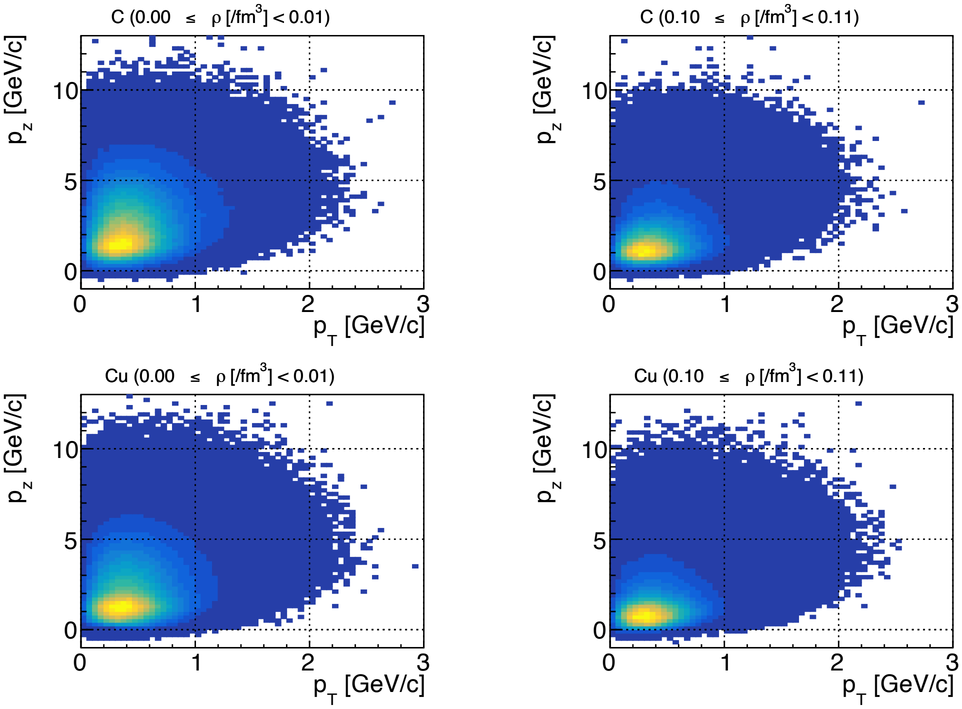

Figure 4.19: Samples of correlation between the transverse and longitudinal momenta of ϕ mesons. The upper panels correspond to pC reactions, while the lower panels correspond to pCu reactions. The left panels show $0 \leq \rho < 0.01\,\mathrm{fm}^{-3}$, whereas the right panels show $0.1 \leq \rho < 0.11\,\mathrm{fm}^{-3}$.

method. As a result of the energy loss and detector resolution, the mass slightly decreases while the width becomes broader.

4.3.4 Statistics for Each Data Set

When comparing the simulated spectra with the experimental data, it is necessary to classify the data according to the factors that produce different distributions and then sum them accordingly. In the present analysis, the data were classified by the year of data acquisition, the target material, and the arm pair (the combination of spectrometer arms in which the electron and positron were detected).

The experimental data were collected during two separate runs in 2001 and 2002. Since the target configuration and the spectrometer magnets dif-

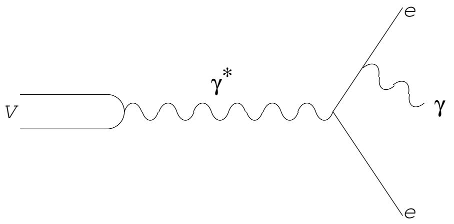

Internal Bremsstrahlung

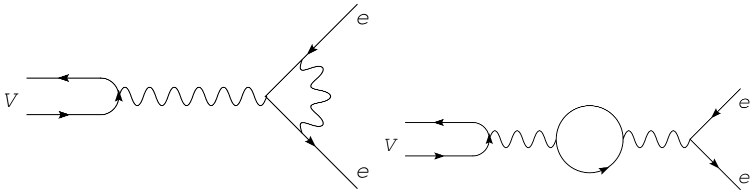

Vertex Correction Vacuum Polarization

Figure 4.20: Feynman diagrams of internal bremsstrahlung, vertex correction, and vacuum polarization. Figure is adapted from Ref. [44].

fered between these runs, some aspects of the analysis must be treated differently. For the targets, one carbon target and two copper targets were used in 2001, whereas two additional copper targets were added in 2002 (Table 2.7). Moreover, part of the spectrometer magnet was damaged between 2001 and 2002. Although Ref. [44] addressed this by modifying the magnetic field map used for the analysis, an incomplete correction could lead to shifts in the mass spectrum (offsets) or changes in resolution. This correction will be discussed in Sect. 4.3.5.

Additionally, the data consists of events where the electron and positron were detected in the left and right spectrometer arms, respectively, resulting in two possible patterns:

- the positron detected on the left arm and the electron on the right (LR)
- the positron detected on the right arm and the electron on the left (RL)

Since the momentum distributions and, consequently, the mass resolutions differ significantly between these two patterns, they must be handled separately.

From the experimental data, the invariant-mass spectra were classified by the target nucleus, data-taking year, and arm pair, and the number of ϕ

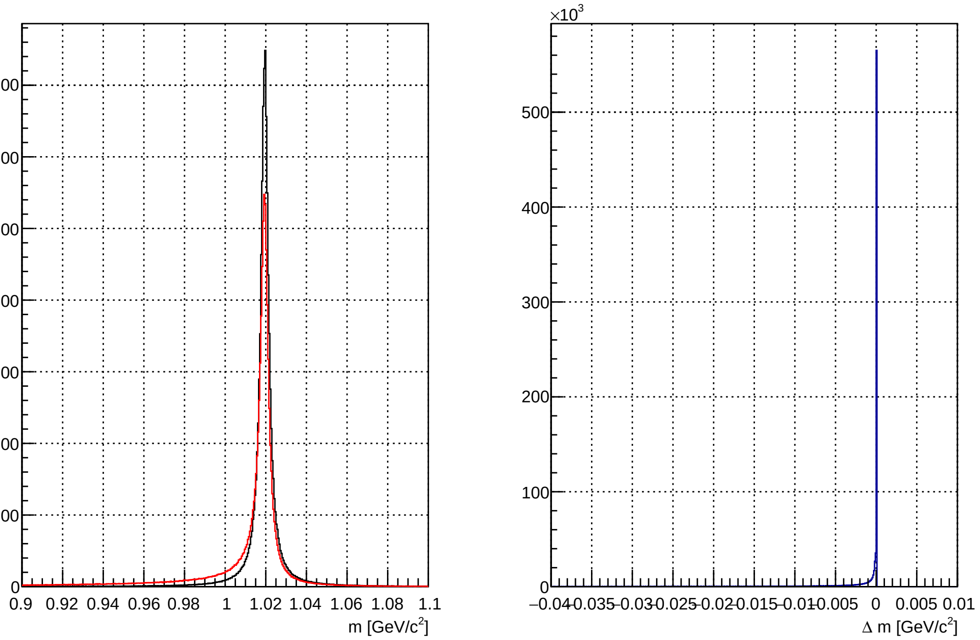

Figure 4.21: Effect of internal bremsstrahlung on the mass spectrum. In the left panel, the black line represents masses randomly sampled from a Breit–Wigner distribution using the resonance mass and width of the ϕ meson [1], while the red line shows the result after applying internal bremsstrahlung. The right panel shows the mass shifts of individual ϕ mesons due to internal bremsstrahlung.

mesons was counted for each category. The background was determined by fitting a quadratic function to the mass regions ($0.85\,\mathrm{GeV}/c^2$ to $1.15\,\mathrm{GeV}/c^2$) outside the expected signal region ($0.95\,\mathrm{GeV}/c^2$ to $1.05\,\mathrm{GeV}/c^2$). The signal yield was then obtained by subtracting the fitted background from the counts in the signal region. The ratio of the yields obtained in 2001 (N_{2001}) and 2002 (N_{2002}) is shown in Table 4.6.

Due to the limited total statistics, further subdivision by $\beta\gamma$ or by each copper target was not feasible. The number of ϕ mesons produced for each Cu target is determined by the beam intensity and the target thickness. In the runs conducted in the same year, the beam intensity was identical, and, as shown in Table 2.7, the target thicknesses were also nearly the same.

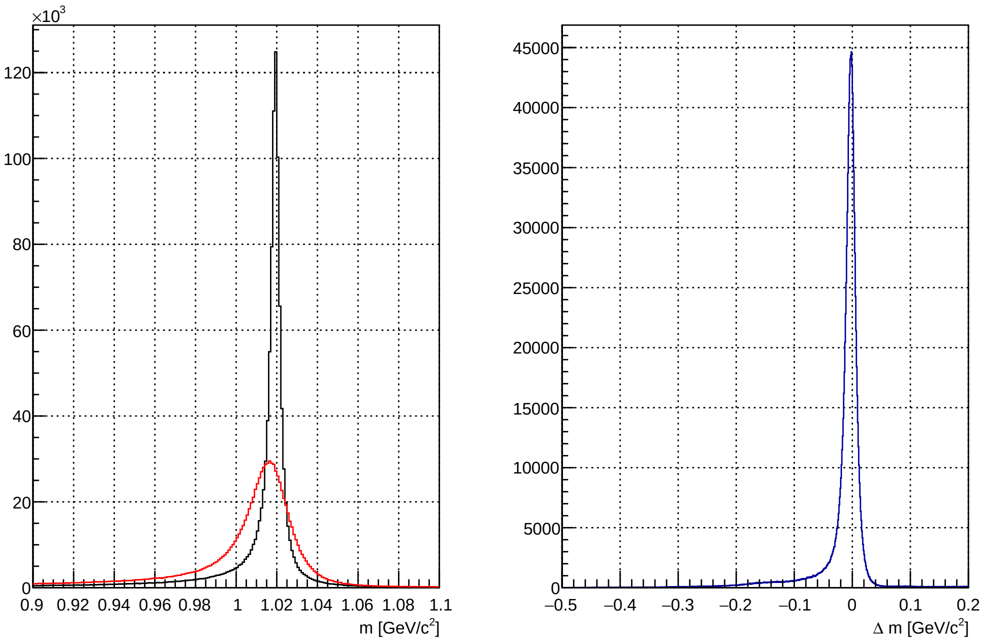

Figure 4.22: Impact of experimental effects on the mass spectrum. Black line in the left panel represents the spectrum of ϕ mesons with IRC, generated using the method described up to Sect. 4.3.2. Red line is obtained from the decay of the black-line ϕ mesons into e^+e^- pairs, with additional effects of energy loss, hit-position smearing, and tracking applied. ϕ mesons that were not detected due to tracking inefficiencies have been excluded from the black line. Neither the black nor the red line includes the effects of cut conditions or efficiency. Furthermore, the corrections discussed in Sect. 4.3.4 and Sect. 4.3.5 have not been applied. The right panel shows the difference in mass before and after the application of experimental effects for each ϕ meson.

Therefore, the production yields were almost equal. Thus, to obtain the ratio of statistics among the targets, we considered only the effects of detector acceptance, detection efficiency, and selection cuts.

Regarding the LR/RL ratio ($= N_{\mathrm{LR}}/N_{\mathrm{RL}}$), although the simulation is expected to reproduce the experimental data, it failed to do so, as shown in Table 4.7. The same issue was reported in Ref. [44], and we therefore adjusted the LR/RL ratio to match the experimental data, as was done in that reference.

4.3.5 Additional Corrections

The decay products from $\Lambda \to p\pi^-$ and $K_S \to \pi^+\pi^-$ have relatively small Q-values, and thus their hit positions on the detector are close to each other, making the impact of detector geometry misalignment minimal. On the other hand, $\phi \to e^+e^-$ has a large Q-value, and the experiment recorded only those events where one track was detected on each side of the beam axis. As a result, residual detector geometry misalignments, which cannot be fully corrected by the aforementioned method, are expected to remain.

To address this, we used the experimental data of ϕ mesons with $\beta\gamma > 1.5$,

Table 4.6: Ratio of the yields in 2001 and 2002 for each target nucleus and arm pair. Error values are statistical uncertainties. Since the C target was placed at the same position in both 2001 and 2002, the ratio for the C target was not used in the analysis.

Target nuclei	Arm pair	N_{2001}/N_{2002}
C	LR	0.53 ± 0.03
	RL	0.59 ± 0.06
Cu	LR	0.52 ± 0.03
	RL	0.59 ± 0.05

Table 4.7: Ratio of the yields in LR-pair and RL-pair for each target. Error values are statistical uncertainties.

	Target ID	$N_{\mathrm{LR}}/N_{\mathrm{RL}}$
Experiment	Sum of all targets	2.5 ± 0.1
Simulation	1	2.2 ± 0.0
	2	2.1 ± 0.0
	3	2.3 ± 0.0
	4	1.8 ± 0.0
	5	1.7 ± 0.0

which are assumed to decay in vacuum and are unaffected by nuclear medium effects, to correct the mass spectrum. Two types of correction parameters were introduced: mass offsets and a Gaussian smearing. First, the experimental data were divided into four subsets based on the data acquisition year and the arm pair, and separate offset parameters were determined for each subset. In this process, contributions from one carbon target and two or four copper targets had to be combined. The smearing parameter was taken to be common across all data. The results and the comparison with Ref. [44] is summarized in Table 4.8, indicating that the obtained parameter values are consistent with those reported in Ref. [44] within uncertainties. Although the uncertainties were not evaluated in the present analysis, they are expected to be of the same order as those in Ref. [44], since the same experimental data and method were used.

4.3.6 Summary of Present Analysis Flow

The analysis flow is summarized as follows:

- Based on the PHSD output, the correlation among the density, longitudinal momentum, and transverse momentum at the time of ϕ-meson decay was constructed, from which mass–momentum pairs were sampled.

- Spectra were generated by applying the IRC, experimental effects, and analysis cuts, and the entire spectrum was further shifted and smeared.

Table 4.8: Values of the offset and additional Gaussian smearing applied to the mass spectra. Error values of Ref. [44] are statistical (first) and systematic (second) uncertainties. Uncertainties of present analysis are not evaluated.

	Year	Arm pair	Present analysis	Ref. [44]
Offset [MeV/c^2]	2001	LR	0.70	$0.7 \pm 0.9^{+0.0}_{-0.6}$
		RL	1.62	$0.6 \pm 2.8^{+0.5}_{-0.7}$
	2002	LR	-0.88	$-0.7 \pm 0.6^{+0.0}_{-0.4}$
		RL	4.59	$4.2 \pm 1.3^{+0.1}_{-0.2}$
Smear [MeV/c^2]	-	-	3.89	$3.6 \pm 1.3^{+1.2}_{-0.0}$

- The simulated data were combined so that their yields matched the relative ratios of data-taking years and LR/RL arm pairs.
- Background events were added, and the result was compared with the experimental data.

In this analysis, the experimental data, the parameterization of spectral modifications (Eqs. (2.2) and (2.3)), the IRC, the experimental effects, and the analysis cuts were taken from Ref. [44]. The global shift and smearing of the spectrum were recalculated because they depend on the simulated data. The relative ratios of data-taking years and LR/RL arm pairs were newly recalculated in a way independent of the simulated data. The density and momentum of the ϕ mesons produced in pA reactions at their decay were entirely recalculated. The masses were calculated using Eqs. (2.1), (2.2), and (2.3), as in Ref. [44]. However, in the present analysis the density distributions and their correlations with momentum, which are required to compute m_ϕ and Γ_ϕ, were obtained using PHSD.

4.3.7 Comparison of Momentum Distribution

Figure 4.23 shows the comparison between various momentum distributions of the ϕ mesons obtained using the methods described so far and the experimental data. A good agreement between the simulation and the experimental results is observed.

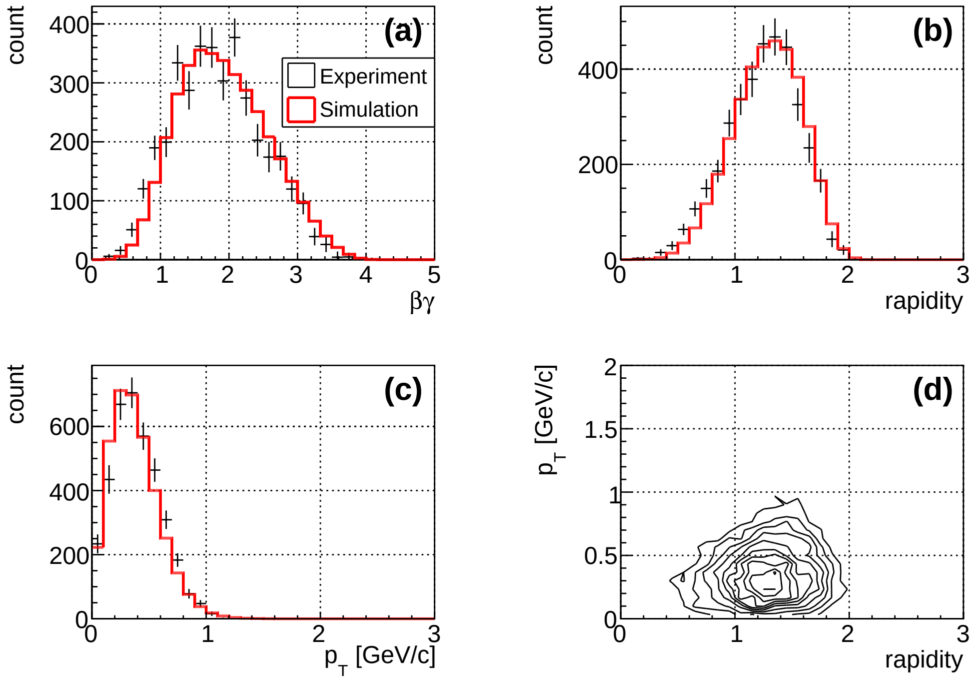

Figure 4.23: Momentum distributions obtained from the experiment and the present simulation. The panels show the $\beta\gamma$ distribution (upper left), rapidity (upper right), transverse momentum (lower left), and the correlation between rapidity and transverse momentum (lower right). Black points represent the experimental data, while red lines represent the simulation. The simulation is fitted to the experimental data with the vertical-axis scale treated as a free parameter.

Chapter 5

Result and Discussion

5.1 Fit Results

In the present analysis, three models for the spectral modification were assumed and used in the fitting procedure:

- **Model A:** No spectral modification. This is equivalent to setting both the shift and broadening parameters to zero.
- **Model B:** The shift and broadening parameters are common across all momentum ($\beta\gamma$) regions. This is the same model as used in Ref. [28].
- **Model C:** Momentum dependence is introduced to the shift and broadening parameters. In this case, the same shift and broadening parameters are used for the pC and pCu spectra within each $\beta\gamma$ region, but different $\beta\gamma$ regions are allowed to have different parameter values.

First, in order to demonstrate the presence of significant in-medium modification, we employed Model A. In this case, it is expected that the spectrum without assuming any modification was able to reproduce the shape in the spectrum expected to be less affected by density, while it failed to reproduce the shape in the spectrum expected to be more strongly affected by density. The density effect is considered to be smaller for smaller nuclei and for ϕ mesons with larger $\beta\gamma$. Next, following Ref. [28], we performed fits applying common shift and broadening parameters to all $\beta\gamma$ regions (Model B). Furthermore, using Model C, which incorporates the momentum dependence of the in-medium resonance mass and width as predicted by QCD sum rules [23, 26] and chiral effective theory [19], we carried out additional fits. For Models B and C, two cases for the density dependence of the partial width for e^+e^- decay are considered: Model B-1 and C-1 assume a density-dependent partial width as described by Eq. (2.4), while Model B-2 and C-2 assume a constant partial width (Table 5.1).

5.1.1 Model without Spectral Modification (Model A)

Figure 5.1 and Table 5.2 show the fit results under the assumption that there is no spectral modification of the ϕ meson. While the spectra in the fastest $\beta\gamma$ regions are well reproduced, the spectrum with the slowest $\beta\gamma$ regions in the pCu reaction yields $\chi^2/\mathrm{dof} = 93/53$, which is rejected at the 99% confidence level.

Table 5.1: Spectral modification models considered in the present analysis.

	Momentum dependence of k_1 and k_2	Partial width
Model A	No modification	
Model B-1	No	Density dependent
Model B-2	No	Constant
Model C-1	Yes	Density dependent
Model C-2	Yes	Constant

Table 5.2: χ^2/dof (degree of freedom) for each of the six fits shown in Fig. 5.1. The number of bins used for the fit is 54, and the only fit parameter is the scale factor of the signal spectra generated with PHSD.

$\beta\gamma$	χ^2/dof (pC)	χ^2/dof (pCu)
Slow	38/53	93/53
Middle	68/53	47/53
Fast	46/53	54/53

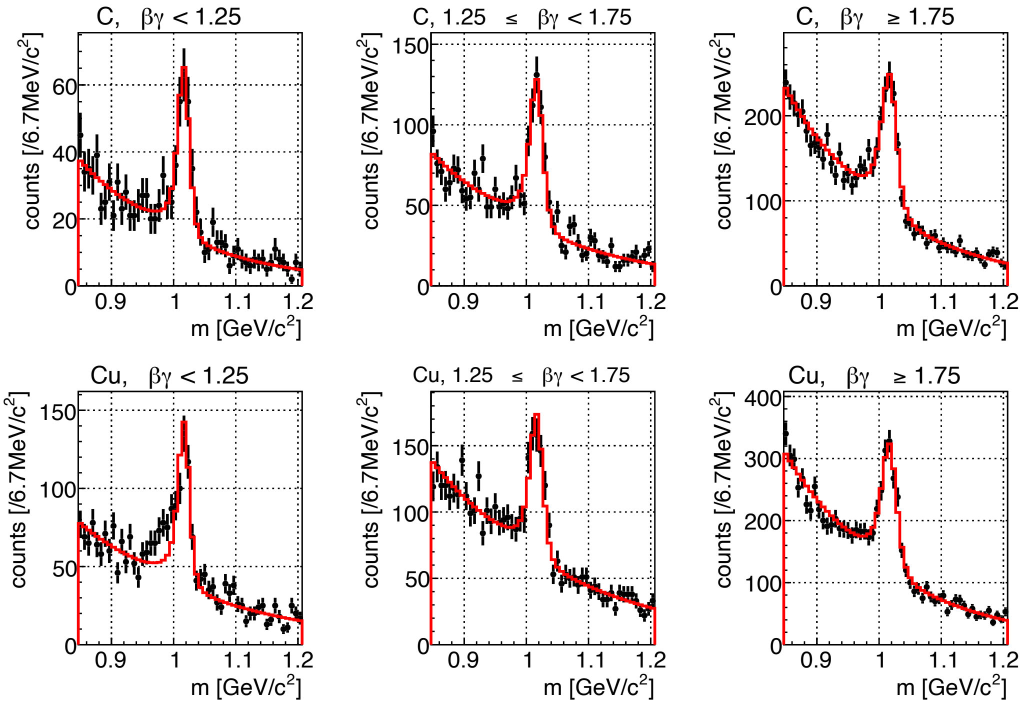

Figure 5.1: Invariant mass distributions of e^+e^- pairs classified by target nucleus and the $\beta\gamma$ of the parent particle, along with the fit results assuming no spectral modification of the ϕ meson. Black points with error bars represent the experimental data. Red lines indicate the fit functions.

5.1.2 Model without Momentum-Dependent Shift and Broadening Parameters (Model B-1, B-2)

Next, we introduced common shift and broadening parameters across all spectra and calculated the χ^2 values for the various parameters. As described in Sect. 2.2.4, the shift and broadening parameters were expressed in the forms of Eqs. (2.2) and (2.3), respectively. The partial decay width to e^+e^- was either density-dependent as in Eq. (2.4) or fixed at a constant value depending on the model type. The total and partial widths affect the decay density distribution of the ϕ meson, while the resonance mass and total width modify the Breit–Wigner distribution at each density.

Figure 5.2 shows the χ^2 dependence on the shift and broadening parameters when fitting the six spectra. Table 5.3 summarizes the minimum χ^2

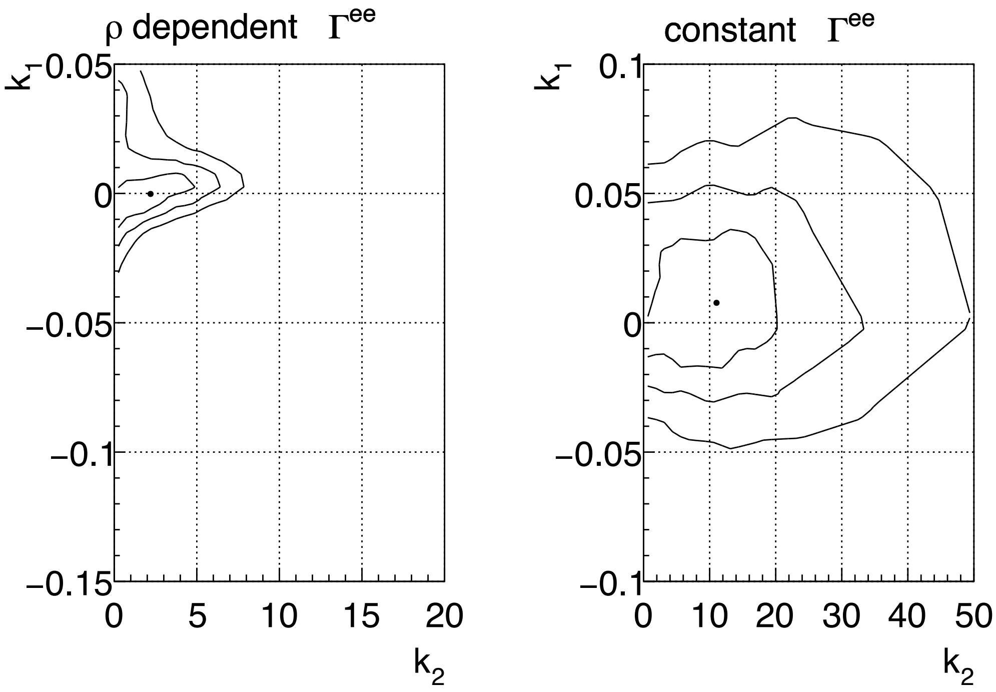

Figure 5.2: χ^2 dependence on the shift and broadening parameters for the fit to all six spectra. Left panel shows Model B-1 and the right panel shows Model B-2. Black points indicate the parameter set yielding the minimum χ^2. Three contour lines correspond to differences from the minimum χ^2 by 1σ ($\Delta\chi^2 = 2.30$), 2σ ($\Delta\chi^2 = 6.18$), and 3σ ($\Delta\chi^2 = 11.83$), respectively. The position and value of the minimum χ^2 were determined by fitting the points with low χ^2 using a paraboloid. The contour map was interpolated from simulated points.

values, the corresponding parameters, and each spectrum's contribution for both Models B-1 and B-2. The best-fit parameters and their corresponding χ^2 values were determined via a paraboloid fit. Figure 5.3 presents the best-fit results for Models B-1 and B-2. The minimum χ^2/dof for Models B-1 and B-2 are 343/316 and 342/316, corresponding to p-values of 14% and 15%, respectively.

Since common parameters are used for all spectra, we cannot discuss the fit quality for each spectrum individually. However, for the slowest ϕ meson spectrum in the pCu reaction, which could not be reproduced in Model

A, the χ^2 values for Models B-1 and B-2 are 89 and 86 (with 54 bins), respectively. As seen in the lower-left panel of Fig. 5.3, the fit still does not adequately reproduce the experimental data. Therefore, in this analysis, we newly allowed the shift and broadening parameters to depend on momentum, enabling different parameters for spectra with different $\beta\gamma$ ranges.

5.1.3 Model with Momentum-Dependent Shift and Broadening Parameters (Model C-1, C-2)

In this model, we apply the same shift and broadening parameters to only to two spectra in the same $\beta\gamma$ region for both pC and pCu reactions, and search for the parameters that minimize the sum of their χ^2 values. As mentioned at the beginning of this chapter, the momentum dependence of the shift and broadening parameters has been pointed out by theoretical calculations. However, since there is no reason for them to depend on the target nucleus, we treated them in this manner. Figure 5.4 shows the dependence of the total χ^2 on the shift and broadening parameters when fitting the spectra in each $\beta\gamma$ region. In the slowest $\beta\gamma$ region of Model C-2, we performed simulations up to $k_1 = 0.5$ and $k_2 = 100$, but could not find the minimum χ^2. Since $k_1 > 0.5$ and $k_2 > 100$ are considered outside the physically meaningful

Table 5.3: Minimum χ^2 values, best-fit shift and broadening parameters, and contributions from each spectrum for the case with momentum-independent parameters. The minimum χ^2 values were obtained as described in the caption of Fig. 5.2.

Model	k_1	k_2	$\beta\gamma$	χ^2 (C)	χ^2 (Cu)	χ^2/dof (total)
B-1	0.000	2.2	Slow	38	89	
			Middle	68	46	
			Fast	46	56	
			Total			343/316
B-2	0.008	11.0	Slow	38	86	
			Middle	69	46	
			Fast	47	57	
			Total			342/316

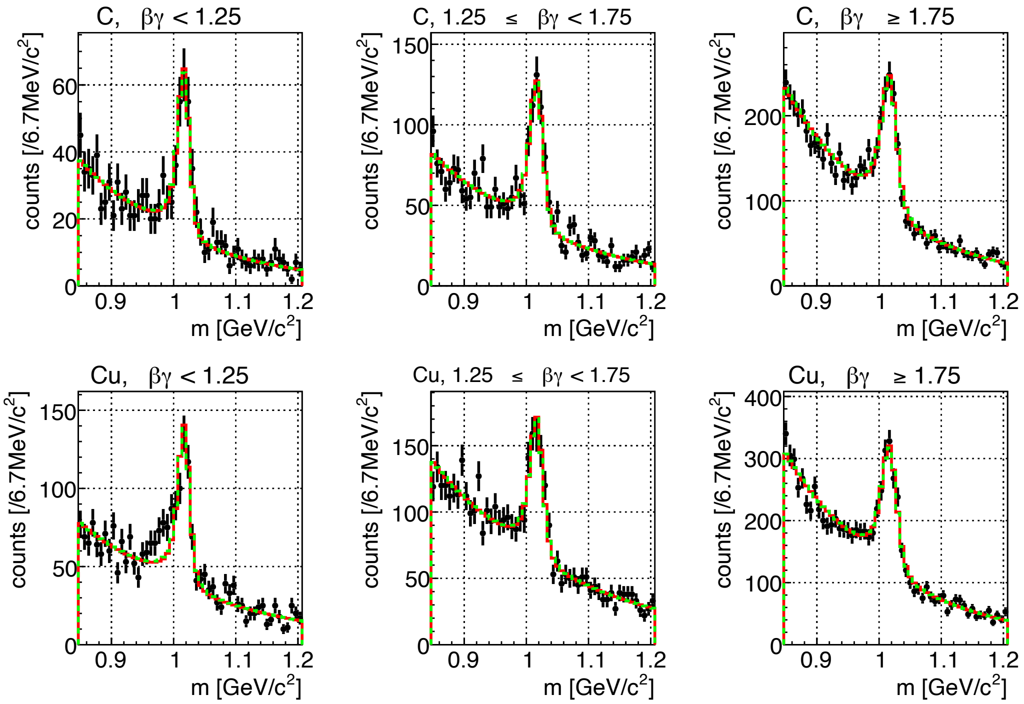

Figure 5.3: Fit results for the momentum-independent case. Black points and error bars indicate experimental data, red solid lines represent Model B-1, and green dashed lines represent Model B-2. The exact parameter values corresponding to the minimum χ^2 were not simulated. Instead, the closest simulated parameter sets were used: $(k_1, k_2) = (0, 2)$ for Model B-1 and $(0.01, 10)$ for Model B-2.

range, no further simulations were conducted.

Table 5.4 shows the minimum χ^2 values for Models C-1 and C-2 along with the corresponding shift and broadening parameters.

Figure 5.5 shows the best-fit results for Models C-1 and C-2. The spectra in the slowest $\beta\gamma$ region of the pCu reaction are reproduced well. The spectra in the corresponding $\beta\gamma$ region for the pC reaction, which use the same parameters, are also well reproduced.

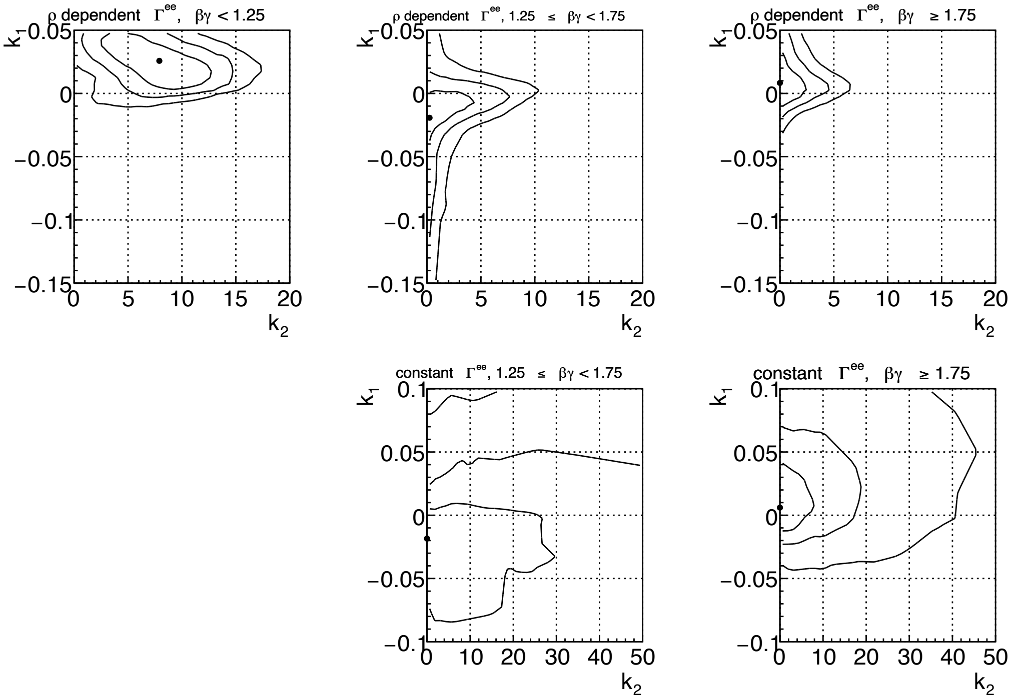

Figure 5.4: Dependence of the total χ^2 on the shift and broadening parameters for each $\beta\gamma$ region. Upper panels correspond to Model C-1 and lower panels to Model C-2, arranged from left to right as slow, middle, and fast regions. Black points indicate the parameters giving the minimum χ^2. The definitions of the contour lines, the evaluation method of the minimum χ^2, and the interpolation method are the same as in Figure 5.2. For the slowest $\beta\gamma$ region in Model C-2, no minimum χ^2 was found within the physically reasonable parameter range, so it is omitted.

5.1.4 Comparison of Models

The different models are compared in this section. First, Model A yields a poor fit to the data in the slowest $\beta\gamma$ region for the pCu reaction, with a $\chi^2/\text{dof} = 93/53$, which is rejected at the 99% confidence level. Furthermore, in Model C-2, the shift and broadening parameters for the slowest $\beta\gamma$ region fall into an unphysical range, indicating that this model cannot reproduce the experimental data. Model B-1 is a subset of Model C-1, allowing a likelihood ratio test to be performed. The number of parameters for Models B-1 and

C-1 are 8 and 12, respectively, and their total χ^2 values are 343 and 327. Based on these values, Model B-1 is rejected at the 99% confidence level.

Although Models B-2 and C-1 are not in an inclusive relation, they can be compared using the Akaike Information Criterion (AIC), which is given by $\chi^2 + 2k$ (where k is the number of parameters or degrees of freedom). While AIC does not allow for model rejection, it enables relative comparison between models. Using AIC, we find that the AIC value of Model B-2 is 974 and the AIC value of Model C-1 is 951. Even after accounting for the increase in the number of parameters, Model C-1 reproduces the experimental data more accurately. This result is also consistent with the visual impression from Figures 5.3 and 5.5.

Table 5.4: Minimum χ^2 and the corresponding shift and broadening parameters obtained for each $\beta\gamma$ region. The slowest $\beta\gamma$ region for Model C-2 is excluded, because no minimum χ^2 was found within the physically reasonable parameter range.

Model	$\beta\gamma$	k_1	k_2	χ^2 (C)	χ^2 (Cu)	χ^2/ndf (total)
C-1	Slow	0.026	7.9	42	73	115/104
	Middle	–0.019	0.2	66	47	112/104
	Fast	0.008	0.0	45	55	100/104
C-2	Slow	-	-	-	-	-
	Middle	–0.018	0.0	66	46	112/104
	Fast	0.006	0.0	45	55	100/104

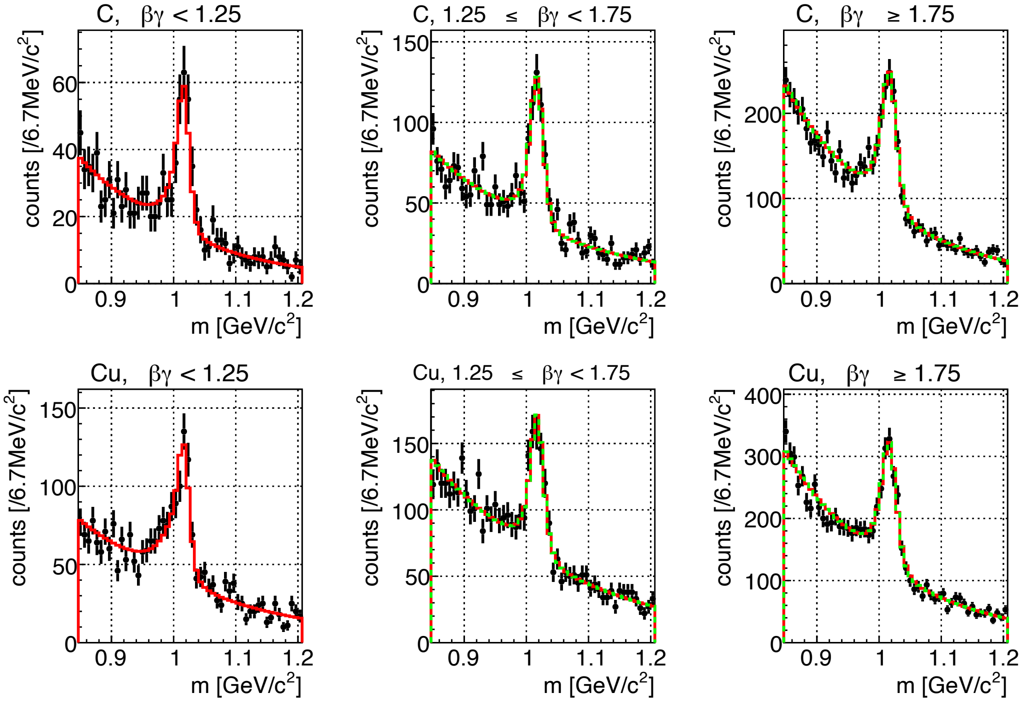

Figure 5.5: Fit results with momentum-dependent shift and broadening parameters. Black points and error bars represent the experimental data; red solid lines represent Model C-1, and green dashed lines represent Model C-2. The shift and broadening parameters used correspond to those simulated parameters closest to the best-fit ones, i.e., $(k_1, k_2) = (0.03, 8), (-0.02, 0), (0.007, 0)$ for Model C-1 (slow, middle, and fast $\beta\gamma$ region, respectively) and $(-0.02, 0), (0.01, 0)$ for Model C-2 (middle and fast $\beta\gamma$ region, respectively).

5.2 Estimation of Systematic Uncertainties

In the present analysis, three types of systematic uncertainties were estimated:

- Those arising from the instability of the target nucleus in PHSD,
- Those originating from the intrinsic k_2 in PHSD,
- Those due to the shape of the background contribution.

The first two sources stem from the PHSD model, while the third originates from the modeling of background events.

5.2.1 Systematic Uncertainty Due to the Instability of the Target Nucleus in PHSD

As described in Sect. 4.2.4, nucleons in the target nucleus gradually spread out in PHSD, even in the absence of any collisions. This is considered to originate from the inaccuracy of baryon propagation discussed in Sect. 3.6, and it is difficult to properly incorporate this effect into the analysis [66].

When simulating pA reactions with PHSD, the baryon density distribution at the time of ϕ meson decay includes both the following effects: (i) deformation of the target nucleus due to the interaction with the projectile (the intended effect), (ii) instability of the target nucleus in the simulation (the unwanted effect). Since it is not possible to isolate Effect (i) from the combined outcome, we estimate the impact of Effect (ii) using the method below.

In Sect. 4.2.4, Effect (ii) was evaluated in terms of time evolution of the Woods–Saxon distribution parameters. We calculated χ^2 values using either a static or a time-evolving Woods–Saxon distribution as the spatial density distribution, based on the best-fit parameters of Model B and Model C. The momentum and baryon density at the time of ϕ meson decay were obtained as follows:

- From the PHSD output, the production time, position, and initial momentum of the ϕ meson were obtained. The initial position was taken in the lab frame with the target nucleus center as the origin.
- Assuming the momentum remains constant, the spatial position was propagated forward in time.
- At each time step, the baryon density at the ϕ meson position was calculated assuming either a static or time-evolving Woods–Saxon distribution. The ϕ meson was assumed to decay with a probability corresponding to the local baryon density, and the decay-time baryon density and momentum distributions were obtained using the shining method.

The difference in χ^2 between the two distributions was regarded as the systematic uncertainty caused by Effect (ii). The region in the parameter space corresponding to a contour shifted by this χ^2 difference from the best-fit value was taken as the systematic uncertainty range. The results are summarized in Table 5.5.

5.2.2 Systematic uncertainty Due to k_2^{PHSD}

As discussed in Sect. 4.2.1, the density dependence of the absorption and decay processes of ϕ mesons simulated within PHSD is characterized by an effective parameter k_2^{PHSD}. In this analysis, we adopted $k_2^{\mathrm{PHSD}} = 7.18$, but as shown in Fig. 4.14, this value varies depending on the baryon density. In this section, we estimate the effect of this variation on the shift and broadening parameters.

As shown in Fig. 4.14, k_2^{PHSD} arises within the range of 0–10 depending on the density. Therefore, we re-generated the ϕ meson generator assuming $k_2^{\mathrm{PHSD}} = 0$ and 10, respectively, and scanned the shift and broadening parameters for each case. The result of the best fit parameters is represented in Table 5.6. The shift and broadening parameters obtained here are regarded as the systematic uncertainty originating from k_2^{PHSD}.

5.2.3 Systematic Uncertainty Due to the Shape of Background Events

The background shape was determined by fitting an exponential function $a\exp(-b(m-c))$ to the mass region outside the signal region ($0.953\,\mathrm{GeV}/c^2$ to $1.106\,\mathrm{GeV}/c^2$), within the fitting range of $0.847\,\mathrm{GeV}/c^2$ to $1.207\,\mathrm{GeV}/c^2$.

To estimate the systematic uncertainty due to the arbitrariness of this background determination method, we varied both the signal region and the fitting function, and repeated the scan of the shift and broadening parameters. Specifically, three combinations were tested:

Table 5.5: Value of the systematic uncertainty due to the instability of the target nucleus in PHSD, evaluated as $\Delta\chi^2$. The corresponding (k_1, k_2) values are those given in Tables 5.3 and 5.4.

Partial decay width	Slow	Middle	Fast	All $\beta\gamma$
Density dependent	0.55	0.06	0.37	0.86
Constant	-	0.11	0.30	0.25

- **Case (0):** Original signal region ($0.953\,\mathrm{GeV}/c^2$ to $1.106\,\mathrm{GeV}/c^2$) with exponential background
- **Case (1):** Original signal region with quadratic background
- **Case (2):** Modified signal region ($0.9\,\mathrm{GeV}/c^2$ to $1.1\,\mathrm{GeV}/c^2$) with exponential background

As described in Sect. 4.3.5, in the present analysis, a mass offset and Gaussian smearing were added to the simulated ϕ spectrum in order to incorporate residual effects of the magnetic field and geometry that could not be fully corrected. Since these values depend on the shape of the background, they were recalculated for each case.

The resulting shift and broadening parameters under each background condition are summarized in Table 5.7. The shift and broadening parameters obtained here are regarded as the systematic uncertainty originating from shape of background events.

5.2.4 Results Including Systematic Uncertainties

Table 5.8 summarizes the shift and broadening parameters including the systematic uncertainties discussed in this section. For model C-1, most strongly supported in the present analysis, signs of deviations of the shift and broadening parameters from zero appear in the slow and middle $\beta\gamma$ regions. Nev-

Table 5.6: Changes in the shift and broadening parameters when the PHSD intrinsic k_2 is assumed to be 0 or 10.

		Slow		Middle		Fast		All $\beta\gamma$	
Γ^{ee}	k_2^{PHSD}	k_1	k_2	k_1	k_2	k_1	k_2	k_1	k_2
ρ dep.	7.18	0.026	7.9	−0.019	0.2	0.008	0.0	0.000	2.2
	0	0.026	6.8	−0.013	0.0	0.008	0.0	−0.002	1.6
	10	0.021	8.9	−0.017	0.0	0.008	0.0	−0.001	2.0
Const.	7.18	-	-	−0.018	0.0	0.006	0.0	0.008	11.0
	0	-	-	−0.017	0.0	0.006	0.0	0.005	9.8
	10	-	-	−0.020	0.1	0.008	0.0	0.003	8.7

ertheless, due to the magnitude of the uncertainties, these signs cannot be regarded as conclusive evidence for significant deviations.

Table 5.7: Shift and broadening parameters obtained under different background modeling conditions.

		Slow		Middle		Fast		All $\beta\gamma$	
Γ^{ee}	Case	k_1	k_2	k_1	k_2	k_1	k_2	k_1	k_2
ρ dep.	(0)	0.026	7.9	–0.019	0.2	0.008	0.0	0.000	2.2
	(1)	0.029	4.7	–0.017	0.0	0.003	0.0	–0.007	0.0
	(2)	0.017	11.7	–0.021	0.0	0.007	0.0	–0.001	3.4
Const.	(0)	-	-	–0.018	0.0	0.006	0.0	0.008	11.0
	(1)	-	-	–0.020	0.0	–0.001	0.0	–0.006	0.0
	(2)	-	-	–0.024	10.0	0.004	0.0	0.011	17.1

Table 5.8: Shift and broadening parameters including uncertainties. The three uncertainties listed are: statistical (first), systematic from PHSD (second), and systematic from background modeling (third). The statistical uncertainties correspond to the bounds at $\Delta\chi^2 = 1$. For the two systematic uncertainties originating from PHSD, only the larger deviation (either positive or negative) from the central value was quoted. If the lower limit of the broadening parameter including statistical uncertainties became negative, only the 90% confidence level upper limit was quoted, with the conventional value given in parentheses. The calculation of the 90% confidence level includes the contribution from the negative region as well.

Γ^{ee}	$\beta\gamma$	k_1	k_2
ρ dep.	Slow	$0.026^{+0.021+0.015+0.003}_{-0.021-0.015-0.008}$	$7.9 \pm 3.9^{+2.9+3.8}_{-2.9-3.2}$
	Middle	$-0.019^{+0.016+0.006+0.002}_{-0.014-0.004-0.002}$	$\leq 4.8\ (0.2^{+2.8+0.7+0.0}_{-0.2-0.2-0.2})$
	Fast	$0.008^{+0.016+0.010+0.000}_{-0.017-0.010-0.006}$	$\leq 2.6\ (0.0^{+1.6+1.0+0.0})$
	All $\beta\gamma$	$0.000^{+0.010+0.009+0.000}_{-0.010-0.009-0.007}$	$\leq 6.8\ (2.2^{+2.8+2.6+1.2}_{-2.2-2.2-2.2})$
	Ref. [28]	$0.034^{+0.006}_{-0.007}$	$2.6^{+1.8}_{-1.2}$
Const.	Slow	-	-
	Middle	$-0.018^{+0.022+0.008+0.000}_{-0.023-0.008-0.004}$	$\leq 32.2\ (0.0^{+19.5+6.5+9.0})$
	Fast	$0.006^{+0.017+0.009+0.000}_{-0.017-0.009-0.007}$	$\leq 6.8\ (0.0^{+4.1+2.3+0.0})$
	All $\beta\gamma$	$0.008^{+0.018+0.009+0.004}_{-0.018-0.009-0.013}$	$11.0 \pm 8.7^{+4.3+6.8}_{-4.3-11.0}$
	Ref. [28]	$0.033^{+0.011}_{-0.008}$	$0^{+5.6}$

5.3 Comparison with Theoretical Calculations and Other Experiments

Among the results obtained in the present analysis, the shift parameter is compared with theoretical calculations based on the QCD sum rule [23, 26] and lattice QCD [19], while the broadening parameter is compared with calculations based on the nuclear dependence of the ϕ meson production cross section measured via $\phi \to K^+K^-$ decays in the COSY-ANKE experiment.

Figures 5.6 and 5.7 show the momentum dependence of the differences in resonance mass and decay width between normal nuclear density and vacuum, as calculated from the shift and broadening parameters listed in Table 5.8. In the present analysis, the model with density-dependent partial width and momentum-dependent shift and broadening parameters (Model C-1), represented as black points in Fig. 5.6, is most strongly supported. However, the uncertainties of the parameters of each momentum region are large, and no definite conclusion can be drawn regarding the trend. The shift parameter shows values comparable to or smaller than those of Ref. [28] across the entire momentum region.

The theoretical curve shown in the figures was obtained as follows. According to the QCD sum rule (Eq. (50) of Ref. [26]), the momentum dependence of the ϕ meson mass at normal nuclear density can be expressed as:

$$m_\phi(\rho = \rho_0, p) - m_\phi(\rho = 0, p = 0) = a + bp^2, \tag{5.1}$$

where the parameter b differs depending on whether the ϕ meson is in a transverse or longitudinal polarization state (b^T and b^L). Here, we approximate $b = (2b^T + b^L)/3$ using the values b^T and b^L from Ref. [26]. The parameter a, the mass shift at zero momentum, is evaluated using Eq. (13) in Ref. [25]:

$$a = b_0 - b_1\sigma_{sN}, \tag{5.2}$$

where σ_{sN} is the strangeness sigma term, defined as $\sigma_{sN} = m_s\langle N|\bar{s}s|N\rangle$. Here, m_s is the strange quark mass, and $\langle N|\bar{s}s|N\rangle$ is the nucleon matrix element of the $\bar{s}s$ operator. The value of σ_{sN} was taken from lattice QCD calculations, using the average of Eqs. (449) and (450) in Ref. [20], which represent recent results for $N_f = 3$ and $N_f = 4$ simulations, where N_f stands for the number of active flavors in the lattice QCD calculations, for which quark loops are taken into account.

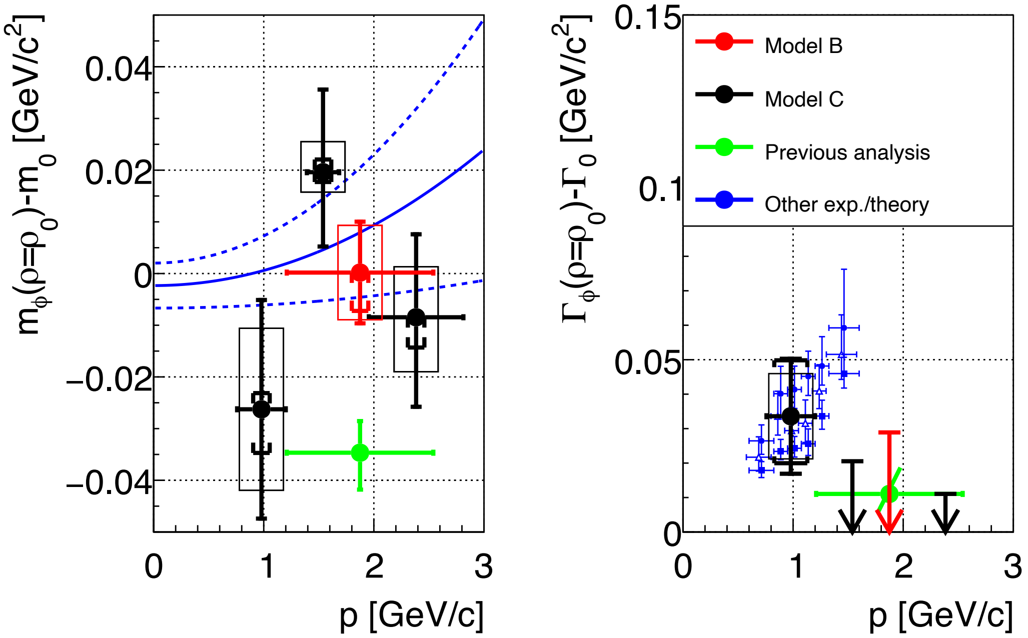

Figure 5.6: Momentum dependence of the difference in resonance mass and decay width between normal nuclear density and vacuum in Models B-1 and C-1. Left (right) panel shows the result for the resonance mass (width). Black, red, and green points correspond to Model C, Model B, and the values from Ref. [28], respectively. Vertical error bars represent statistical uncertainties (lines), systematic uncertainties due to PHSD (squares), and those due to background modeling (brackets). Horizontal error bars represent the RMS of the momentum distributions in each $\beta\gamma$ region. Blue solid line in the left panel is the theoretical prediction from the QCD sum rule and lattice QCD, and the dashed line represents its uncertainty band. Blue points in the right panel are the results of COSY-ANKE experiment extracted from Fig. 4(a) of Ref. [30], using different theoretical models (indicated by different markers) as described in Ref. [68–70]. To improve visual clarity, certain error bars are displayed at an angle.

Comparing these theoretical results with the present analysis, the results from Ref. [28] fall outside the theoretical band, while the present results lie within the uncertainty range. However, the present results do not show

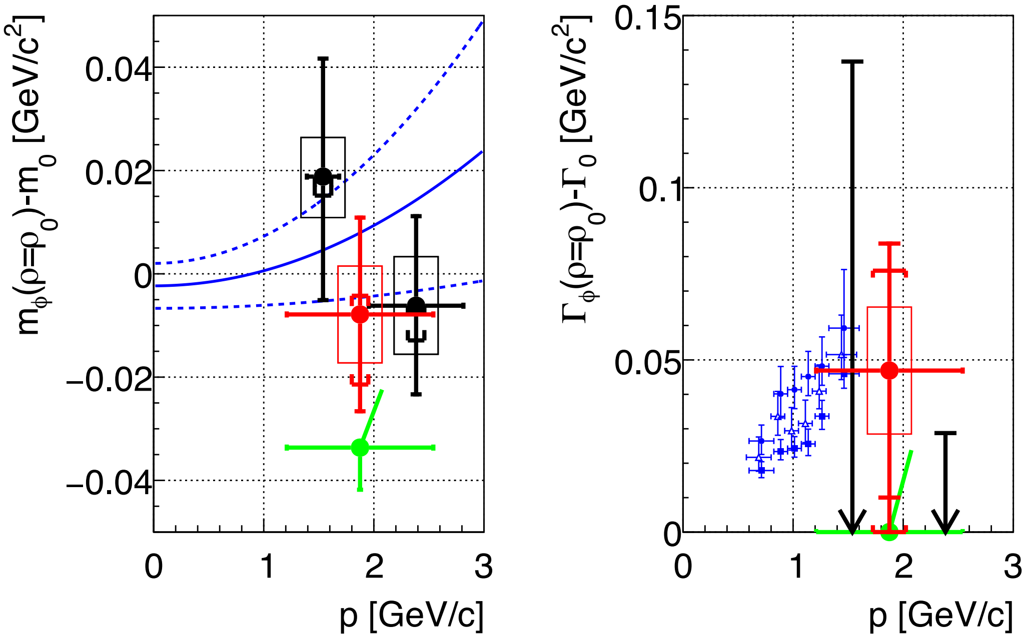

Figure 5.7: Momentum dependence of the difference in resonance mass and decay width between normal nuclear density and vacuum in Models B-2 and C-2. Definitions of the symbols are the same as in Fig. 5.6.

a monotonic momentum dependence; the direction of the shift appears to change. This is considered to be due to the large uncertainties, especially the statistical ones, which make it difficult to draw firm conclusions about the momentum dependence.

In the COSY-ANKE experiment, ϕ mesons with momenta of 0.6 GeV/c to 1.6 GeV/c were measured using $\phi \to K^+K^-$ decays with a 2.83 GeV proton beam incident on C, Cu, Ag, and Au targets. The nuclear dependence of the double-differential cross sections was used, along with multiple theoretical models, to estimate the in-medium decay width at normal nuclear density. The COSY-ANKE data cover only the slow and middle $\beta\gamma$ momentum regions of the present analysis. In the middle region, the present results deviate from the COSY-ANKE data beyond the uncertainty bounds and show an opposite trend: the present results indicate a decrease in width with increasing momentum, while the COSY-ANKE data suggest the opposite. In contrast, the absolute value in the slowest $\beta\gamma$ region is in good agreement.

5.4 Comparison with Previous Results

A comparison of the present results with previous results under the assumption of momentum-independent spectral modification shows that the shift parameter in the density-dependent partial width model is significantly smaller in the present analysis beyond uncertainties. This is considered to be due to the $\beta\gamma$ dependence of the ϕ meson decay-time density distribution. Figure 5.8 shows the dependence of the average decay-time density on the broadening parameter for each $\beta\gamma$ region, obtained in both Ref. [**muto**] and the present analysis. As mentioned earlier, a larger broadening parameter increases the probability of in-medium decay, and thereby increases the average decay-time density. Comparing Ref. [28] and the present analysis for each $\beta\gamma$ region, the average density is smaller in the present analysis in the slowest $\beta\gamma$ region, while in the fastest $\beta\gamma$ region it is higher.

A higher average density makes the spectrum more sensitive to the shift and broadening effects. Therefore, this tendency implies that the present analysis is more influenced by the fastest $\beta\gamma$ region. Since little spectral modification is observed in the fastest $\beta\gamma$ region, this leads to a suppression of the parameters in the momentum-independent model.

In the momentum-independent model, the results of Ref. [28] and those of the present analysis were inconsistent. However, the present analysis suggests a momentum-dependent model in the case of density-dependent partial width, as discussed in Sect. 5.1.4. When the fit is performed only for the Cu target spectrum with the slowest $\beta\gamma$, where a pronounced spectral modification was observed, the results of Ref. [44] and the present analysis are consistent, as shown in Table 5.9.

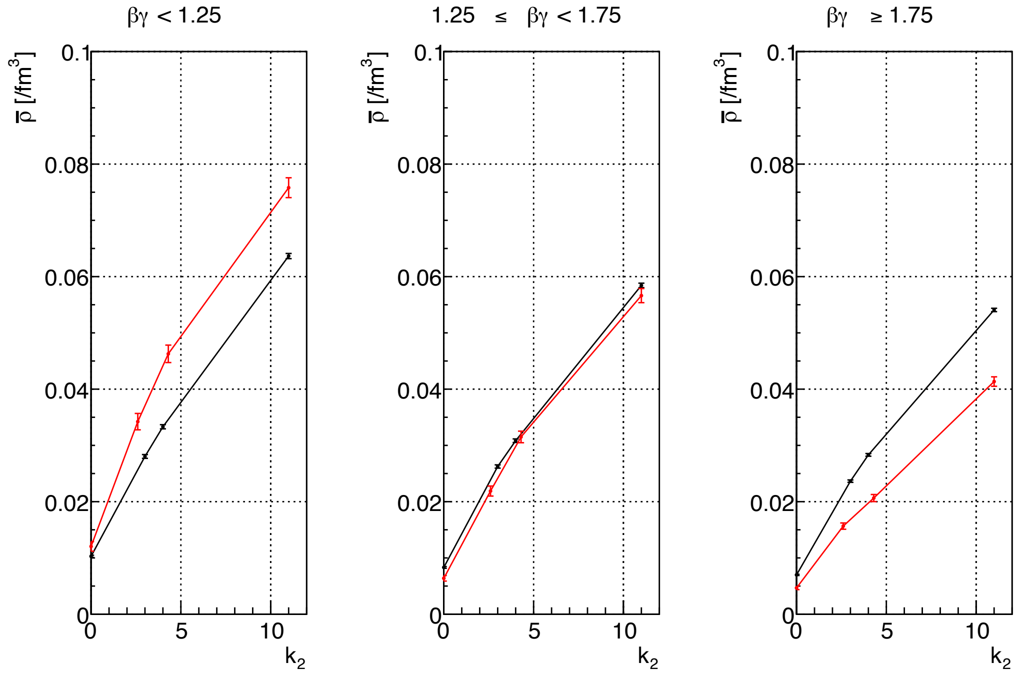

Figure 5.8: Dependence of the average decay-time density on the broadening parameter for each $\beta\gamma$ region for pCu reaction. The values are obtained using the density-dependent partial width model. Black points and lines represent the results from the present analysis, while red points and lines are from Ref. [44]. The effects of spectrometer acceptance and detection efficiency are taken into account.

Table 5.9: Best-fit modification parameters for the Cu target spectrum with the slowest$\beta\gamma$ in the case of density-dependent partial width. Only statistical uncertainties are considered.

	k_1	k_2	χ^2/dof
present analysis	0.034 ± 0.012	8.5 ± 3.3	74/51
Ref. [44]	$0.031^{+0.05}_{-0.03}$	$6.1^{+2.3}_{-1.5}$	63.4/48

Chapter 6

Summary

The masses of light hadrons are significantly larger than the bare masses of their constituent quarks. Theoretically, it is considered that the major part of the hadron mass is generated through the phenomenon known as spontaneous chiral symmetry breaking. On the other hand, this symmetry is expected to be partially restored at finite density or high temperature, and several experiments have been performed to measure hadron masses under such conditions. The measured hadron masses are related to spontaneous chiral symmetry breaking via methods such as QCD sum rules.

The ϕ meson is regarded as a good probe for studying the hadron mass generation mechanism, both experimentally and theoretically. In the KEK-PS E325 experiment, the mass spectrum of the ϕ meson produced in 12 GeV pA reactions was measured, and a significant spectral modification at finite density was observed [28]. Furthermore, the degree of spectral modification allowed for a quantitative discussion of its density dependence.

The spectra obtained in this experiment include ϕ mesons decaying at various densities, ranging from around normal nuclear density down to the vacuum. Meanwhile, the spatial distribution of the target nucleus may change after the pA reaction, but this effect was not considered in the previous analysis. In the present study, we employed the Parton-Hadron-String Dynamics (PHSD) transport calculation to perform a more realistic simulation of the spatial distribution of nucleons after the pA reaction.

In the analysis, three types of fits were performed: one without spectral modification, one with momentum-independent spectral modification, and one with momentum-dependent spectral modification. The fit without modification was rejected at the 99% confidence level, confirming significant spectral modification consistent with Ref. [28]. Although smaller modification parameters were obtained in the momentum-independent case compared to Ref. [28], the experimental data were not well reproduced. In contrast, the fit assuming momentum-dependent spectral modification, as predicted by theory, successfully reproduced the experimental spectra, suggesting the existence of such momentum dependence. The obtained momentum dependence does not contradict predictions from lattice QCD and QCD sum rule calculations. For the most pronounced case of spectral modification, namely the slowest-$\beta\gamma$ ϕ mesons in the Cu target, the results of the present analysis and the previous one were consistent.

Although the present analysis indicated a momentum dependence of the spectral modification, the trend could not be discussed in detail due to large statistical uncertainties. To resolve this issue, the J-PARC E16 experiment, which employs a 30 GeV proton beam, is currently underway [71, 72]. This experiment will provide statistics two orders of magnitude higher than the previous one, enabling a more precise study of the in-medium properties of the ϕ meson and their momentum dependence. Regarding transport calculations, fundamental issues such as the treatment of mass modifications and the stability of the target nucleus need to be addressed. Comparisons across different transport models are also expected to lead to more reliable analyses.

Acknowledgements

In the course of conducting the research presented in this thesis and throughout my doctoral studies, I have been fortunate to receive the guidance, advice, and support of many people.

I am deeply grateful to Dr. Satoshi Yokkaichi of RIKEN for his invaluable guidance and comments during our meetings, as well as for providing the data from the KEK-PS E325 experiment and the codes used in previous analyses. He has supported me in many aspects of the analysis and taught me numerous practical skills and perspectives. As the spokesperson of the J-PARC E16 experiment, which I mainly worked on during my doctoral course, he also gave me essential guidance on how to carry out the experiment from the very beginning. I am sincerely thankful to Dr. Philipp Gubler of JAEA for introducing me to the PHSD model, serving as a bridge to the PHSD developers, and for his theoretical advice and continuous support. I also express my deepest gratitude to Prof. Megumi Naruki of Kyoto University for attending my analysis meetings, proofreading my thesis, and serving as the chief examiner of my doctoral dissertation.

I would like to thank all collaborators of the KEK-PS E325 experiment. In particular, I am grateful to Prof. Hideto En'yo of RIKEN, the spokesperson of the experiment, for his helpful suggestions and encouragement when preparing the analysis results for publication.

My sincere thanks also go to the PHSD development group. I am especially indebted to Prof. Elena Bratkovskaya and Dr. Taesoo Song of GSI for their valuable discussions and advice on various issues encountered while using PHSD.

I am also grateful to Prof. Natsuki Tomida of Kyoto University for proofreading this thesis and providing many constructive comments during the writing process.

I sincerely thank all the staff members of KEK, including the PS accelerator division, online group, electronics group, PS floor group, and in particular the PS beam channel group, for their kind technical support. I also wish to express my gratitude to the staff members of RIKEN-CCJ, RIKEN RSCC, RIKEN Hokusai, and KEKCC for their assistance with data analysis, data archiving, and large-scale simulations.

Although the results of the J-PARC E16 experiment, which I worked on during my doctoral course, are not included in this thesis, I would like to express my heartfelt appreciation to all the collaborators of the experiment for their help and encouragement.

I would like to thank Dr. Tomonori Takahashi of RCNP for his continuous guidance in the development of the trigger system, which I had been engaged in since my master's course. I am also grateful to Prof. Kyoichiro Ozawa, Prof. Kazuya Aoki, and Prof. Yuhei Morino of KEK, as well as Dr. Koki Kanno and Mr. Wataru Nakai of the University of Tokyo, for their valuable advice in experimental preparation and data analysis.

I would also like to express my gratitude to my colleagues, Ms. Sakiko Ashikaga, Dr. Kazuki Suzuki, Mr. Tomoki Murakami, Mr. Ryohei Fujii, Ms. Satomi Nakasuga, Mr. Yudai Takaura, Mr. Takehito Kondo, Mr. Daichi Arimizu, Mr. Naoki Ogata, Ms. Kanako Yamaguchi, Mr. Shunnosuke Nagafusa, Mr. Shuta Ochiai, Mr. Ren Ejima, Mr. Rento Yamada, Mr. Jo Kakunaga, Mr. Shogo Yanai, and Mr. Shunji Hashimoto, from Kyoto University, the University of Tokyo, and Hiroshima University, for their collaboration in experimental studies and for their constant support and encouragement, including many discussions and personal conversations that helped me greatly during my research life.

During my stay in Tokai Village, where J-PARC is located, I was supported by many people. In particular, I would like to express my gratitude to Prof. Mifuyu Ukai of KEK and Dr. Takeshi Yamamoto of JAEA for their kindness and help in my daily life.

I also wish to thank the members of the Nuclear and Hadron Physics Laboratory at Kyoto University, the Meson Science Laboratory at RIKEN, the Research Group for Hadron Nuclear Physics at JAEA, and the Hadron Group at the Institute of Particle and Nuclear Studies, KEK, as well as the members of the KEK e-sys group for providing development space and valuable support.

Finally, I would like to express my heartfelt gratitude to my family for giving me life, nurturing me, and always supporting me throughout these years.

Appendix A

Transport Approaches in General

Transport approaches describing heavy-ion collisions in terms of hadronic degrees of freedom can be broadly categorized into two types: QMD-type and BUU-type calculations [36].

A.1 QMD-type

In QMD-type transport calculations, the single-particle wave function is represented by a Gaussian wave packet, and the total wave function is given as the product of all such packets:

$$\phi_i(\vec{r_i};t) = \frac{1}{(2\pi(\Delta x)^2)^{3/4}} \exp(-\frac{(\vec{r_i} - \vec{R_i}(t))^2}{4(\Delta x)^2}) \exp(\frac{i}{\hbar}\vec{P_i}(t)(\vec{r_i} - \vec{R_i})), \quad \text{(A.1)}$$

$$\Psi(\vec{r_1}, \cdots, \vec{r_A}; t) = \prod_{i=1}^{A} \phi_i(\vec{r_i};t). \quad \text{(A.2)}$$

Here, ϕ_i is the single-particle wave function, $\vec{R_i}$ and $\vec{P_i}$ denote the centroid coordinate and momentum of the packet, respectively, and Ψ is the total wave function. The parameter Δx represents the width of the packet.

Applying the time-dependent variational principle to this form yields equations of motion analogous to classical Hamilton's equations:

$$\frac{d\vec{R_i}}{dt} = \nabla_{P_i}\langle H\rangle, \quad \text{(A.3)}$$

$$\frac{d\vec{P}_i}{dt} = \nabla_{R_i} \langle H \rangle. \tag{A.4}$$

The implementation of the potential term in the Hamiltonian depends on the specific QMD model, while the collision term is introduced separately in a stochastic manner.

JAM, a QMD-type transport calculation was used in Ref. [28].

A.2 BUU-type

In BUU-type transport approaches, the time evolution of the one-body phase-space distribution $f_a(\vec{r}, \vec{p}; t)$ for particle species a is governed by

$$(\frac{\partial}{\partial t} + \nabla_p \epsilon \nabla_r - \nabla_r \epsilon \nabla_p) f_a(\vec{r}, \vec{p}; t) = I_{\text{coll}}[f_a(\vec{r}, \vec{p}; t)]. \tag{A.5}$$

Here, $\epsilon[f]$ is the single-particle energy including mean-field effects, and I_{coll} denotes the two-body collision integral:

$$I_{\text{coll}}[f_a] = \sum_b \frac{g_b}{(2\pi\hbar)^3} \int d^3p_b d\Omega' \, v_{ab} \frac{d\sigma_{ab}^{\text{med}}}{d\Omega'} \Big[(1-f_a)(1-f_b)f'_a f'_b - f_a f_b (1-f'_a)(1-f'_b)\Big], \tag{A.6}$$

where b denotes the collision partner species, g_b is the spin degeneracy factor, v_{ab} is the relative velocity, and σ_{ab}^{med} is the in-medium cross section. f' represents post-collision states, where the first term in the brackets [] represents the gain term and the second term represents the loss term. Equation (A.5) is called the BUU equation.

The characteristics of each BUU calculation depend largely on the treatment of the mean-field potential. With a scalar potential Φ and a vector potential V^μ, the effective mass and four-momentum are defined as

$$m^* = M - \Phi, \tag{A.7}$$

$$\vec{p}^* = \vec{p} - \vec{V}, \tag{A.8}$$

$$E^* = p^{*0} = \sqrt{\vec{p}^{*2} + m^{*2}}. \tag{A.9}$$

The scalar potential is calculated using the scalar density

$$\rho_S = g \int \frac{d^3p^*}{(2\pi\hbar)^3} \frac{m^*}{E^*} f(\vec{r}, \vec{p}^*; t), \tag{A.10}$$

while the vector potential is obtained from the baryon current

$$j^{\mu} = g \int \frac{d^3p^*}{(2\pi\hbar)^3} \frac{p^{*\mu}}{E^*} f(\vec{r}, \vec{p}^*; t). \tag{A.11}$$

Different approximations, such as using non-relativistic reductions, considering only j^0, or including/excluding momentum dependence, distinguish each BUU model.

A.2.1 Test-Particle Method

Since the BUU equation cannot be solved analytically, f_a is represented numerically by an ensemble of so-called test particles:

$$f_a(\vec{r}, \vec{p}; t) = \frac{1}{g_a N_{\mathrm{TP}}} \left(\frac{2\pi}{\hbar}\right)^3 \sum_{i=1}^{N_a N_{\mathrm{TP}}} G(\vec{r} - \vec{R}_i(t))\, \tilde{G}(\vec{p} - \vec{P}_i(t)). \tag{A.12}$$

Here, N_a is the number of particles of species a, N_{TP} is the number of test particles per real particle, and $\vec{R}_i$, $\vec{P}_i$ are the coordinates and momenta of each test particle. The profile functions G and $\tilde{G}$ may be chosen as delta functions, Gaussians, or triangular functions.

A.3 Lattice Hamiltonian Method

Since N_{TP} is finite in practice, artificial fluctuations appear in the particle distributions. To suppress these unphysical effects, the lattice Hamiltonian method is employed. In this approach, space is discretized into cells, and densities and energies are defined on the lattice. The subsequent time evolution of particles within each cell is computed accordingly. This coarse-graining procedure effectively reduces numerical fluctuations. The method is also applicable to QMD calculations.

A.4 Collision Term

The occurrence of a collision is typically determined by the Bertsch criterion, which requires that during a given time step:

1. the particles reach their minimum distance of approach, and

2. this distance is smaller than the interaction radius derived from the cross section.

The post-collision states are assigned probabilistically under energy–momentum conservation, while Pauli blocking is enforced within each spatial cell.

A.5 Comparison between QMD and BUU

The interpretation of collisions differs significantly between QMD and BUU approaches. In QMD, a single collision corresponds directly to a binary nucleon–nucleon interaction. In BUU, however, a collision occurs between two test particles, which represent only fractions of physical particles. Thus, post-collision states may differ for each test particle even if the precollision states are nearly identical. As a result, phenomena such as multi-particle correlations and cluster formation naturally emerge in QMD but require special prescriptions in BUU. On the other hand, the propagation of mean-field dynamics is more straightforward in BUU.

Moreover, QMD calculations are less suited for implementing off-shell dynamics, whereas BUU approaches can more easily incorporate them. Furthermore, while BUU can be formulated in a covariant manner, QMD is fundamentally non-covariant. Consequently, QMD is advantageous when many-body correlations or clusterization are important, while BUU is preferable when off-shell dynamics play a dominant role. As described in Chapter 3, PHSD is advertised as an advanced BUU-type model that is both covariant and capable of treating off-shell dynamics.

Appendix B

e^+e^- Pair Reconstruction

The e^+e^- pair reconstruction from the experimental data was performed through the following procedure:

- Track selection
    - Candidate hit combinations in the CDC and BDC were selected using computationally inexpensive methods such as straight-line or quadratic fits.
    - The selected hit combinations were then subjected to a full Runge–Kutta tracking.
- Target selection
    - Using multiple tracks from the same event, the reaction target was determined.
- Electron/positron identification
    - Electrons and positrons were identified using dedicated electron identification counters.
- Other event selection
    - Events in which multiple e^+e^- pairs could be formed were excluded, since they are likely to contain contributions from γ conversions or π^0 Dalitz decays.

For this analysis, the events obtained by the trigger described in Sect. 2.1.6 were used, that is, events in which each of the two layers of the electron identification counters in both arms had position-correlated hits and hits were also recorded in the STC of both arms. Conditions such as coarse track selections prior to the Runge-Kutta tracking or signal threshold are omitted in this thesis.

B.1 Single Track Fit

The CDC consists of three super layers, each with a horizontal layer (XX') and either one or two tilt layers (one or two among UVV'). For the horizontal layers, hits were required in all super layers, and for the tilt layers, hits were required in at least two super layers. For the BDC, hits were required in at least three of the four layers.

The tracking was performed using the Runge-Kutta method. The step size was typically 50 mm, and reduced to 1 mm near the drift chambers. The initial position was defined as the intersection point between the track obtained from coarse tracking and a cylindrical surface of 100 mm diameter, placed vertically at the center of the magnet.

The coarse tracking used only the CDC data. A quadratic function was assumed for the horizontal plane and a straight line for the vertical plane. The initial momentum was obtained from a circular fit in the horizontal plane.

B.2 Target Selection

First, the vertex was determined without imposing any target constraint by minimizing the value of S based on the tracks in the same event. S was calculated as follows;

$$S = \frac{1}{3N_t - 4} \sum_{j=1}^{N_t} ((\frac{d_x^j}{\sigma_x})^2 + (\frac{d_y^j}{\sigma_y})^2 + (\frac{d_z^j}{\sigma_z})^2), \tag{B.1}$$

where N_t is the number of tracks in an event, $\vec{d^j}$ is the distance vector between the vertex point and the j-th track, and σ_i is the error of the vertex determination in each axis and was determined as $\sigma_x = 1.80\,\mathrm{mm}$, $\sigma_y = 7.15\,\mathrm{mm}$, and

$\sigma_z = 1.44\,\mathrm{mm}$. The reference vertex position and resolution were obtained from the vertex distributions and summarized in Table B.1.

Events satisfying $S < 5$ and lying within 3.5 standard deviations from the center of any target were selected. To determine the reaction target, $\chi^2_{T_i}$ was calculated for each target as follows,

$$\chi^2_{T_i} = \sum_{j=x,y,z} (\frac{d_j - c_{ij}}{\sigma_{ij}})^2, \tag{B.2}$$

where $\vec{d}$ is the reconstructed vertex position, $\vec{c_i}$ is the center of beam image for target i, and $\vec{\sigma_i}$ is the vertex resolution around target i. The one with the smallest value was assigned as the reaction target.

Table B.1: Vertex distribution in the double-arm events. z corresponds the z position of each target. x and y correspond to the center of beam image for each target.

Year	Target	x [mm]	y [mm]	z [mm]	σ_x [mm]	σ_y [mm]	σ_z [mm]
2001	Cu-1	3.13	0.61	-47.04	3.24	3.68	3.73
	C	4.03	0.62	-0.14	3.74	3.70	3.48
	Cu-2	4.91	0.67	45.46	2.42	3.14	2.71
2002	Cu-1	0.89	0.55	-48.03	1.98	4.33	3.21
	Cu-2	1.31	0.54	-23.41	2.27	4.54	3.35
	C	1.72	0.52	0.17	1.97	3.85	3.20
	Cu-4	2.22	0.54	24.60	2.94	3.98	1.98
	Cu-5	2.57	0.57	44.21	2.61	3.74	2.01

B.3 Pair Track Fit

With the z-coordinate fixed to the value of the reaction target determined above, a pair track fit was performed by minimizing the following quantity under the constraint that both tracks share a common vertex:

$$\chi_C^2 = \sum_{s=\pm 1} \sum_{l} (\frac{h_l^s - e_l^s}{\sigma_l})^2 + \sum_{j=x,y} (\frac{v_j - c_j}{\sigma'_j})^2, \tag{B.3}$$

where h_l^s and e_l^s are the hit position and the track position, respectively, with a charge s on the drift chamber layer l, σ_l is the position resolution of layer l, $\vec{v}$ is the vertex point on the reaction target, $\vec{c}$ is the beam center position on the reaction target, and σ'_j is the beam size for each axis. The beam size in the x-direction was taken from Sect. 2.1.2, and the same value was used for the y-direction. For each pair, the two tracks were required to belong to different arms. Pairs with $\chi_C^2/\mathrm{dof} < 5$ were accepted as final track pairs.

B.4 Electron Identification

Due to the limited vertical acceptance of the gas Cherenkov counters, only tracks with vertical incident angles within ±0.45 rad at the FGC and within ±0.15 rad at the RGC were selected. In order to avoid misidentification of pions in the Gas Cherenkov counters, tracks with momenta above 2.7 GeV/c were excluded.

Bibliography

[1] S. Navas et al., Phys. Rev. D **110**, 030001 (2024).

[2] R. S. Hayano and T. Hatsuda, Rev. Mod. Phys. **82**, 2949–2990 (2010).

[3] V. Koch, Int. J. Mod. Phys. E **06**, 203–249 (1997).

[4] M. Gell-Mann, R. J. Oakes, and B. Renner, Phys. Rev. **175**, 2195–2199 (1968).

[5] S. Hübsch and D. Jido, Phys. Rev. C **104**, 015202 (2021).

[6] D. Jido, T. Hatsuda, and T. Kunihiro, Phys. Lett. B **670**, 109–113 (2008).

[7] N. Kaiser, P. D. Homont, and W. Weise, Phys. Rev. C **77**, 025204 (2008).

[8] S. Goda and D. Jido, Phys. Rev. C **88**, 065204 (2013).

[9] A. Lacour, J. A. Oller, and U.-G. Meißner, J. Phys. G: Nucl. Part. Phys. **37**, 125002 (2010).

[10] T. Nishi et al., Nat. Phys. **19**, 788–793 (2023).

[11] W. Weise, Prog. Theor. Phys. Suppl. **174**, 1–13 (2008).

[12] P. Gubler and D. Satow, Prog. Part. Nucl. Phys. **106**, 1–67 (2019).

[13] T. Hatsuda and S. H. Lee, Phys. Rev. C **46**, R34–R38 (1992).

[14] S. Zschocke, O. Pavlenko, and B. Kämpfer, Eur Phys J A **15**, 529–537 (2002).

[15] P. Gubler and W. Weise, Phys. Lett. B **751**, 396–401 (2015).

[16] P. Gubler and W. Weise, Nucl. Phys. A **954**, 125–148 (2016).

[17] F. Klingl, T. Waas, and W. Weise, Phys. Lett. B **431**, 254–262 (1998).

[18] D. Cabrera and M. J. Vicente Vacas, Phys. Rev. C **67**, 045203 (2003).

[19] D. Cabrera, A. N. Hiller Blin, and M. J. Vicente Vacas, Phys. Rev. C **95**, 015201 (2017).

[20] Y. Aoki et al., `10.48550/arXiv.2411.04268` (2025).

[21] M. Asakawa and C. Ko, Nucl. Phys. A **572**, 732–748 (1994).

[22] F. Klingl, N. Kaiser, and W. Weise, Nucl. Phys. A **624**, 527–563 (1997).

[23] S. H. Lee, Phys. Rev. C **57**, 927–930 (1998).

[24] B. Kämpfer, O. Pavlenko, and S. Zschocke, Eur Phys J A **17**, 83–87 (2003).

[25] P. Gubler and K. Ohtani, Phys. Rev. D **90**, 094002 (2014).

[26] H. Kim and P. Gubler, Phys. Lett. B **805**, 135412 (2020).

[27] J. Kim, P. Gubler, and S. H. Lee, Phys. Rev. D **105**, 114053 (2022).

[28] R. Muto et al., Phys. Rev. Lett. **98**, 042501 (2007).

[29] F. Sakuma et al., Phys. Rev. Lett. **98**, 152302 (2007).

[30] M. Hartmann et al., Phys. Rev. C **85**, 035206 (2012).

[31] M. H. Wood et al., Phys. Rev. Lett. **105**, 112301 (2010).

[32] T. Ishikawa et al., Phys. Lett. B **608**, 215–222 (2005).

[33] J. Adamczewski-Musch et al., Phys. Rev. Lett. **123**, 022002 (2019).

[34] A. Yu. Polyanskiy et al., Phys. Atom. Nucl. **75**, 63–75 (2012).

[35] R. Arnaldi et al., Eur. Phys. J. C **64**, 1–18 (2009).

[36] H. Wolter et al., Prog. Part. Nucl. Phys. **125**, 103962 (2022).

[37] A. W. R. Jorge, T. Song, Q. Zhou, and E. Bratkovskaya, Phys. Rev. C **111**, 064904 (2025).

[38] T. Song, J. Aichelin, and E. Bratkovskaya, Phys. Rev. C **106**, 024903 (2022).

[39] P. Gubler, M. Ichikawa, T. Song, and E. Bratkovskaya, Phys. Rev. C **111**, 034908 (2025).

[40] M. Ichikawa et al., Prog. Theor. Exp. Phys. **2025**, 093D01 (2025).

[41] K. Ozawa et al., Phys. Rev. Lett. **86**, 5019–5022 (2001).

[42] M. Naruki et al., Phys. Rev. Lett. **96**, 092301 (2006).

[43] T. Tabaru et al., Phys. Rev. C **74**, 025201 (2006).

[44] R. Muto, Doctoral dissertation (Kyoto University, 2007).

[45] Vector Fields Limited (UK), `http://www.vectorfields.co.uk/`.

[46] J. Allison et al., IEEE Trans. Nucl. Sci. **53**, 270–278 (2006).

[47] J. Allison et al., Nucl. Instrm. Meth. A **835**, 186–225 (2016).

[48] S. Agostinelli et al., Nucl. Instrum. Meth. A **506**, 250–303 (2003).

[49] A. Spiridonov, `10.48550/arXiv.hep-ex/0510076` (2005).

[50] E. Oset and A. Ramos, Nucl. Phys. A **679**, 616–628 (2001).

[51] R. J. Glauber and G. Matthiae, Nucl. Phys. B **21**, 135–157 (1970).

[52] Y. Nara, N. Otuka, A. Ohnishi, K. Niita, and S. Chiba, Phys. Rev. C **61**, 024901 (1999).

[53] W. Cassing and S. Juchem, Nucl. Phys. A **677**, 445–460 (2000).

[54] W. Cassing and S. Juchem, Nucl. Phys. A **665**, 377–400 (2000).

[55] W. Cassing and S. Juchem, Nucl. Phys. A **672**, 417–445 (2000).

[56] W. Cassing, Lecture Notes in Physics **989**, `10.1007/978-3-030-80295-0` (2021).

[57] W. Cassing, A. Palmese, P. Moreau, and E. L. Bratkovskaya, Phys. Rev. C **93**, 014902 (2016).

[58] T. Sjöstrand, S. Mrenna, and P. Skands, J. High Energy Phys. **2006**, 026–026 (2006).

[59] B. Andersson, G. Gustafson, and T. Sjöstrand, Phys. Scr. **32**, 574 (1985).

[60] B. Andersson, Cambridge Monographs on Particle Physics, Nuclear Physics and Cosmology, `10.1017/CBO9780511524363` (1998).

[61] B. Andersson, G. Gustafson, and T. Sjöstrand, Nucl. Phys. B **197**, 45–54 (1982).

[62] B. Andersson, G. Gustafson, G. Ingelman, and T. Sjöstrand, Phys. Rep. **97**, 31–145 (1983).

[63] P. Eden, `10.48550/arXiv.hep-ph/9610246` (1996).

[64] W. Cassing and E. L. Bratkovskaya, Phys. Rep. **308**, 65–233 (1999).

[65] KEKCC support page, `https://kekcc.kek.jp/service/kekcc/support/en/`.

[66] J. Xu et al., Phys. Rev. C **93**, 044609 (2016).

[67] N. Davidson, T. Przedzinski, and Z. Was, Comput. Phys. Commun. **199**, 86–101 (2016).

[68] V. K. Magas, L. Roca, and E. Oset, Phys. Rev. C **71**, 065202 (2005).

[69] E. Y. Paryev, J. Phys. G: Nucl. Part. Phys. **36**, 015103 (2008).

[70] H. Schade, Doctoral dissertation (University of Dresden, 2010).

[71] M. Ichikawa et al., Acta Phys. Pol. B Proc. Suppl. **16**, 1 (2023).

[72] K. Aoki et al., J. Subatom. Part. Cosmol. **3**, 100019 (2025).